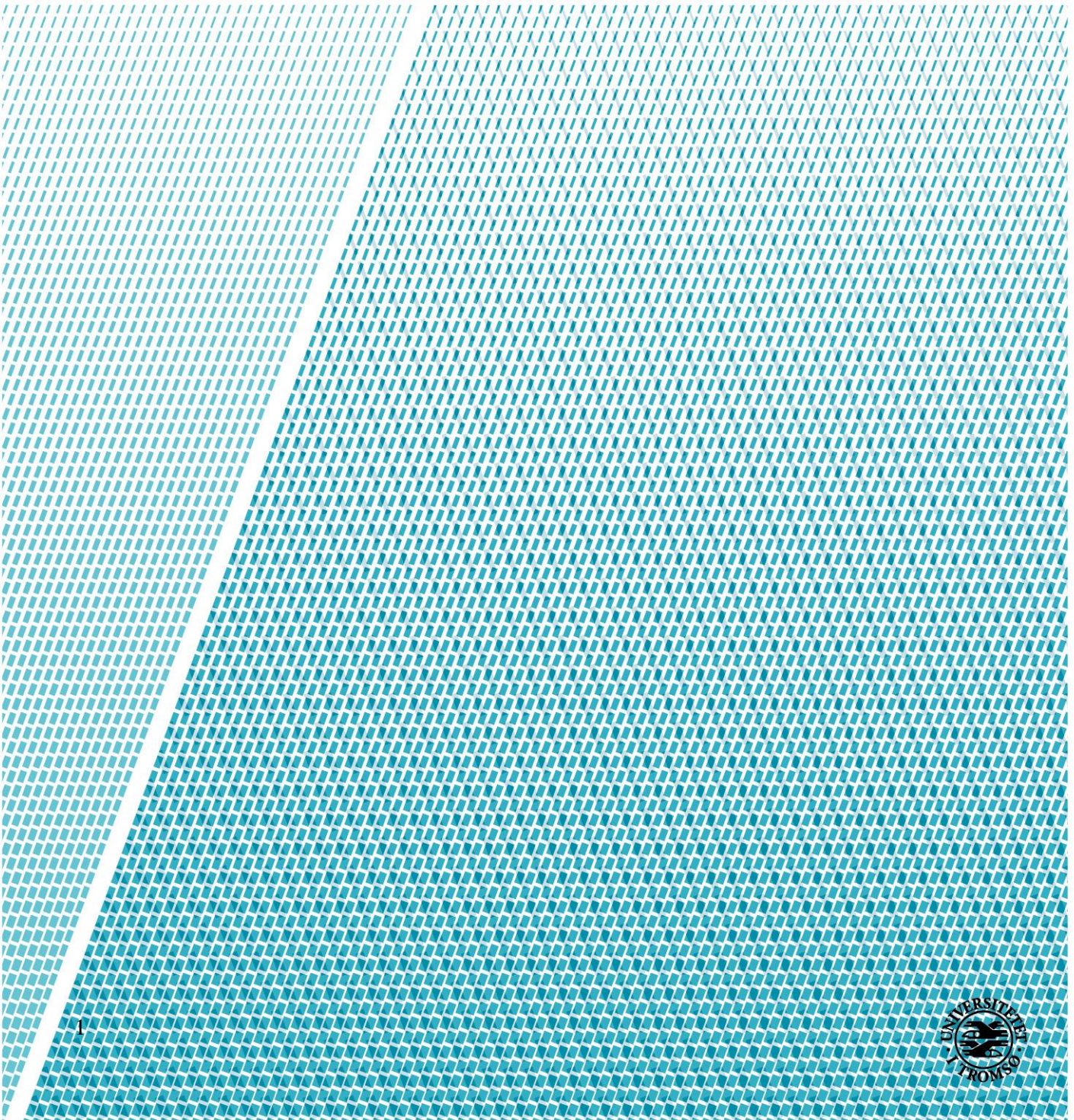# The origin of quartz-carbonate veins hosted by ductile shear zones of the Astridal Supracrustal Belt, West-Troms Basement Complex.

With focus on structural geology and hydrothermal processes.

Thea Mathilde Forslund

Master in Geology, May 2018

1

Content

Acknowledgments

1 Introduction

1.1 Context of study

Greenstone belts worldwide host numerous orogenic gold deposits (e.g. (Groves et al., 1998, Niiranen et al., 2015, Groves et al., 2018). In general, orogenic gold deposits are invariably found associated in zones of high strain that are brittle, brittle-ductile or ductile deformation depending on crustal depths fluids were circulating (McCuaig and Kerrich, 1998). Crustal thickening, deformation, metamorphism and synorogenic magmatism all play important roles in the origin of the fluid and their paths upwards into the crust (Robb, 2004). Although the origin of orogenic gold deposit still controversial, the role of H_2O-CO_2 phase separations is usually considered as an important process in gold deposition and could explain why some rich accumulations of gold in quartz veins (Robb, 2004).

An peninsula called Småsandnesset in the Astridal supracrustal belt on Senja, in the West Troms Basement Complex (Fig.1), was mapped in detail to get a better understanding of a quartz-carbonate veins hosted in chlorizied mylonitic shear zones, that occur in the axial plane of subvertical folds (Bergh et al., 2010, Bergh et al., 2015). Sediment-derived calcarous shist and marbles are also present in the Astridalen metasupracrustal belt (Zwaan et al., 1998, Pedersen, 1997). These units are conformable with banded amphibolite and Fe-rich mica schists (Bergh et al., 2010, Bergh et al., 2015). The calcareous schist and marbels may potentially be linked to the quartz and calcite veins.

The studied chloritized mylonitic shear zone in the Astridal belt crosscuts the main foliation of the banded amphibolite (Bergh et al., 2010, Bergh et al., 2015). The chloritized mylonitic shear zone contains a phyllonitic (chlorite, carbonate, albite) steeply dipping fabric/foliation and hydrothermally precipitated quartz and calcite veins (containing high concentrations of CO_2), and therefore accomplishes the criterions for possibly gold bearing veins (Hagemann and Cassidy, 2001). The detailed mapping of Småsandnesset, done for this master thesis was to provide knowledge about the structural and geochemical evolution of these hydrothermal veins and their relation to the tectono-stratigraphy and structural evolution in the Astridal metasupracrustal belt.

1.2 Goal of work

Younger not dated mylonitic NE-SW trending shear zones arranged axial planar to F3-folds in the area of Småsandnesset formed at low to medium grade metamorphic conditions (Bergh et al., 2010), and their relations to previously known tectono-stratigraphic evolution have been the main goal for this master thesis. One of these mylonitic shear zones host hydrothermally precipitated quartz and calcite veins, and fluid inclusions studies applied to quartz will reveal the chemical composition of the hydrothermal fluids and pressure and temperature condictions during the vein deposition.

The goals will be achived by combining structural mapping of the penisula of Småsandnesset, combined with microscopic studies, XRD analyses, SEM/EDS analyses, stable isitope studies (δC^{13} vs. δO^{18}) and fluid inclution studies. Microscopic studies will gain information about the host rocks composition and metamorphic evolution. XRD analysis reveals information about alteration products within the chloritizied mylonitic shear zone. SEM/EDS will infrom about realtion of oreminerals to the chloritizied mylonitic shear zone. The stable isotope compositions (δC^{13} vs. δO^{18}) of carbonates will give an insight into the orgin of CO_2.

1.3 Location of the study area

The field area is situated in the geological province termed West Troms Basment Complex (Bergh et al. 2010), in the northernmost part of the island of Senja, in Troms region, northern Norway (fig. 1) The mapped area belongs to the Astridal metasupracrustal belt, which is well exposed in a 2-3 km long coastal section surrounded by steep mountain sides, in gullies and along scarps in the valley. The geology in the area is easily accessible along the shoreline, but the outcrop quality decreases from the shoreline and further up in the terrain. The penisula Småsandnesset sticks out from the rest of the suprarsutal belt, and are situated in the middle of the Astridal supracrsutal belt.
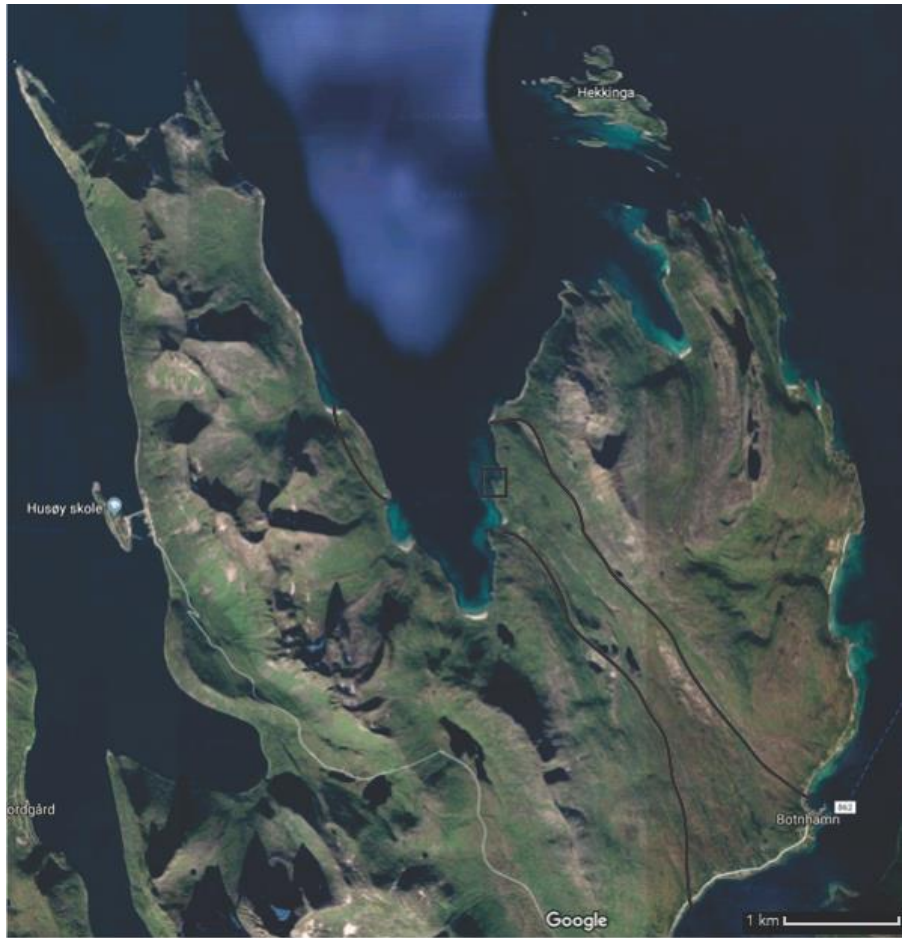
Figure 1. Aerial photograph with line interpretation of the Astridal belt on northeast Senja. Note location of the peninsula of Småsandnesset.

1.4 Regional Geology

1.4.1 The Fennoscandia shield

Fennoscandia is referred to as the old Precambrian shield area in northern Norway, Sweden, Finland and the Kola province of Russia. The Fennoscandian shield is the largest exposed segment of Precambrian crust in Europe (Sundblad, 2003). The large span in age (3.5-1.5 Ga) of the Fennoscandian shield is a result of several orogenic events, ie. The Lopian, the Lappland-Kola (Svecokarelian), the Svecofennian, the Gothian and Sveconoervegian orogenies (Hölttä P, 2008, Holtta et al., 2008) (Lahtinen et al., 2008). These Precambrian provinces host various greenstone belts of different ages, composed of metasedimentary and metavulcanoclastic rocks usually enriched in Fe, Zn, Cu, Ni and Au mineralization (Sundblad, 2003).

The Archean domain is situated in the northeastern parts of the Fennoscandian shield and are devided into four main provinces, the Karelian, the Belomorian, the Kola and the Norrbotten province (Gorbatschev and Gaál, 1987) Paleoproterozoic rifting and breakup between 2.5 and

2.0 Ga (Gorbatschev and Bogdanova, 1993); (Lahtinen et al., 2008) has strongly affected the Archean domain. The Paleoproterozoic orogenic evolution of Fennoscandia includes the Lapland-Kola orogeny (1.94-1.86 Ga) in the northeastern part, and the Svecofennian orogeny (1.92-1.79 Ga) in the northwestern part. Both of these orogeny evolved by rifting, opening and then closing of oceanic and arc-marginal basins (Lahtinen et al., 2008). The Lapland-Kola mobile belt separates the Archean and Svecofennian domains, and reflect a collisional orogeny (Lahtinen et al., 2008). The Fennoscandian shield grew by Andean-type accretion during the Gothian (1.64-1.52 Ga) and Sveconorwegian (1.14-0.9 Ga) orogeny. During the Gothian orogeny voluminous granite bodies as well as the Transscandinavian Igneous Belt intruded the shield (Larson and Berglund, 1992). The Svecofennian orogeny involved mostly crustal stacking and accretion of crust in the southwest, rather than formation of new crustal segments (Gorbatschev and Bogdanova, 1993).

The Caledonian thrust nappes in northern Norway are located west of the autochthonous Precambrian shield areas of Russia, Finland and Sweden (fig. 2) and formed much later. The Ordovician-Silurian (500-390 Ma) as a result of a final continent-continent collision.

Several Precambrian greenstone belts in Northern Norway are exposed in tectonic windows within and west of the Caledonian thrust nappes, and these Precambrian rocks, including those of the West Troms Basement Complex (Bergh et al., 2010), show remarkably weak signs of Caledonian deformation, compared to the Paleoproterozoic rocks in the southwestern part of Norway (Corfu et al., 2003). The greenstone belts in Northern Norway are mostly, with some exceptions of Paleoproterozoic age (2.4-1.9 Ga), and they are related to a crustal extension event when the Archean continent split up to form the Kola Ocean (Holtta et al., 2008); (Lahtinen et al., 2008). They are surrounded by Archean TTG-gneisses and Paleoproterozoic intrusives and magmatic rocks and contain numerous stratiform ore bodies. Rifting is always a good depositional environment for ore deposit, because of the accumulation of sediments, the heat from the rifting, which causes circulation of water and the thinning of the crust, which may work as a trap.
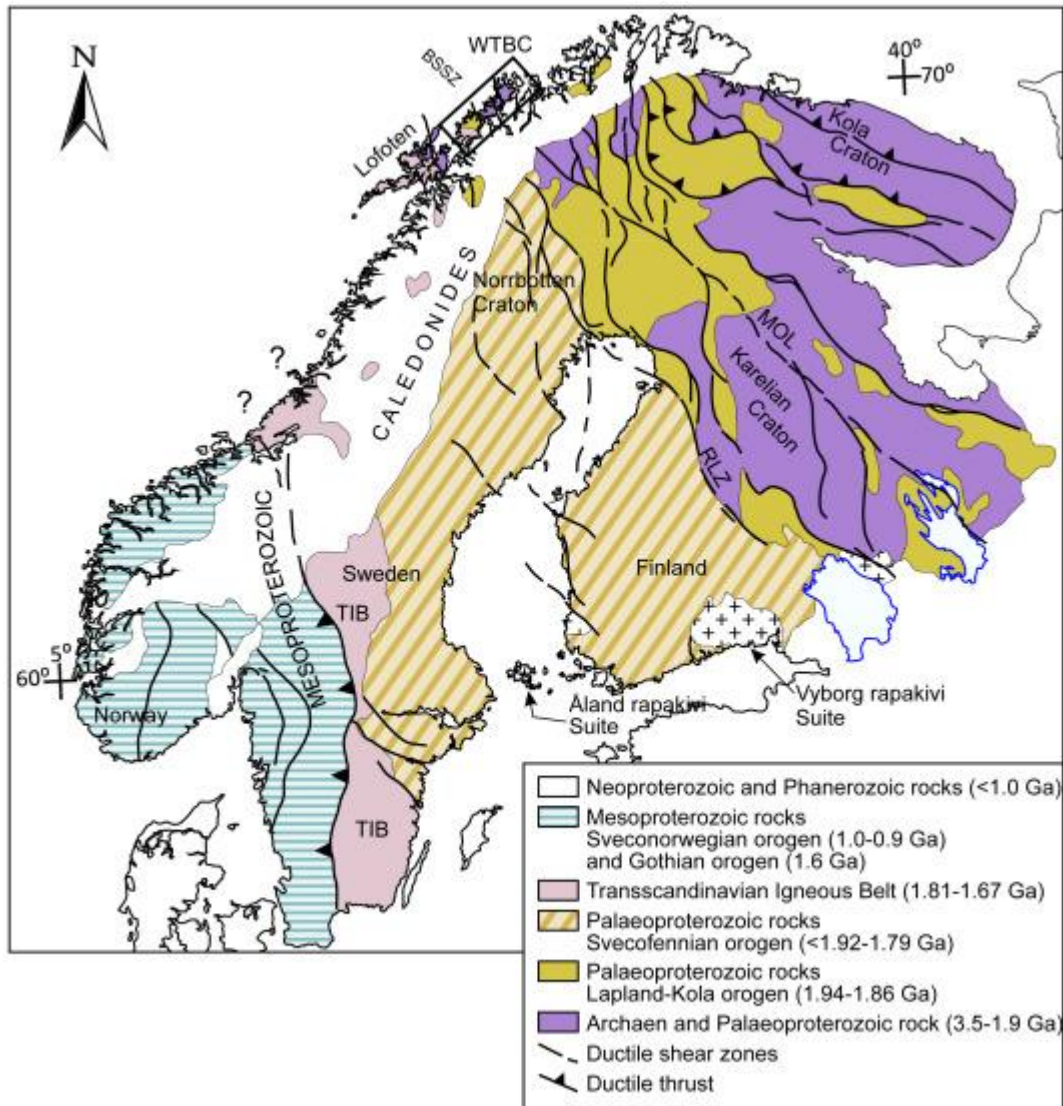
Figure 2. Geological map of the Fennoscandian Shield. Showing Archean cratons, Major Paleoproterozoic and Mesoproterozoic tectonic events and reginal scale ductile shear zones (based on (Koistinen, 2001). Note location of the West Troms Basement complex (see frame) northwest of the Scandinavian Caledonides. Components and architectures Abbrevations: BBSZ: Botnian-Senja shear zone, MOL: Malangen-Onega linament, RLZ: Raahe-Ladoga shear zone, TIB: Transscandinavian Igneous Belt, WTBC: West Troms Basement Complex. Figure from (Bergh et al., 2015).

1.4.2 West Troms Basement Complex

The West Troms Basement Complex is the region located northwest of the Caledonides, and stretches from the islands of Senja in southwest to Vanna in northeast. WTBC is separated from the Caledonian thrust nappes by thrust faults and Mesozoic normal faults (Zwaan et al., 1998); (Bergh et al., 2014). WTBC is bounded by plutonic rocks of the anorthosite-magnerite-charnockite-granite complex (AMCG) suite in the southwest (Griffin et al., 1978, Corfu, 2004). The WTBC is elevated at least 2-3 km compared to the Caledonian thrust nappes. This is thought to be the consequence of development of a horst that was formed during the Mesozoic

rifting and opening of the North Atlantic Ocean (Olesen et al., 1997); (Indrevær et al., 2013). The WTBC shows remarkably few mineralogical and structural signs of impact from the Caledonian orogeny (Corfu et al., 2003). Despite the proximity to the Caledonides, the Archean and Paleoproterozoic structures are well preserved within the WTBC (Bergh et al., 2010). Ductile deformation and amphibolite to greenschist facies metamorphic overprint and several major NW-SE striking shear zones characterize the WTBC, the most dominant one being the Botnian-Senja Shear Zone (Zwaan, 1995, Henkel, 1989). The main deformation that can be observed is mainly caused by the Svecofennian orogeny (1.8-1.7 Ga). The metamorphic grade is increasing to the southwest from lower greenschist facies at Vanna (Bergh et al., 2007) to amphibolite facies central parts of the WTBC further south (Bergh et al., 2010).

In regional context, the Bothnian-Senja Shear Zone can be traced underneath the Caledonides and further in to Sweden (Henkel, 1989). On the other hand WTBC shows many similar geological and structural similarities to the old Precambrian Laurentian Shield continent, for example precense of numerous greenstone belts, mafic dyke swarms the within the TTG-gneisses in Greenland with approximately the same composition and age as a mafic dyke swarm in the Ringvassøya greenstone belt (Kullerud et al., 2006b). The discussion about weather WTBC belongs to the old Baltic continent or the Laurentian continent has been ongoing for a long time (see (Bergh et al., 2015).

The WTBC consists of various Meso- and Neoarchean TTG gneisses separated by several NW-trending ductile shear zones, which separates the TTG-gneisses from several NW-SE-trending metasupracrustal belts (Bergh et al., 2010). The age of the metasupracrustal belts vary from Neoarchean age 2.7 Ga in Ringvassøya (Motuza et al., 2001). 2.2-2.4 Ga for meta-sedimentary rocks on Vannøya (Bergh et al., 2007) to about 1.9 in the Torsnes and Astridalen metasupracrustal belts ((Bergh et al., 2010); (Myhre et al., 2011). The WTBC also consists of the Ersfjord granite and the Hamn norite younger intrusions (1.8-1.7 Ga), which intruded the TTG-gneisses and some of the metasupracrustal units (Corfu et al., 2003).
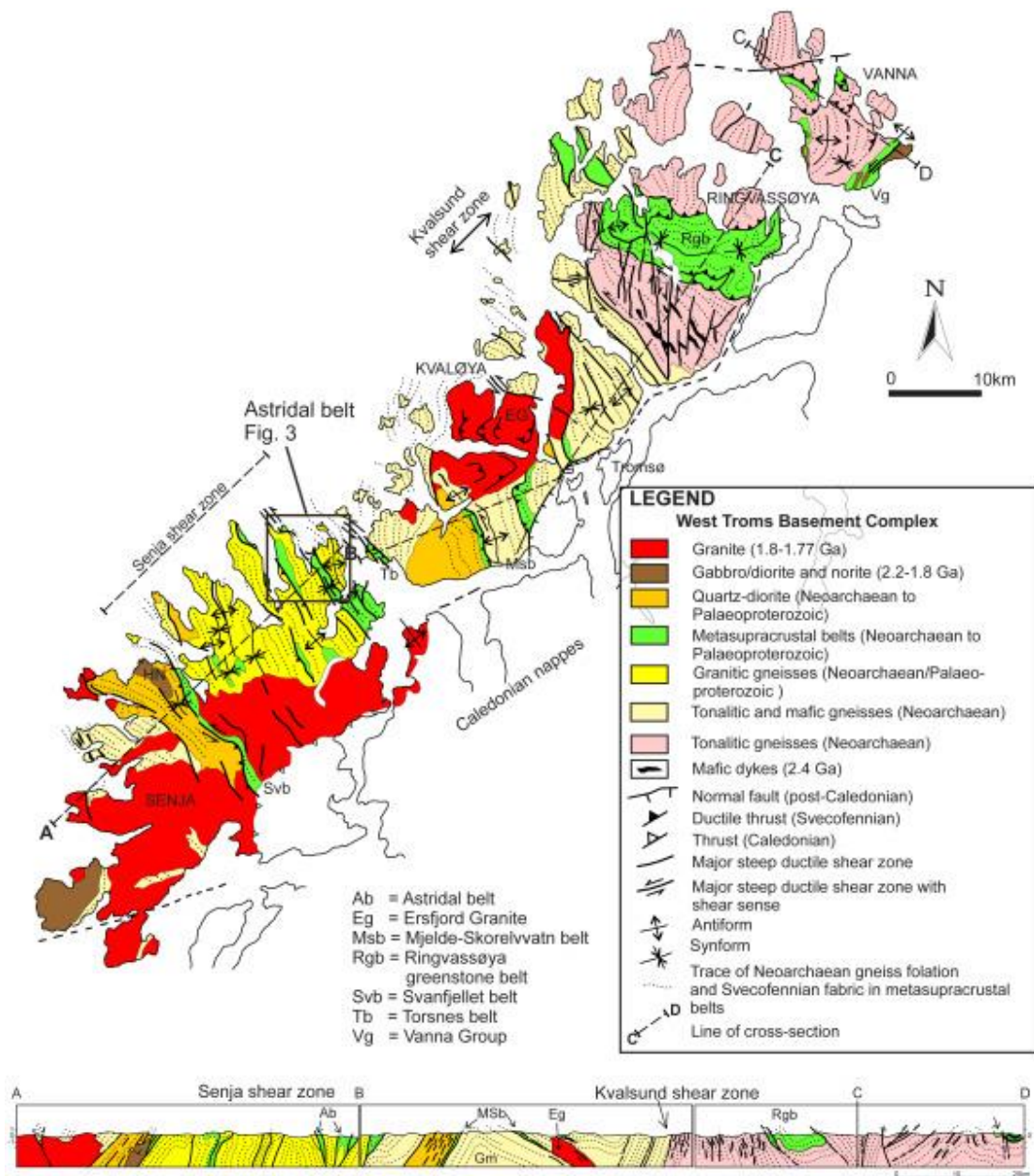
Figure 3. Geological and tectonic map over the West Troms Basement Complex with cross-section. Figure shows the main TTG-gneisses domains, supracrustal belts and magmatic intrusions. Note location of the Astridal supracrustal belt (see frame).The map is revised after (Zwaan et al., 1998, Kullerud et al., 2006a) and (Bergh et al., 2010). Figure is from (Bergh et al., 2015).

1.5 The Astridal supracrustal belt

The Astridal supracrustal belt is one of several NW-SE trending Paleoproterozoic metasupracrustal belts in the 30km wide Senja Shear Zone located in the island of Senja in northern Norway (Zwaan, 1995). The metasupracrustal belt is surrounded by Neoarchean (2.6 Ga) TTG-gneisses. The surrounding TTG-gneisses show a Neoarchean high-grade foliation (Myhre et al., 2013), which is slightly discordant on a regional scale, but conformable with the

main foliation of the metasupracrustal rocks on a local scale (Bergh et al., 2015). All the metasupracrustal belts have suffered polyphase late/post-Svecofennian orogenic deformation of mostly amphibolite phase metamorphism (Bergh et al., 2015). The Astridal metasupracrustal belt consists of meta-volcanic and meta-siliciclastic rocks like hornblende rich-amphibolite schist, graphite schist, marbles, meta-psammite, various metamorphosed calc-silicate rocks and various ultramafic rocks (Pedersen, 1997); (Bergh et al., 2010). On the western side of the fiord, a succession of ultramafic, spinel-bearing olivine-orthopyroxene hornblendite, hornblende peridotite and olivine-bearing meta-grabbro crop out (Priyatkina, 2013). In adittion, lenses of peridotite occur both in the Astridal belt units and in the surrounding TTG-gneisses. These rocks are all intrusive, but deformed into lenses that are conformable with the main host rock foliation (Priyatkina, 2013), which is partly mylonitic (Bergh et al., 2010). The Astridal metasupracrustal belt are also intruded by various generations of granite pegmatite dykes, which have yielded a U-Pb age from zircon and titanite ranging between 1758 and 1562 Ma (Bergh et al., 2015), with a weak Caledonian overprint at about 400 Ma (Bergh et al., 2015). This indicates that the deformation events D1-D3 that affected the Astridal belt (and WTBC) were slightly younger than the main Svecofennian orogeny and that the pegmatitic dykes intruded both during the main 1.77-1.75 Ga contraction events (D1 and D2), and in later pulses (1.7-1.65 Ga) during later stages of deformation (D3) (Bergh et al., 2015). The rocks have undergone multiple folding and are cut by several generations of pegmatite bearing anastomosing ductile shear zones that are both parallel to lithological contacts, parallel to the mylonitic foliation and parallel to axial-surfaces and/or other truncation fabrics. Some of these shear zones contain quartz and carbonate veins and are the target for this study.

The polyphaser orogenic deformation in the West Troms Basement Complex included the following main structures and events (D1-D3). D1 structures represent the main host rock foliation of the metasupracrustal rocks, which is partly mylonitic and dips steeply to the NE and is formed axial planar to isoclinal folds (F1) and/or as foliation-parallel thrusts due to NE-directed thrusting (Bergh et al., 2010).

D2 structures represents macro folding (F2) of the foliation by subhorizontal NW-SE trending macro folds with steep limbs and general vergence to the NE (Bergh et al., 2010). These structures are believed to have formed by continuous NE-SW directed crustal shortening. These structures are a result of convergent accretionary and/or collisional tectonics in the timespan 1.77-1.75 Ga (Corfu et al., 2003), (Bergh et al., 2010), which is slightly postdating the Svecofennian orogeny.

D3 structures represents steeply NW-plunging sinstral macro and meso scale folds (F3) and associated steep NW-SE trending mylonitic strike-slip shear zones locally arranged parallel to fold axial surfaces and truncating cleavage surfaces. These structures formed at lower metamorphic conditions. The D3 event is thought to be a response to post-svecofennian strike-slip reactivation of the steep D2 fold limbs, combined with orogeny-parallel reactivation and increased transpression with time (Bergh et al., 2010) (Bergh et al., 2015).
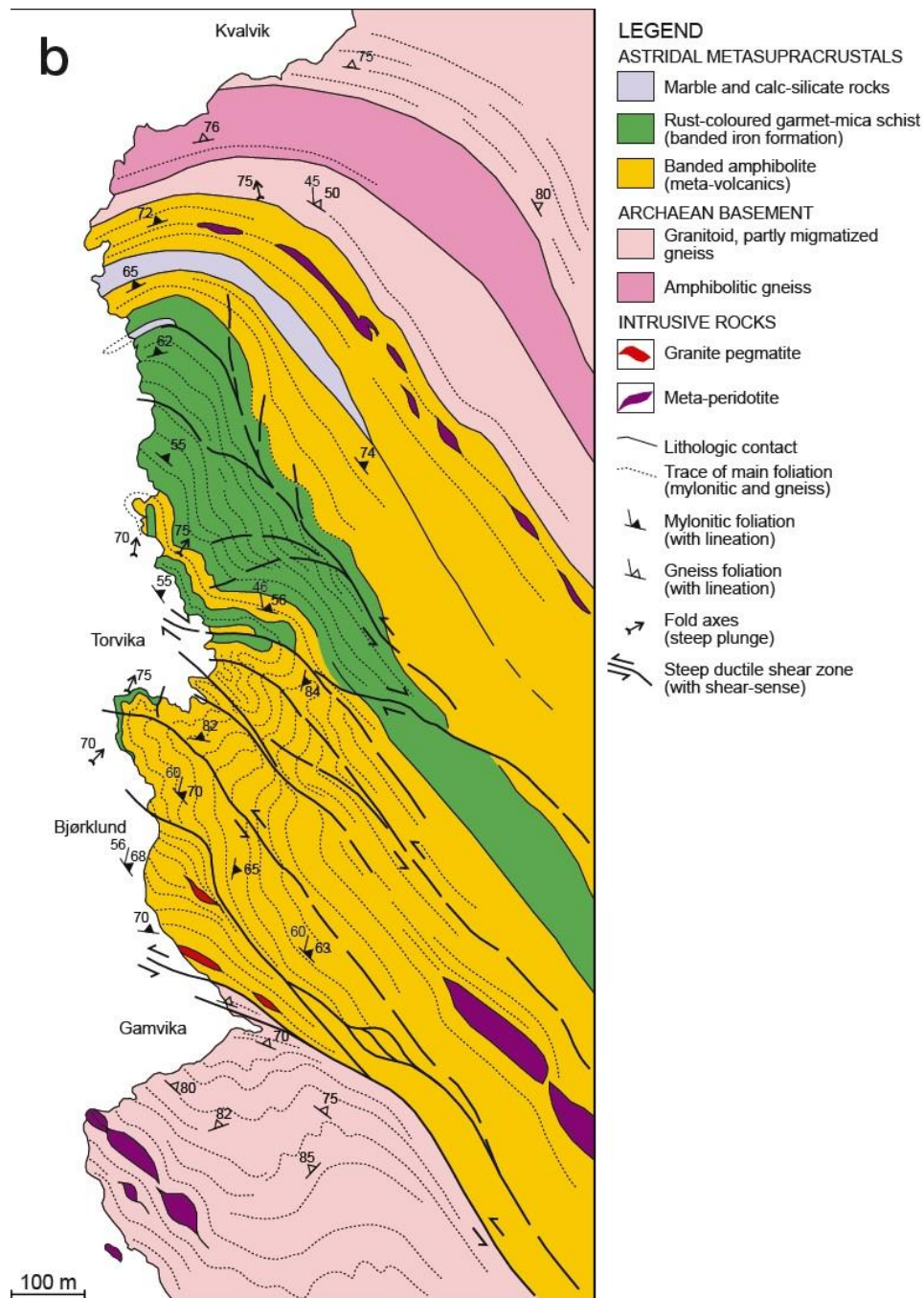
Figure 4. Detailed geologic and tectonic map of the Astridal supracrustal belt east of Baltsfjorden. Note that the entire belt and the surrounding gneisses are folded in a steeply plunging macro fold, disharmonic and refolded fold styles in the hinge and steep, NW-SE to N-S trending axial-plane shear zones (after (Bergh et al., 2010)).

1.6 Mineralization in the Astridal Metasupracrustal belt

The most pronounced mineralization in the Astridal metasupracrustal belt occurs within a banded quartz-garnet-mica schist which is enriched in iron oxide, is extensive and thus provides a reference unit for lithological mapping (fig. 4). The quartz-garnet-mica schist is heavily folded (F1-F3), refolded (F3) and cut by several granitic (quartz) pegmatite dykes and quartz-carbonate veins. The quartz-garnet-mica schist is also cut by several ductile and semi-ductile shear zones.

Brown and orange colored iron oxide also occurs in secondary, axial planar cleavage within vertical D3 folds in the area (fig. 5a). The main target for this master thesis is a similar, meter-wide, semi-ductile shear zone, containing quartz and iron rich carbonate with subsidiary chlorite (fig. 5b). This study attempts to resolve the relationship of these veins to the polyphaser D1-D3 deformation fabrics. One model is that the vein may be part of a fan-shaped architecture of steep shear zones that formed axial planar to the macro- and meso-F3 vertical folds in the area or alternatively, are younger and post-date all the ductile phases (see discussion).

Figure 5. A) Brown and orange colored iron oxide occurring in secondary axial planar within vertical D3 folds. B) 1 meter wide ductile shear zone containing quartz and iron-rich carbonate.

1.7 Definitions and terms

Shear zone – the ductile analog to a fault	A zone of ductile deformation between two undeformed blocks that have suffered relative shear displacement.
Ductile	A tenacity descriptor of a mineral that can be drawn into a wire.
Mylonite	A fine-grained, foliated fault rock with a recrystallized texture with 50-90% matrix and a strong lineation caused by shear in a major ductile fault or shear zone.
Mineralization	An assemblage of minerals associated with economic benefits and in this case precious elements and iron-sulfides
Metasomatism	A metamorphic process in which the chemical composition of a rock is changed significantly, usually as a result of fluid flow.
Metamorphism	The process by which rocks are changed by the solid-state application of heat, pressure and fluids to change the mineralogy of the rock.
Metamorphic phases	A group of rocks that reached chemical equilibrium at the same pressure and temperature range of metamorphism and characterized by specific mineral assemblages.
Schistosity	Wildly used term for a course grained foliation thought to be secondary in origin. A foliation produced by deformation, with preferred orientation and in which tabular minerals are course enough to be visible to the naked eye.

Porphyroblast	A large nicely developed mineral grain within a fine-grained matrix formed during metamorphic recrystallization.
Grain boundary migration recrystallization	The highest temperature form for recrystallization in quartz grains. At high temperatures between 500-700⁰C quartz grains are completely recrystallized with highly interfingering boundaries and grain boundaries are free to sweep across entire grains.

2 Methods

2.1 Mineralogical phase analyses (XRD)

X-ray powder diffraction (XRD) is mostly used to identify unknown crystalline materials like clay minerals, which are hard to identify petrographically. Mineralogical phase analyses (X-ray powder diffraction, XRD) were conducted at Department of Mineralogy and Petrography, Faculty Science, University of Zagreb. Measurements were performed on Philips PW 3040/60 X'Pert PRO powder diffractometer (45 Kv, 40 μA) with CuKα monochromatised radiation (λ=1,54056 Å) and $\Theta-\Theta$ geometry. Area between 4 and 63⁰ 2Θ with 0.02° step, was measured with 0.5° primary beam divergence. Compound identifications were based on computer program X'Pert High Score 1.0B and literature data. Unit cell parameters were calculated with the least-square refinement program UNITCELL (Holland and Redfern, 1997).

2.2 Scanning Electron Microscope

For this master thesis, SEM and EBDS analysis were performed on a Zeiss Merlin field emission scanning electron microscope (FE-SEM) in the electron microscopy laboratory at the Faculty of Health Sciences, UiT The Arctic University of Norway. The Zeiss Merlin is equipped with several detectors; An energy-dispersive spectrometer (EDS), a wavelength dispersive spectrometer (WDS) and an electron back scatter diffraction (EBSD) detector. The samples was lightly, carbon coated of approximately 3nm to reduce surface charging effects.

Working beam distance of 8.5 mm, using a 3-40 µm beam, accelerating voltage of 20 kV, emission current of 45 mA and counting time of 100-200 seconds and data were further processed in AZtecEnergy software. The SEM was used to preform point analysis, linescans and maps, mainly measuring the high-energy backscattering electrons (BSE) to collect chemical data about the rocks. The EBSD was used to map the contact between the hydrothermal vein and altered host rock.

2.3 Electron Backscatter Diffraction (EBSD)

This technique is based on the scanning electron microscope (SEM).

The crystalline sample was tilted 70 degrees from horizontal position inside the microscope chamber. A beam of high-energy electrons are shot towards the crystalline sample (Schwartz et al., 2000). The beam reaches approximately 20nm deep into the sample. EBSD patterns are created by scattering of the entering electrons within the crystal structure on different lattice planes (Neufeld, 2007), and the patterns are generated on a phosphorous screen by the backscattered electrons (BSE) from the sample. The backscattered electrons forms a so-called Kikuchi pattern (Kikuchi, 1928). The Kikuchi can be interpreted as a projection of the crystal lattice at phosphorus screen. The diffraction pattern is used to measure crystal orientations of different crystals and to identify them (Schwartz et al., 2000).

2.4 Chlorite geothermometry

The chemical compositions for the chlorite was determined in selected samples from syn/post-D3 shear zones and post-D3 shear zones by point SEM/EDS analyses. Samples TMF 002 and TS (TMF 015) contain chlorite from the syn/post-D3 shear zone, and sample TMF 016 contains chlorite from the post-D3 shear zone. Chemical composition of analyzed chlorites was recalculated to oxide composition and Winccac software (Yavuz et al., 2015) was used. The software is created to estimate temperature-dependent cation site-allocations at the different structural positions such as the tetrahedral, octahedral and interlayer sites (Yavuz et al., 2015). Various chlorite geothermometers are carried out to specify the conditions of formation temperature (Yavuz et al., 2015). Two chlorite analysis was chosen to estimate temperature formation of the chlorites:

1) Chlorite geothemometer by Cathelineau, 1988, is based on an empirical calibration between the tetrahedral aluminum occupancy in chlorites and measured temperature in geothermal systems, This geothermmometer has a wide application in diagenetic, hydrothermal and metamorphic settings (Yavuz et al., 2015).

2) Chlorite geothermometer by Kranidiotis and MacLean, 1987, is also an empirical geothermometer based on the tetrahedral aluminum occupancy and Fe/Mg ration in analyzed chlorites. This geothermometer can be applied to conditions where chlorite is associated with other aluminous minerals (Yavuz et al., 2015).

2.5 Polarization Microscopy & Reflected Light Microscopy

Petrographical descriptions of the thin sections were done using the microscope Leica DM4500P. Transmitted light and reflected light was used with plane- and cross-polarized light to identify the minerals. All thin sections contain silicates of various kinds, toghether with opaque minerals such as oxides and sulfides. A camera placed on the Leica DM4500P, was used to take pictures of the thin sections. CorelDraw was used to process the pictures, and making figures.

2.6 Isotope Ratio Mass Spectrometer (IRMS)

Stable isotopes of carbon and oxygen where analyzed using the isotope mass spectrometer, Thermo Scientific Flash 2000.

The amount of sample analyzed in the gas bench, should be around 50 mg for each sample. Samples are placed in 4, 5 mm glass tubes and placed in the gas bench for analyzing. The bench holds a consistent temperature of 50ºC. First the samples gets flushed with helium to push out all air that could exists in the sample. Adding phosphoric acid (H_3PO_4), samples are converted to simple gases such as H_2, CO_2 and N_2(Carter and Barwick, 2011). The acid has to react with the carbonate for at least two hours and longer is recommended. Phosphoric acid is added a second time and measures the CO_2. Then the gas is dried before it enters the mass spectrometer. Inside the mass spectrometer an electron canon shoots electrons on the CO_2 molecules and some electrons leaves the CO_2 molecule and the remaining are positive charged CO_2^+ ions. An electric field on 10000 V accelerates the ions into a high velocity. Several lenses inside the mass spectrometer focuses the ion beam as narrow as possible before entering the electromagnet. The electromagnet reacts with the electric field of the CO_2^+ ions, so their electric

field corresponds. The IRMS measures the ratio of ions that corresponds to the CO_2 gasses. For example, in the analysis of carbon isotope ratios, the mass spectrometer monitors ions with mass to charge ratios (m/z) of 44, 45 and 46 (g/mol) which corresponds to the ions produced from CO_2 molecules containing ^{12}C, ^{13}C, ^{16}O, ^{17}O and ^{18}O in various combinations (Carter and Barwick, 2011). The ratios of these molecules are always measured relative to an isotropic standard in order to eliminate any bias or systematic error in the measurements (Muccio and Jackson, 2009). These standards are linked to internationally recognized standards such as PDB for carbon and SMOW for oxygen. Isotope ratios for samples of interest are reported in the delta notation, δ:

$$\delta = \frac{1000(R_{sample} - R_{standard})}{R_{standard}}$$

2.7 Fluid inclusion Microthermometry

Samples for fluid inclusion microthermometry were taken from rock sample TMF 006. This sample consists of nearly pure hydrothermally precipitated quartz. Microthermometric measurements of fluid inclusions were performed at the Department of Geosciences, UiT The Arctic University of Norway. Double polished ~0.25 mm thick, transparent mineral wafers were used. Measurements were carried out at Linkam THMS 600 stage mounted on an Olympus BX-2 microscope using 10x and 50x Olympus long-working distance objective lenses for visible light. Two synthetic fluid inclusion standards (SYN FLINC; pure H_2O and mixed H_2O-CO_2) were used to calibrate equipment. The precision of the system was ±2.0°C for homogenization temperature, and ±0.2°C in the temperature range between –60 and +10°C.

Following procedures outlined by (Shepherd et al., 1985): temperature of homogenization (T_H), temperature of decripitation (T_D), temperature of CO_2 homogenization (T_H^{CO2}) and melting temperature for clathrate (T_M^{clath}) were measured in the case of the three-phase CO_2-rich inclusions present in all samples.

There are several ways to classify fluid inclusions, but the most important one relates to the timing of formation of the inclusion relative to the host mineral.

Primary fluid inclusions are formed during the formation of the crystal and are very good indicators for conditions during crystallization of the host minerals. They are generally trapped along the growth zones of crystal phases. Primary inclusions are usually isolated and occur at

distances more than 5 times the inclusions diameter (Shepherd et al., 1985). To make sure that the other fluid inclusions in close relation to the fluid inclusion of interest are the same, it is important to look at the variation of the degree of fill in fluid inclusion assemblages. If the inclusions in close relation have a constant liquid to vapor ratio, the inclusions in close relation to the one of interest can be classified as cogenetic. Primary inclusions are usually large in size relative to the host crystal. Another way to try to establish which inclusions came first is to look at the size of the gas bubble with in the fluid inclusion. The bigger the gas bubbles are, the higher temperature was the inclusions entrapped in (Shepherd et al., 1985).

2.8 Raman Spectrometry

Raman spectroscopy is a spectroscopic technique that provides a structural fingerprint of analyzed molecules. It applies Raman (inelastic) scattering of monochromatic light, usually from a laser beam within the visible, near infrared, or near ultraviolet range. Raman spectroscopy was performed at the Department of Earth Science, The Faculty of Mathematics and Natural Sciences, University of Bergen. A JobinYvon LabRAM HR800 confocal Raman spectrometer equipped with a frequency doubled Nd-YAG laser (100 mW, 532.2 nm) and a LMPlan FI 100x objective lens (Olympus) was used to identify chemical composition of volatile phases hosted by fluid inclusions. Measurements were conducted on same double polished mineral wafers that were used for microthermometry. Compound identifications were based on literature Raman spectra (Burke, 2001, Frezzotti et al., 2012, Frost et al., 2012)

3 Field relations of bed rocks and structures in the study area

3.1 Introduction

The coastal area near Småsandnesset (Fig. 3) was mapped and studied in detail during this work with the goal to describe the various lithologies and structural relationships, and in particular, enable to characterize the shear zones that host the hydrothermal quartz and calcite veins and mineralization. The area was previously mapped on a regional scale by Pedersen (1997 and Bergh et al. (2010). Three main tectonostratigraphic units occur in the mapped area (fig 6.): banded amphiboles, garnet-mica-schists and quartz-feldspatic pegmatites. In addition, mafic intrusions together with mylonitic/phyllonitic, mineralized and vein-bearing ductile shear zones are described. The shear zone localities, and samples collected for thin-section studies (table 1) are shown separately.
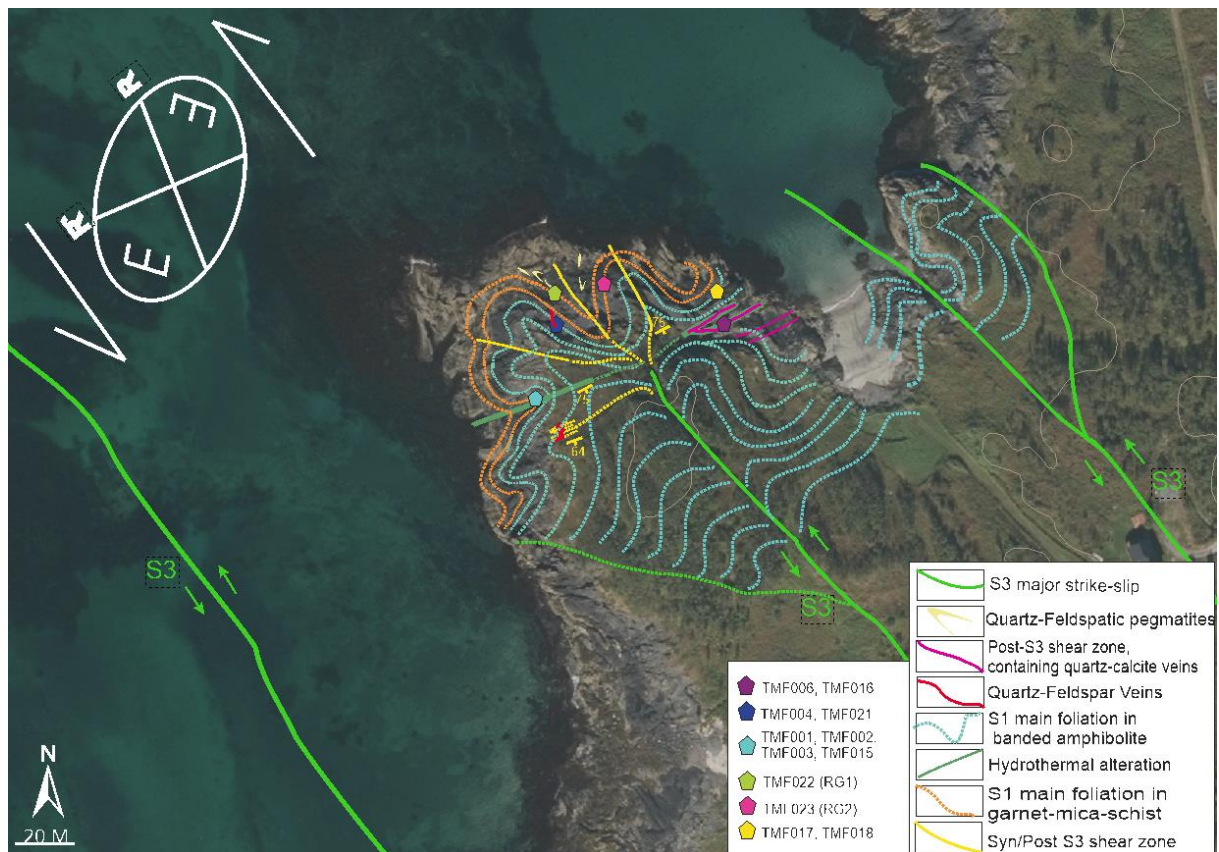
Figure 6. Detailed geologic and tectonic map of the Småsandnesset peninsula. Note the architecture of S3 shear zones oriented axial planar to the F3 folds.

3.2 Structural overview

The main host rocks and lithological units in the mapped area (see description below), contain a strong foliation which is referred to as the main foliation (S1). The main S1-foliation is partly mylonitic and axial-planar to isoclinal folds (F1) of presumed bedding, within foliation-parallel ductile shear zones. The main foliation is itself folded in macro scale, steeply plunging to sub vertical folds (F3) which is widespread in the mapped area (see chapter 1.4.3; Bergh et al. 2010). The axial surface associated with F3 folds strikes variably NW-SE to NE-SW and are generally, steeply dipping and overlap with steep ductile shear zones (see chapter 3.3.). These shear zones, striking parallel to the axial planar surface of the F3-folds in the area, comprise phyllonites quartz-carbonate veins, and also, potentially host mineralization (see chapter). Most of these F3 folds are asymmetric and S-shaped, indication formation during sinistral shear (see later discussion). The abundance of F3-folds and their geometries across the entire islet may infer that the F3-fold architecture is controlled by a larger structure (see discussion).

3.3 Ductile shear zones

Based on the structural study of D3 structures, two generations of ductile shear zones are identified in the study area, as marked on (fig.6). They include syn-D3 and syn/post-D3 shear zones relative to D3 structures. The two types of shear zones are oriented on opposite sides of each other but have the same strike direction. However, they are not possible to trace as one continuous shear zone, and therefore are separated as to different categories:

The first category likely represents syn-S3 semi-ductile shear zones (marked in yellow in the map). These shear zones are believed to be parallel to the axial surfaces of F3 folds and have NE-SW strike and steep attitudes. The main foliation (S1) in the amphibolite seems to be relatively unaffected by these shear zones and crosscuts the main foliation (S1), and the axial planes of macro scale F3-folds, supporting a syn-D3 relative age. The mineralogy in these shear zone seems to be relatively unaffected by these shear zones, but in close relation to these shear zones the banded amphibolite gradually changes into garnet-mica-schist. These shear zones shows both sinistral and dextral shear motion (Bergh et al., 2015)
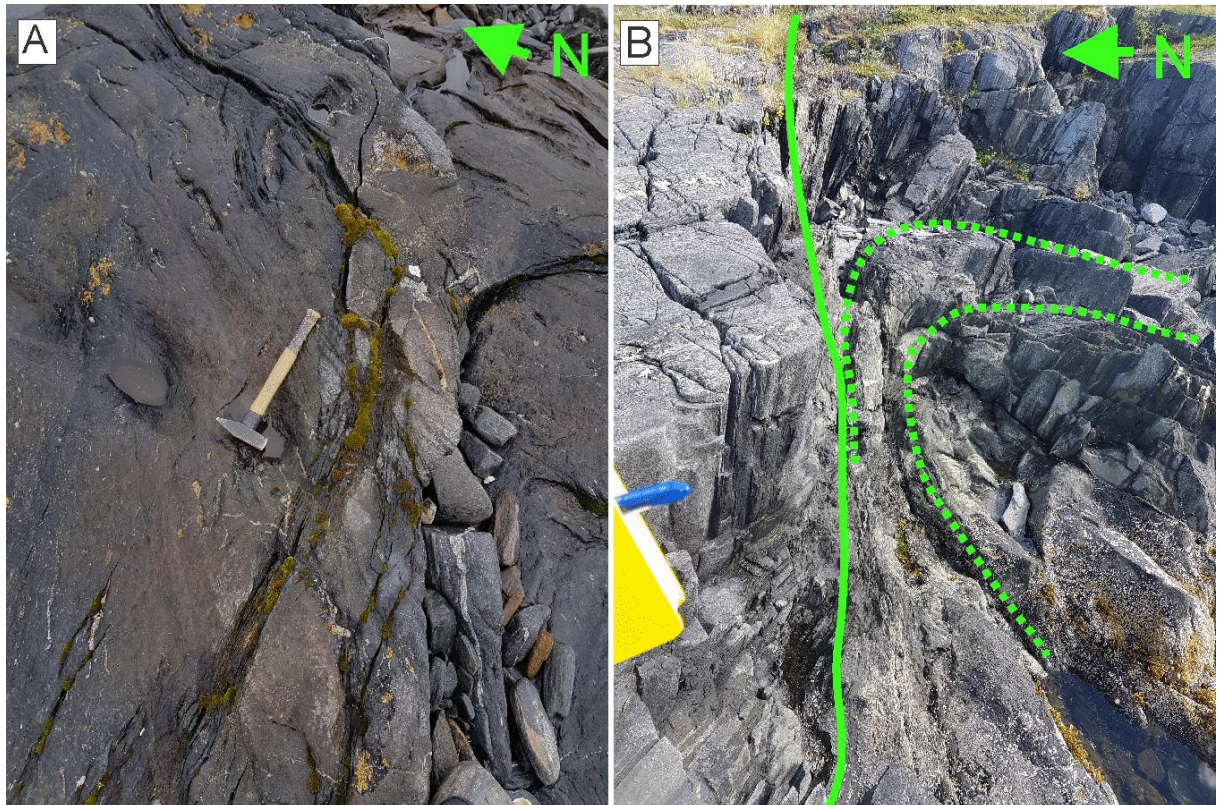
Figure 7. A) Semi-ductile character of the syn-S3 shear zones. B) Syn-S3 shear zone (green solid line) crossuting axial plane of F3 fold hinge (green stippled lines).

The second category of shear zones represents syn/post S3 (marked in green in the map) crosscuts the main foliation (S1) in the banded amphibolites, and the main foliation (S1) tends to bend in against these shear zones. The main schistose/mylonitic fabric (S3) in these shear zones strikes NE-SW, dips steeply, and consists of dominantly chlorite, and can therefore be classified as mylonitic/phyllonic. The retrograde alteration in these shear zones, and the presence of hydrothermally precipitated quartz and calcite supporting a syn/post D3 relative age.
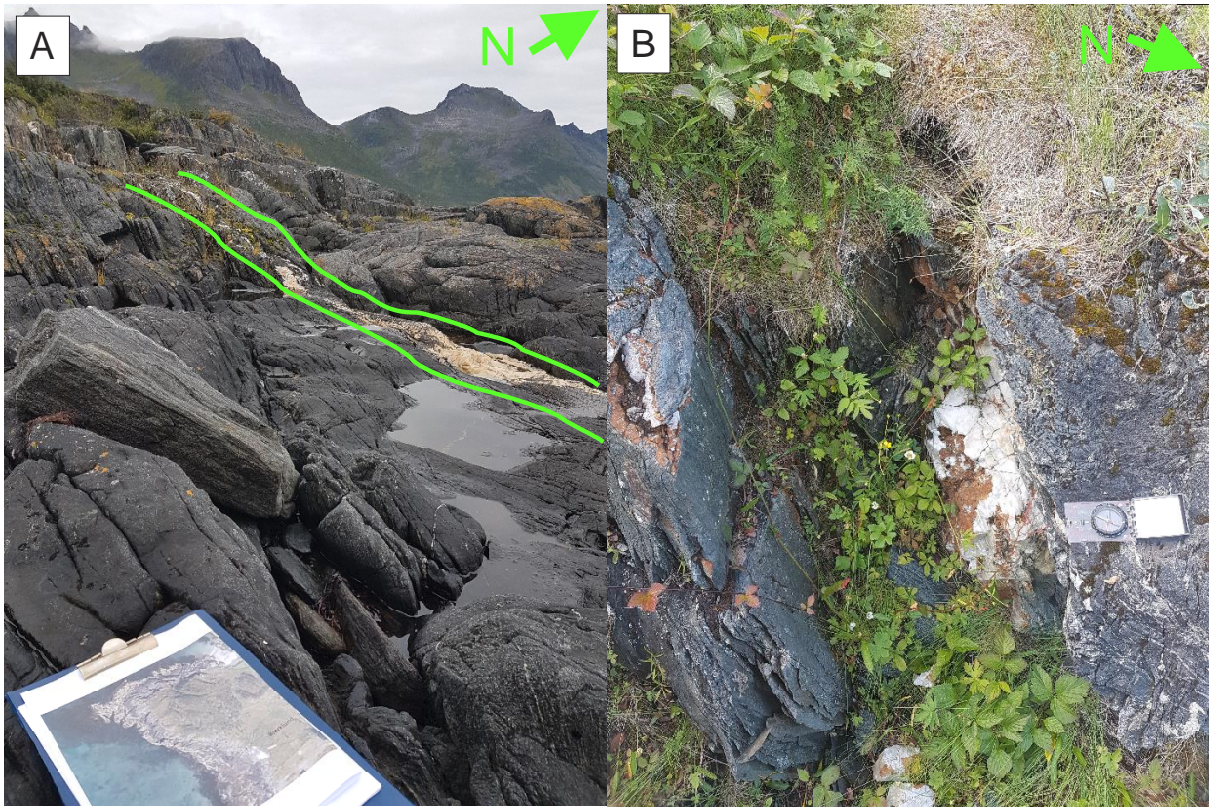
Figure 8. A) Mylonitic shear zone crosscutting the main foliation (S1) in the banded amphibolite. B) Quartz and carbonate veins in steeply dipping mylonitic shear zone.

4 Petrography

4.1 Banded Amphibolite

4.1.1 Field occurrence and hand specimen

The most widespread host rock type in the study area is a gray to almost black aphanitic banded amphibolite (Fig. 9). The banded amphibolite have a well-developed S1-foliation that is irregular and display smooth and rounded shapes of the bed rock surface (fig. 9). The banded amphibolite is mapped as a NW-SE striking continuous tectono-stratigraphic unit extending along strike all the way from Baltsfjord to Botnhamn in the south, with a thickness of several hundred meters (Pedersen, 1997). Banded and conformable massive amphibolites (dm- to meter-thick) are often interlayered. Along the entire mapped shoreline in Småsandnesset the amphibolites are strongly folded (fig. 6). The amphibolite is bounded by a conformable unit of rusty colored garnet-mica schist (fig. 6). Foliation-parallel quartz veins in the banded amphibolites, form lenses that pinch out along strike, sometimes defining boudines. This suggests that the quartz lenses may have been originally continuous bands in a sedimentary

succession (Pedersen 1997). These quartz veins have not been sampled, but they are thought to have the same origin and age as the quartz-feldspar (pegmatitic) veins that where sampled (see later discussion). The layers of the banded amphibolite contain dm-sized mafic and felsic clasts often with angular shapes, while similar clasts present in banded and strongly foliated amphibolites define cigar-shaped features parallel to a stretching lineations on steeply dipping S1-foliation surfaces. Observed cigar-shaped clasts of both felsic and mafic composition of mixed clast shapes and sizes, most likely of volcanoclastic origin, supports the fact that the amphibolite is likely of metasupracrustal origin (cf. (Pedersen, 1997, Bergh et al., 2010).
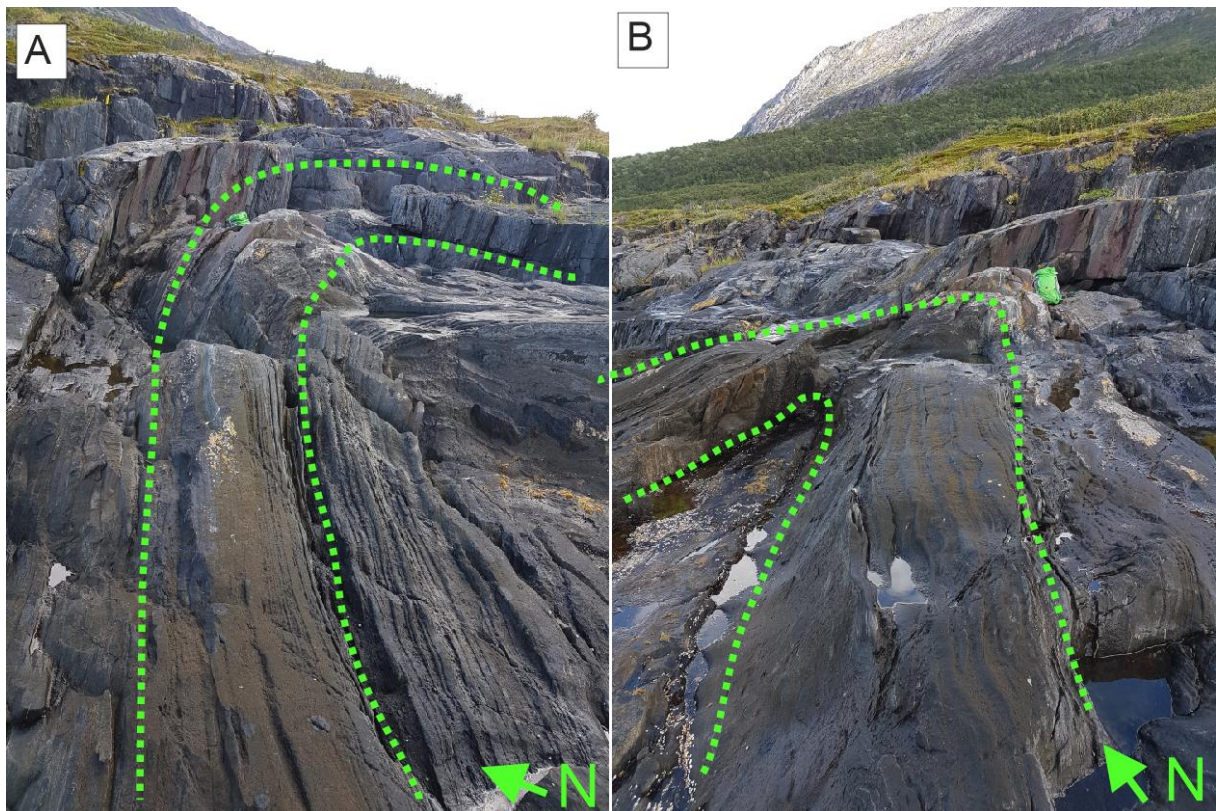
Figure 9. A) Steeply dipping main foliation (S1) of the amphibolite are folded in macro scale F3 folds. B) Macro F3 fold in banded amphibolite, axial-plane almost dipping vertically into the ground.

4.1.2 Mineralogy and texture

The banded amphibolite contains mainly hornblende, biotite, quartz and feldspar, with minor chlorite, titanite and subordinate garnet. Biotite, chlorite and hornblende grains defines the main ductile foliation (S1) in the banded amphibolite, which is composed of preferred oriented flaky, granoblastic polygonal crystals of hornblende, biotite and small amounts of chlorite grains in foliation surfaces (fig. 10). The preferred elongation and typical granoblastic polygonal nature

of the mineral crystals (fig. 10) suggests growth during ductile metamorphism. The mineral content vary due to presence of biotite-rich zones laterally in the rock. Some foliation parallel units of the amphibolite contain larger porphyroblast of biotite with random orientations and larger amount of clustered biotite, in contrast to a more massive banded rock where biotite crystals are smaller and not that abundant (fig. 10). These laterally changes of the rock composition could be due to various eruption products, for instance effusive versus extrusive products. Tiny titanite grains grows restricted to flaky, granoblastic polygonal biotite in the banded amphibolite (fig. 10a). This is believed to be a breakdown reaction related to biotite in the transformation to chlorite (see later discussion).
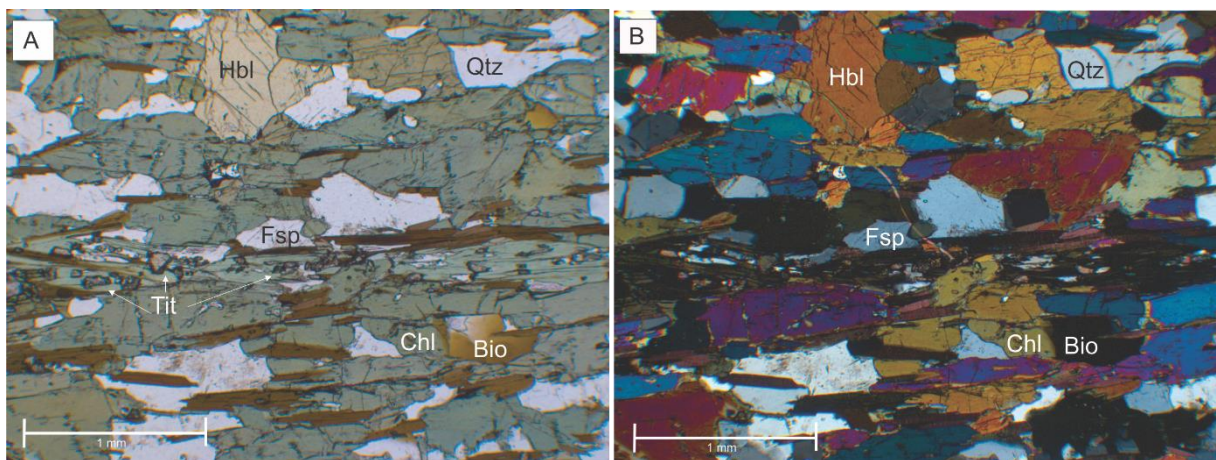
Figure 10. A) Banded Amphibolite in PPL. Consisting mainly of Hornblende (Hbl), Quartz (Qtz), Feldspar (Fsp), Biotite (Bio) and Titanite (Tit). B) Banded Amphibolite in XPL.

4.1.3 Reflected light

Opaque minerals tend to exist as several overlapping mineral phases of iron oxides and iron sulfides (fig. 11b). Pyrite occurs as separate grains, and is the most widespread opaque mineral in the banded amphibolite. Chalcopyrite and magnetite have been found in associations with pyrite. Hematite is observed along weathering rims of both pyrite and chalcopyrite grains. Titanite and tiny crystals of ilmenite can be observed as small grains spatially associated to biotite (fig. 11d)
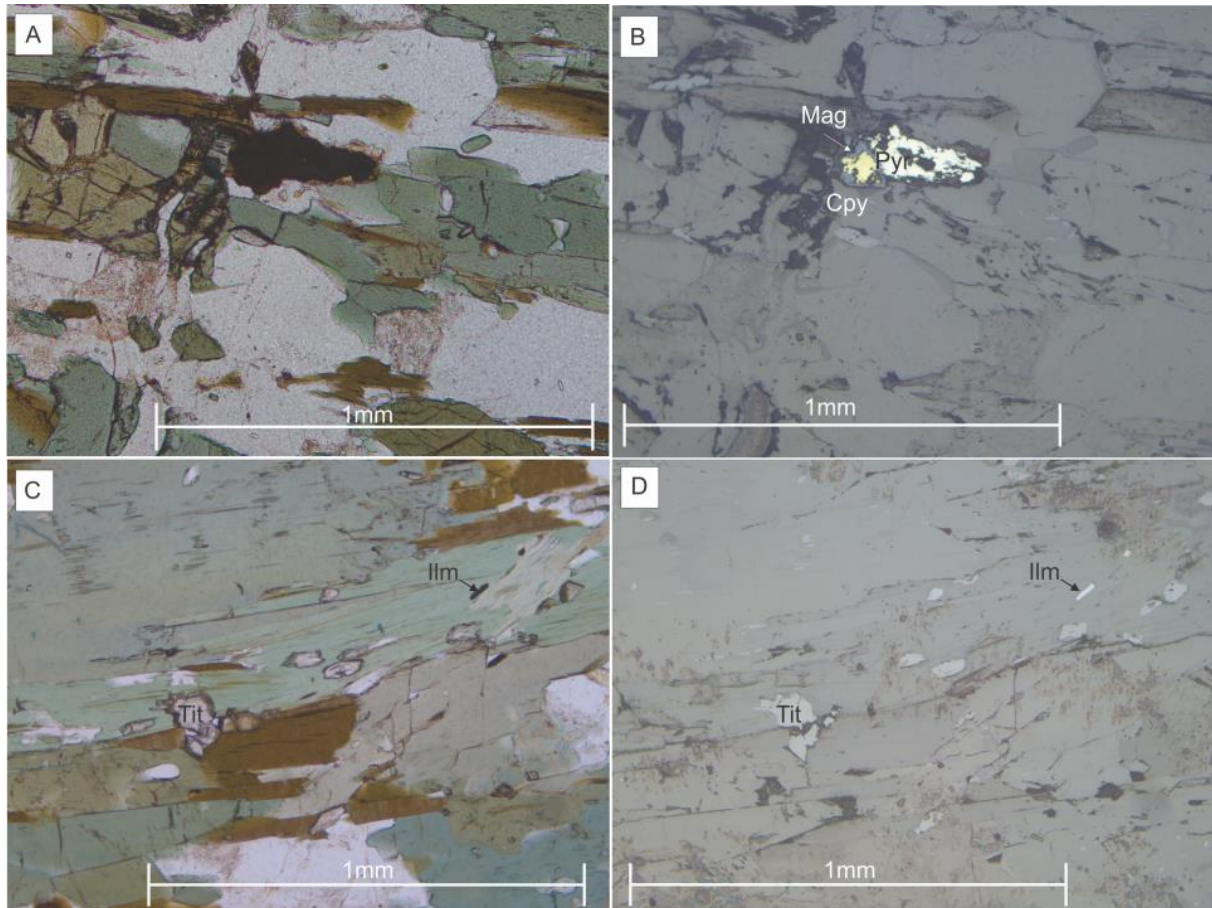
Figure 11. A) Opaque minerals in the banded amphibolite. B) Chalcopyrite, pyrite and magnetite in relation to biotite and hornblende. C) Titanite (Tit) and ilmenite (Ilm) in relation to biotite. D) Titanite (Tit) and ilmenite (Ilm) in reflected light.

4.2 Garnet-Mica-Schist

4.2.1 Field occurrence and hand specimen

A very distinct lithology consisting of rusty colored garnet-mica schist (gneisses), are mapped along the entire shoreline from Bjørklund to Småsandnesset (fig. 6). The distinct rusty color therefore makes it a suitable lithostratigraphic leader horizon (fig. 12a). The thickness of the mapped unit vary laterally, from 10-25m (Pedersen, 1997), but thickness cannot be estimated fully, since the contact to the surrounding rocks is in the fiord. There is also a thicker unit of garnet-mica-schist which extend from Småfluan in Baltsfjord all the way to Botnhamn in the south (fig. 4). This lithological unit is ca.150-400 m thick (Pedersen, 1997). The rocks have a well-developed S1-foliation and a rusty brown color due to high concentrations of iron-hydroxide or accessory minerals like magnetite (Pedersen, 1997). Rusty colors can be observed both in hand specimen as well as in thin sections (fig. 13a). The contact between the garnet-mica-schist and the surrounding banded amphibolite's is always conformable and parallel to

the main S1 foliation (fig. 12b). The main S1 foliation of the garnet-mica-schist vary a lot in geometric character, from gneissic layers to penetrative, as well as in orientation (fig. 4). This unit is folded by F3-folds in a similar manner as the surrounding amphibolites and cut by ductile S3-shear zones (fig. 4). In some areas the garnet-mica-schist are more intensively foliated, in other the garnet-mica-schist are more competent and dominated by silica-rich minerals (Pedersen, 1997), and up to cm-sized garnet crystals may be present (fig. 13c).
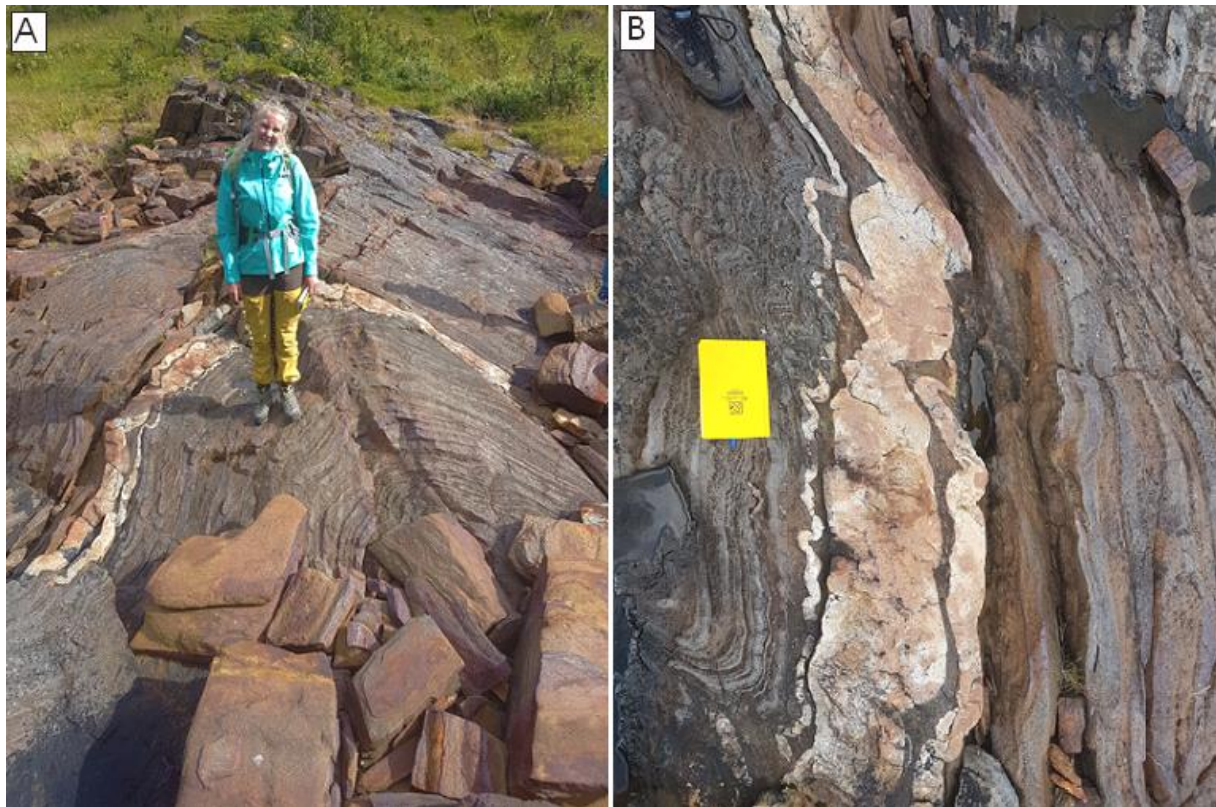
Figure 12. A) Rusty garnet-mica schist folded in a macroscale F3 fold. B) Quartz-Feldspar? (pegmatitic) vein intruded parallel to the main foliation (S1). Notice the change in color on each side of the pegmatitic vein.

4.2.2 Mineralogy and texture

Thin sections made of the garnet-mica-schist shows dominantly hornblende, quartz, garnet, feldspar and leucoxene (iron oxide+titanium oxide). The rusty rims surrounding weathered mineral grains indicate a general high iron content in the garnet-mica-schist (see discussion). In the garnet-mica-schist there were found possibly two generations of garnets, one generation of garnets aligned parallel to the S1 foliations (fig. 13a), the second type of garnets where very large (up to 3 cm) of single porphyroblast crystals (fig. 13c). The larger garnets are part of the S1 main foliation, but appears to have grown across. Porphyroblast garnets are in the thin sections observed as polycrystals, intergrown with each other. This may explain the locally, very large size of observed garnet grains. Grains of hornblende are relatively smaller than in

the garnet-mica-schist, compared to those observed within the amphibolite. The collected samples have small contents of mica in general, and puts a question mark if this really is a separate lithology, due to its similar mineralogy and conforms boundary to the banded amphibolite. In the garnet-mica-schist, the main foliation (S1) are defined by flat hornblende grains in a preferred orientation (fig. 13a).
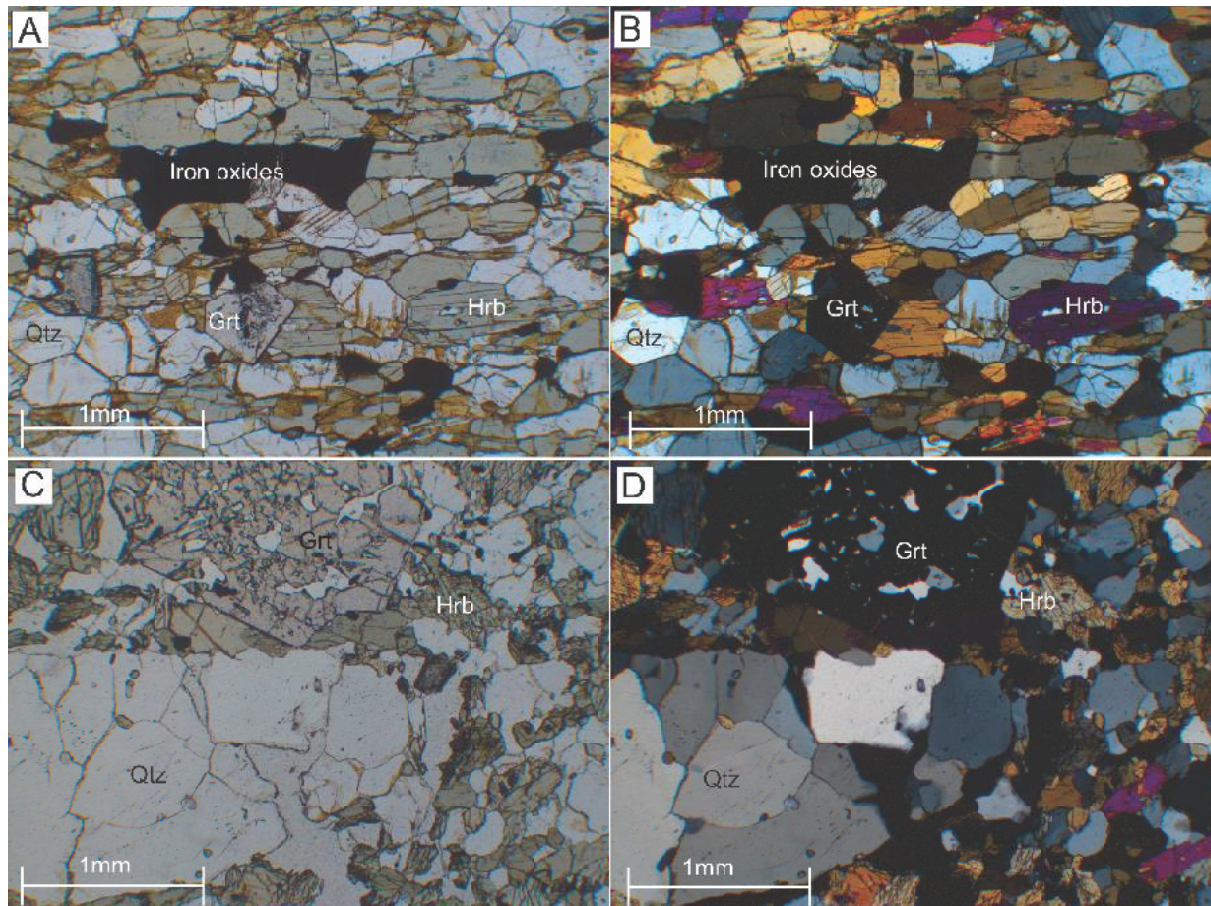
Figure 13. A) Relatively elongated grains of chlorite defines the main foliation (S1) in Rg1. B) In XPL the first-order interference colors reveals that much of the hornblende grains is transformed into chlorite. C) Large porphyroblast garnets and infiltration of quartz grains in Rg2. D) Bands of quarts defines the schistosity in Rg2. Porphyroblasts of garnet grows in the matrix consisting of fine-grained hornblende, quartz and feldspar.

4.2.3 Reflected light

Mainly iron oxides, pyrite and ilmenite are present as opaque minerals within the garnet-mica-schist. Clusters or traces of very fine grain opaque minerals with a rusty color are common. Mixtures of iron oxides are the most common mineral assemblage within the garnet-mica-schist. Ilmenite can be seen growing on top of or beside iron oxides (fig. 14b), but also as tabular crystals separately throughout the sample have been found (fig. 14d). Weathering of pyrite

crystals, is commonly observed within the garnet-mica-schist as yellow, orange and deeply red colors on top of or within the pyrite grains (fig. 14c).
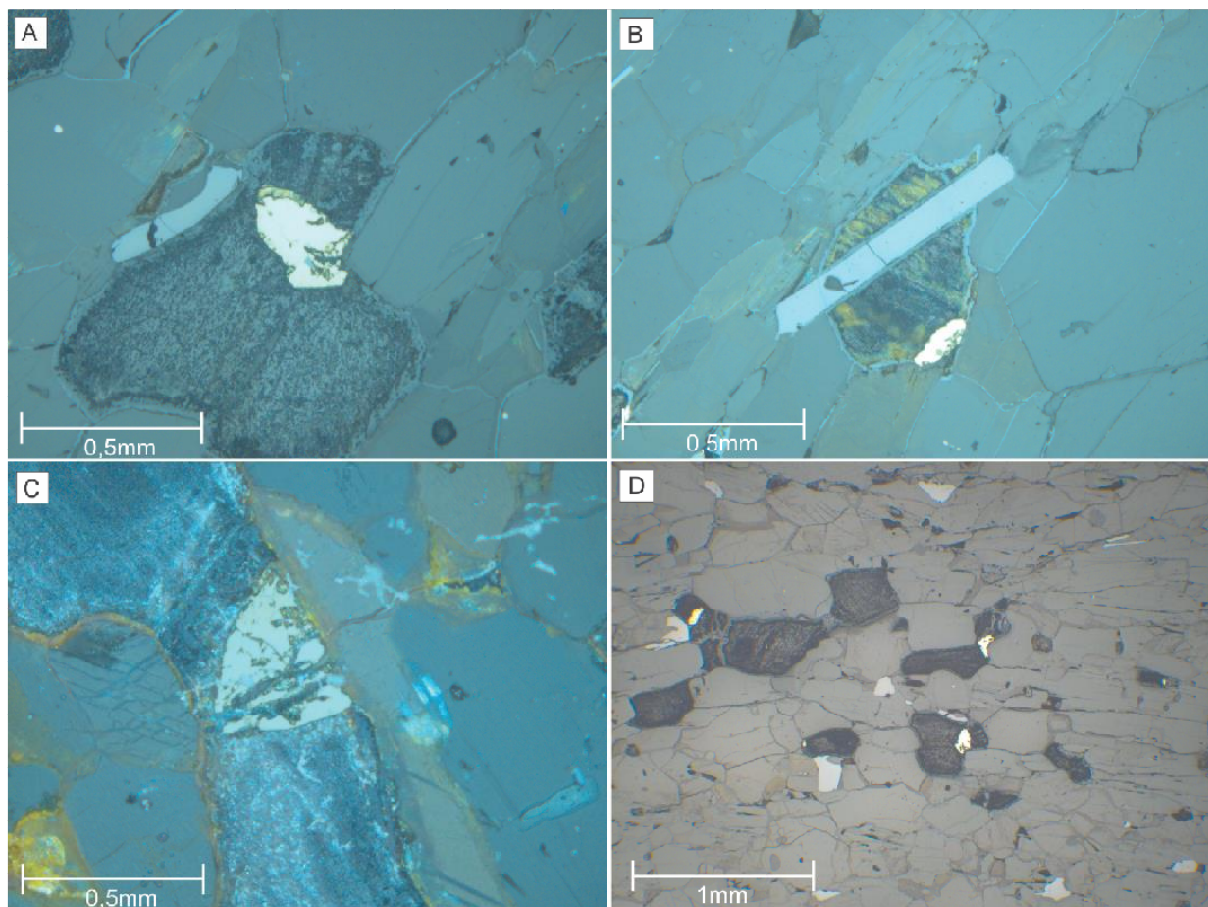
Figure 14. A) Large grains of various iron oxides, growing together with pyrite and ilmenite. B) Prefect tabular ilmenite crystal growing on top of iron oxides. C) Iron oxides surrounding a heavily leaching pyrite grain. D) Iron oxides widespread within the GMS together with separate ilmenite grains.

4.3 Quartz Feldspatic Pegmatites

4.3.1 Field occurrence and hand specimen

Felsic and granitic pegmatite dykes are widespread in the study area. They vary a lot in thickness and lateral extent (fig. 15b), and some are mapped for several hundred meters along strike by (Pedersen, 1997). Observed pegmatites at Småsandnesset mostly define dm-thick dykes that are parallel to the main foliation of the amphibolites and garnet-mica schists (fig. 15a). The pegmatites are not continuous units and they rather appear as lenses that are folded together with the main foliation (S1). The alteration color these pegmatites in field are pale white, and fresh rock shows the same colors with bigger crystals of glassy crystals (ie. quartz).

Figure 15. A) Note the gradual change in composition from amphibolite in the left side, to granet mica schist in the right side in relation to pegmatite. B) Pegmatites mainly following the main foliation (S1) in the amphibolites.

4.3.2 Mineralogy and texture

Thin sections of sampled veins reveals the veins consists mainly of quartz and feldspar crystals, together with some calcite (fig. 16a). Calcite crystals grow as smaller grains across the feldspar grains (fig. 16b). Quartz crystals show only weak dislocation of their crystal lattices (fig. 16a).
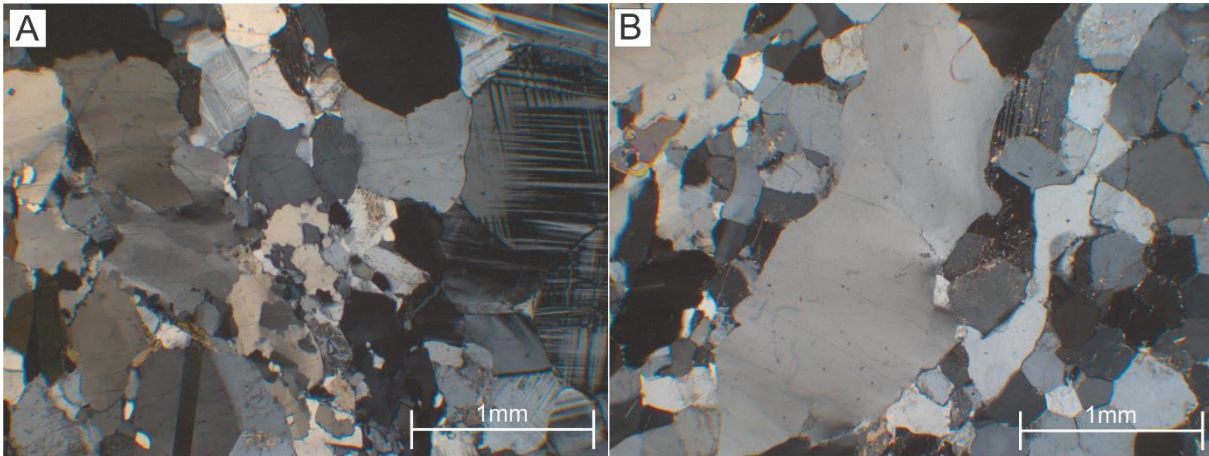
Figure 16. A) Various sized quartz crystals side by side with microcline crystals. B) Large quartz grain surrounded by small crystals of feldspar.

4.4 Magmatic Quartz-Feldspar Veins

4.4.1 Field occurrence and hand specimen

Quartz-feldspar veins are hosted with the banded amphibolite. The veins are widespread within the banded amphibolite and occurs as ptygmatic folds in many locations (fig.17a). The minerals representing the veins appears as sandy grain-sized material with a greasy white color and traces of rust surrounding the veins. Thickness and prevalence of the veins are various. The magmatic veins are not following the main foliation (S1), and the veins also crosscut it the main S1-foliation (fig. 17b).
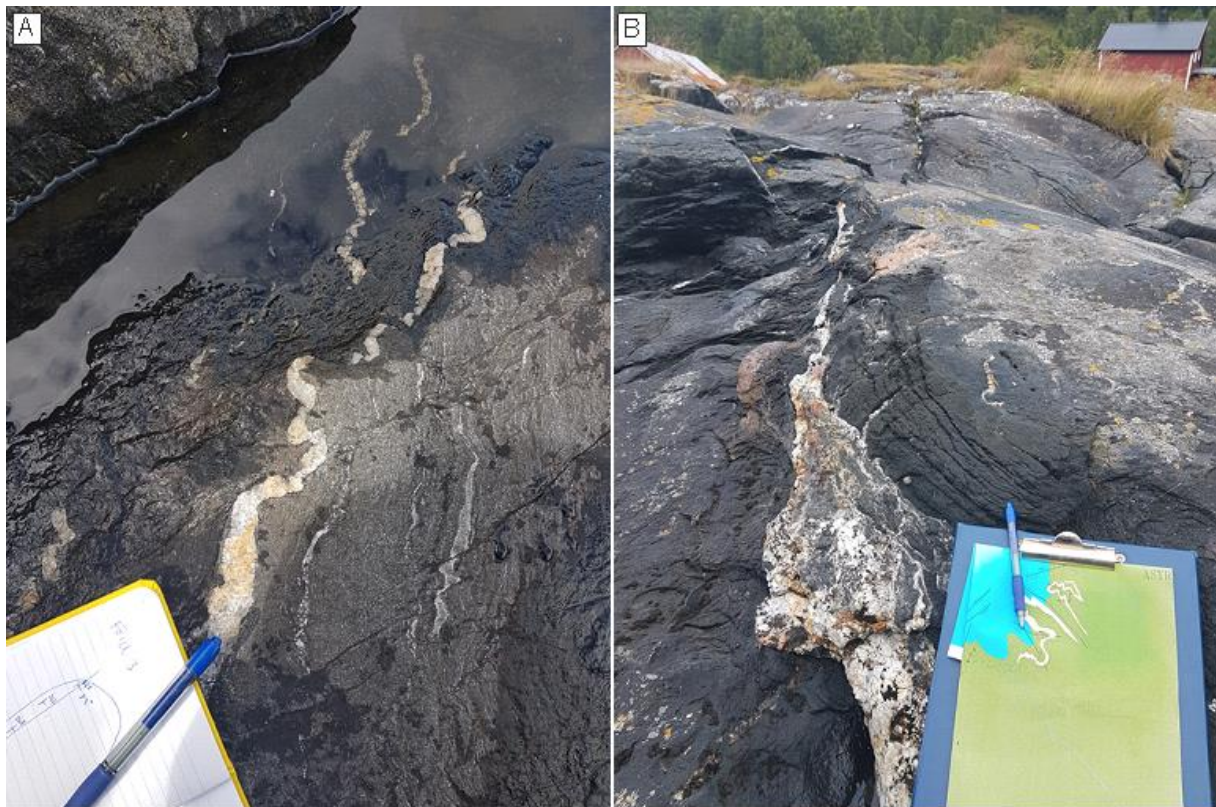
Figure 17. Ptygmatic quartz-feldspar veins in the banded amphibolite. The quartz-feldspatic veins mostly follows the main foliation (S1) in the banded amphibolite but with some ptygmatic character. B) Exsolution features of quartz-feldspatic veins in relation to amphibolite. Immiscible segregation of possibly quartz-feldspatic veins in banded amphibolite.

4.4.2 Mineralogy and texture

Thin sections of sampled veins reveals the veins consists of quartz and feldspar crystals, together with some calcite. Calcite crystals grow as smaller grains across the feldspar grains or in matrix between larger feldspar grains (fig. 18a). Patch-Perthite have been observed within the feldspar grains. Patch-perthite is characterized by albite and microcline rich regions (patches) with both regular and irregular outlines (fig. 18b). Observed melt inclusions within

these veins reveals that the veins have a magmatic origin (fig. 19a). The matrix surrounding the veins consists of fine-grained hornblende, quartz, iron-oxides and titanite.
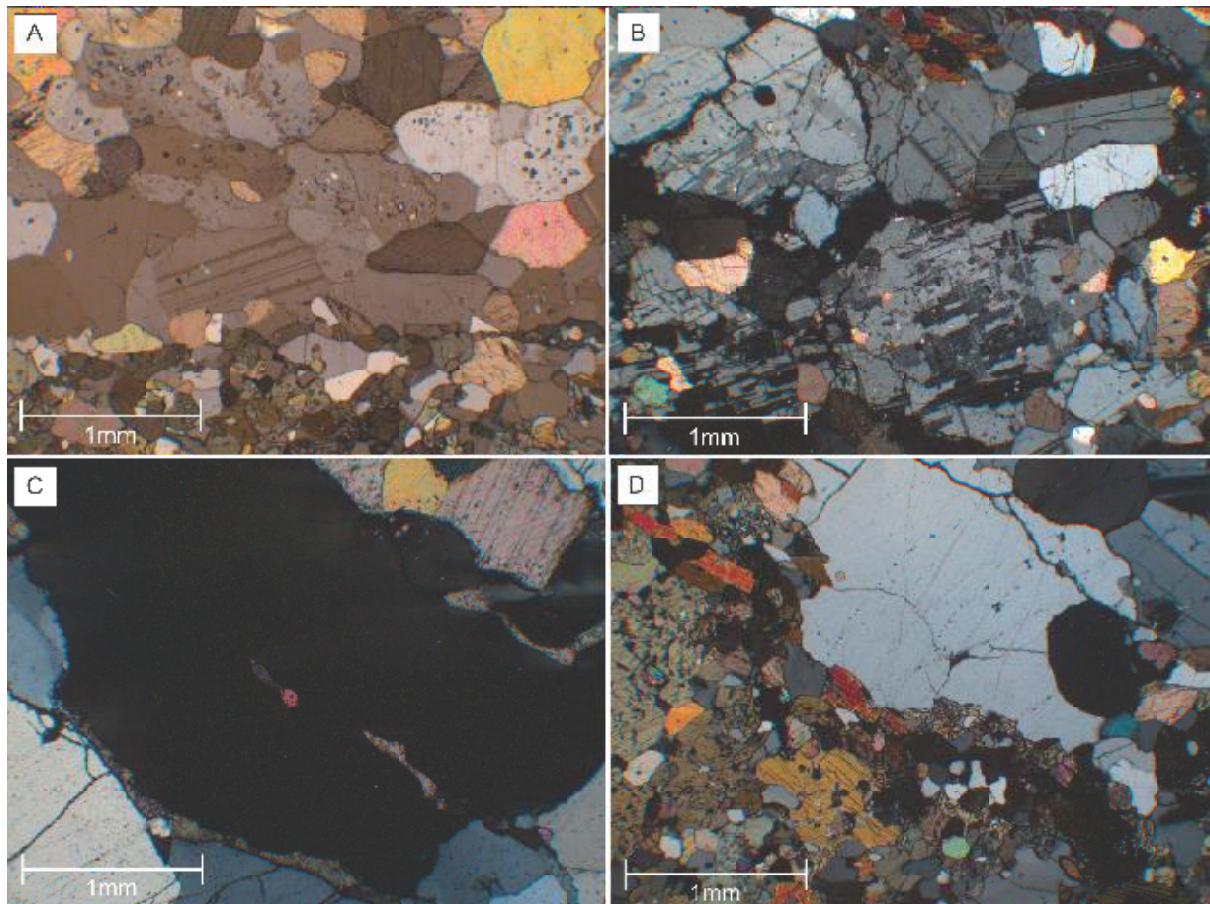
Figure 18. A) Small calcite crystals growing on top of feldspar crystals. B) Patch-perthite in large feldspar crystals.
C) Quartz crystals shows weak dislocation of crystal lattice. The same can be seen in quartz-feldspatic pegmatites.
D) Huge quartz crystal in contact with the amphibole.
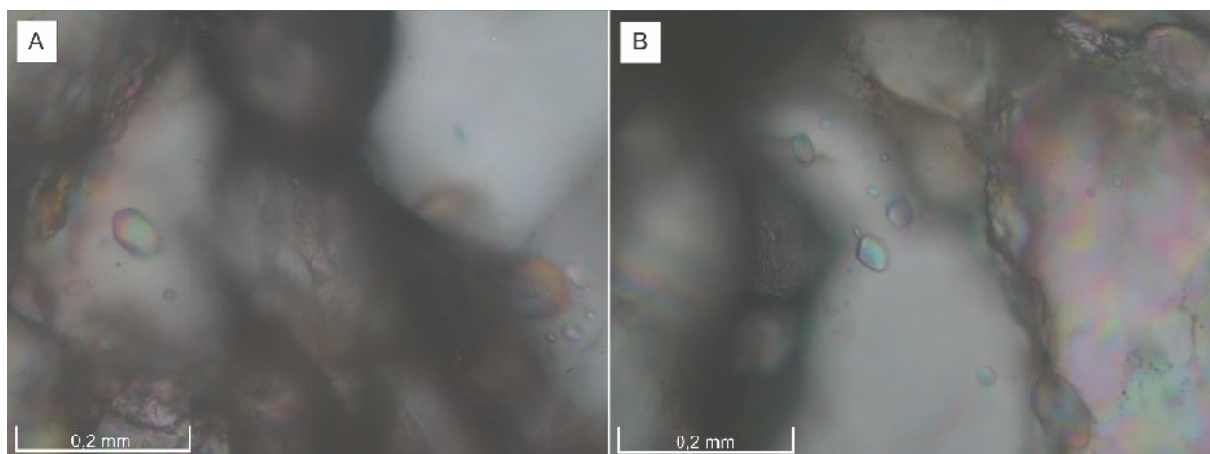
Figure 19. A) Various size of melt inclusions inside quartz crystal. B) Melt inclusions is widespread within the quartz crystals.

4.5 Mafic mylonites (phyllonite)

4.5.1 Field occurrence and hand specimen

Several syn/post S3 shear zones with mylonitic fabric have been mapped in the study area at Småsandnesset (fig. 6). The mylonitic shear zones (approximately 1 m wide) comprise chlorite-rich schists with a ductile fabric containing hydrothermally precipitated carbonate and quartz (fig. 20b). The secondary fabric can be classified as a penetrative cleavage, in cases when they define distinct, narrow surfaces composed of flakey metamorphic chlorite and consistently crosscut the main S1 foliation. The mylonitic shear zones contains hydrothermally precipitated quartz and carbonate. The shear zones strikes in an NE-SW direction and have a steep almost vertical dip (fig. 21a).

Figure 20. A) Steeply foliation planes of chloritized shear zone fabric. B) Quartz, and carbonate clasts in association with chloritized fabric.

4.5.2 Mineralogy and texture

The mylonite mainly consist of chlorite, calcite and feldspar with minor amounts of quartz, biotite and tourmaline. Chlorite and biotite which occurs as bands penetrating the matrix are defining the foliation fabric in the shear zones (fig. 21a). The mylonites are also highly rich in carbonate, unlike the amphibolite where calcite cannot be found as a rock forming mineral, except in magmatic veins penetrating the banded amphibolite. The carbonate is fine-grained and distributed evenly throughout the shear zones (fig 21b). Tourmaline have been observed in

the mylonites as nicely rounded crystals (cross section) or elongated tabular crystals (longitudinal). Biotite and chlorite are surrounding the porphyrobasts of quartz and tourmaline making some of these clast perfect kinematic indicators (fig 21a), indicating sinistral simple shear. Grain boundary migration recrystallization is the dominant recrystallization process observed within the quartz grains (fig. 21b).
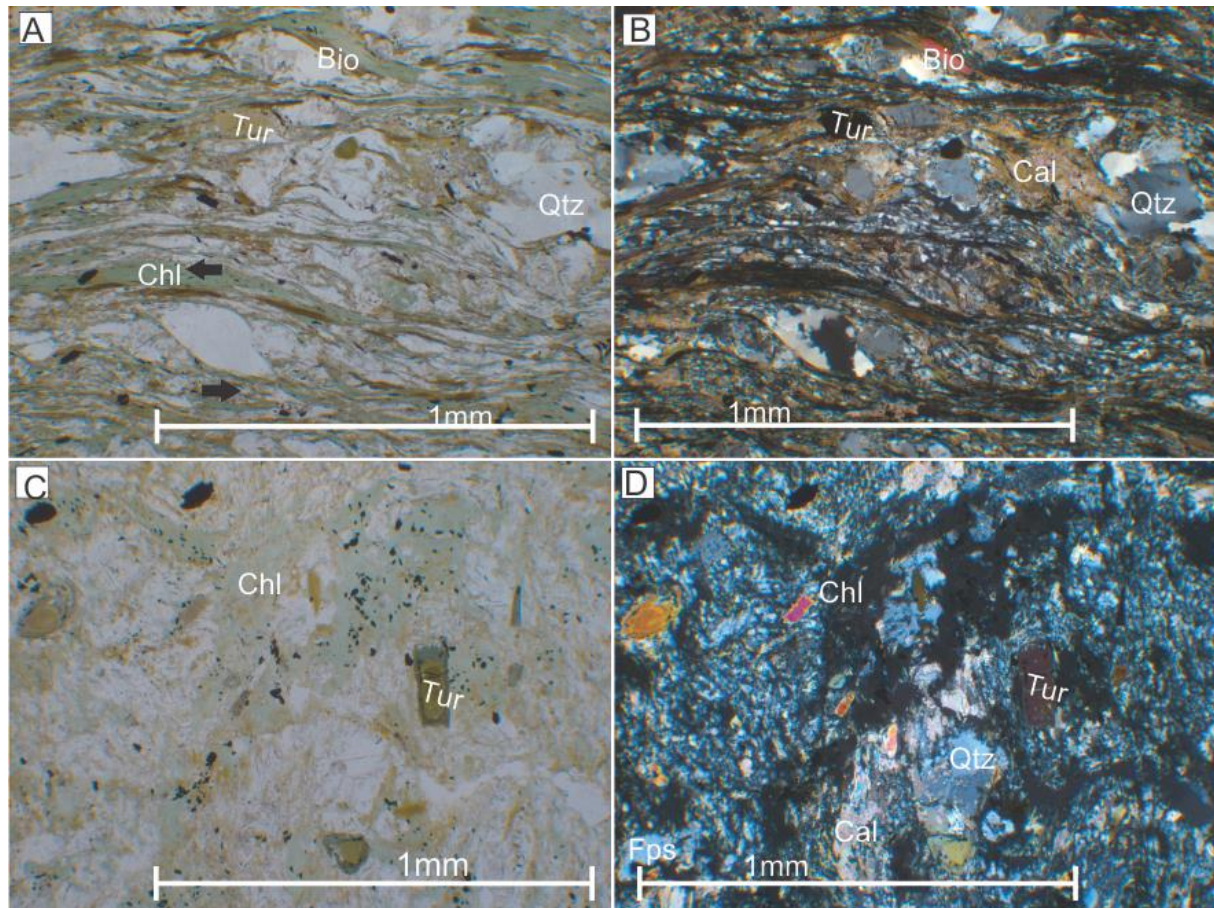
Figure 21. A) Sigmoidal clast showing sinistral simple shear. B) Mylonitic texture in the phyllonite. C) Turmaline crystals shows nice zoning. D) Calcite, chlorite, quartz and turmaline in a fine-grained matrix.

4.5.3 Reflected light

Ilmenite is much more abundant in the mylonitic shear zone in contrast to the banded amphibolite. Ilmenite is believed to be related to breakdown of biotite (fig. 22a), and can some places be seen surrounded by brown halo of a biotite trail (fig. 22c). Ilmenite is abundant everywhere where chlorite is distributed within the thin sections. Since chlorite is one of the biggest constitute in the mylonitic shear zone, and therefore ilmenite are quite abundant within the mylonitic shear zone.
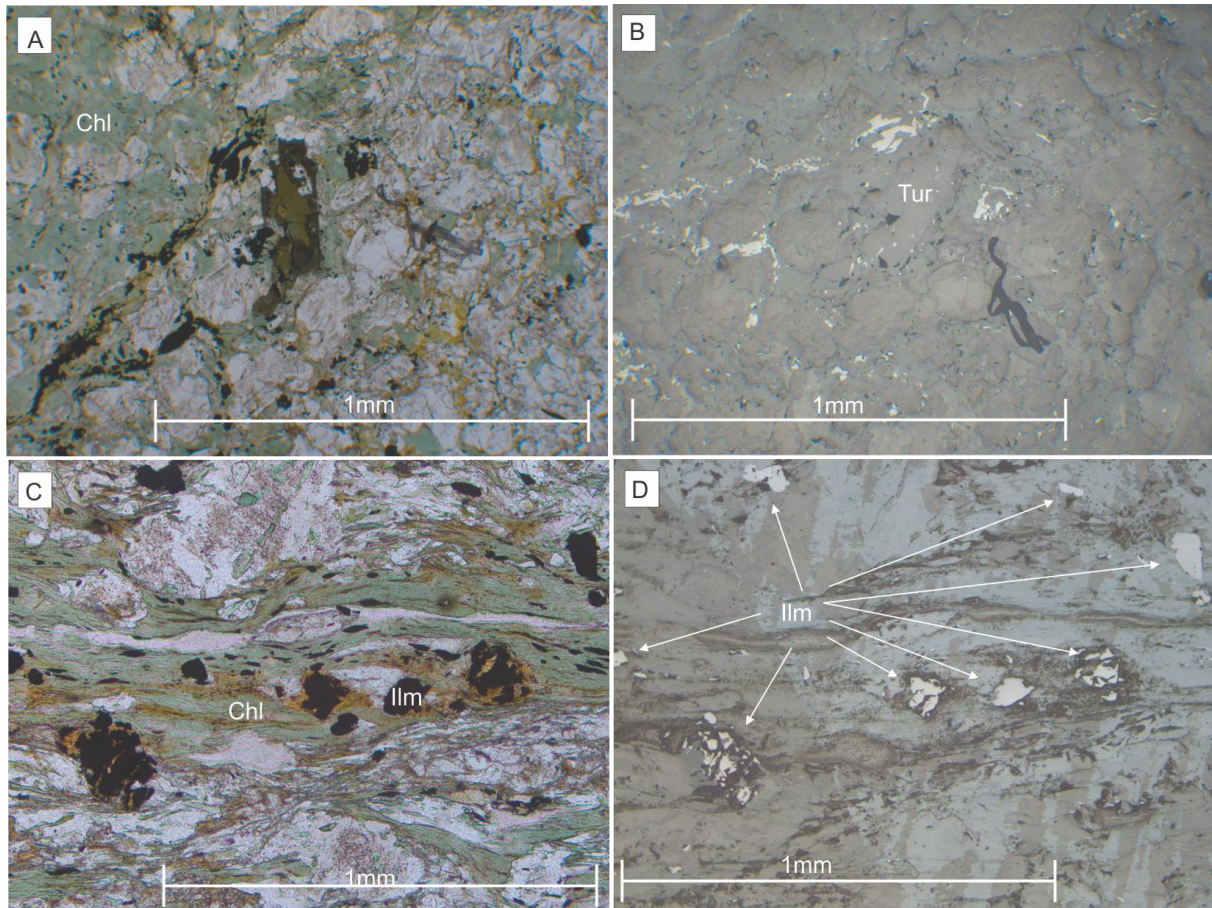
Figure 22. A) Tourmaline in a matrix of chlorite and albite. B) Tourmaline also contains minor inclusions of ilmenite. C) Ilmenite distributed within foliation of chlorite. D) Ilmenite distributed in the mylonitic shear zone.

4.6 Quartz-Calcite veins in shear zones

4.6.1 Field occurrence and hand specimen

Quartz-calcite hydrothermal veins are hosted in an approximately 1m wide mylonitic shear zone and the hydrothermal veins are believed to have been formed simultaneously in relation to the mylonitic shear zone (fig. 23a). The carbonate have an orange weathering color due to high concentration of iron within the carbonate (fig. 23b). Carbonate appears as extremely fine-grained brittle material surrounding the more massive interlocking quartz. The quartz in the hydrothermal vein has a pale white color.

Figure 23. A) Overview of chloritized ductile shear zone containing quartz and calcite veins. B) Chloritized steeply dipping foliation planes of chloritized shear zone containing quartz and calcite veins.

4.6.2 Mineralogy and texture

Quartz and calcite crystals are up to 3mm big, and often fills the whole picture when observing them in the microscope. Calcite infiltrates in cracks and holes in between the quartz crystals (fig. 24d). Smaller chlorite crystals (0,1 mm) can be seen within the both quartz and calcite crystals, which is a good indicator that the hydrothermal fluid was circulating through the mylonitic shear zone (fig. 24b). Quartz crystals in the sampled veins show only weak signs for dynamic recrystallization, which is a contrast to the quartz crystals observed inside the mylonitic shear zone, where the quartz shows grain boundary migration recrystallization.
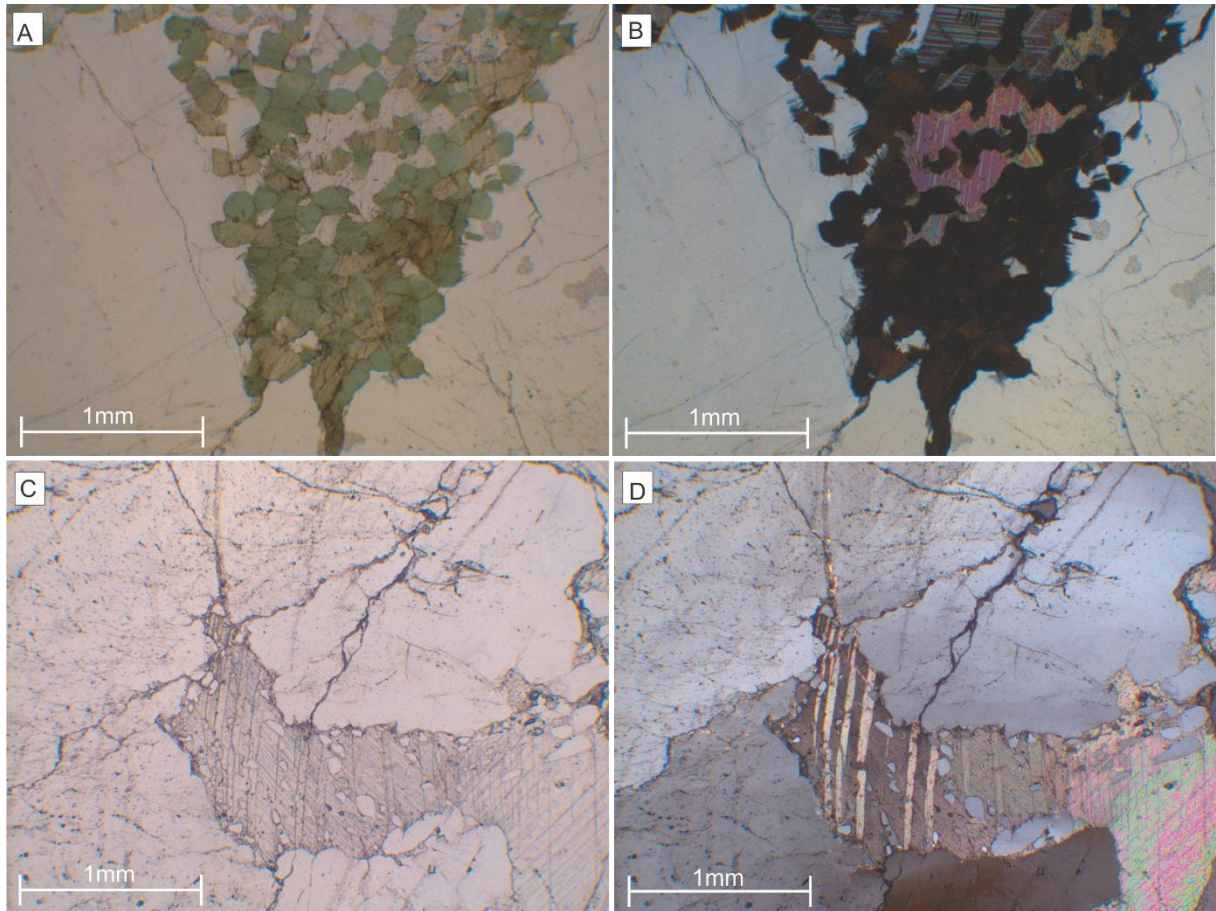
Figure 24. A) Hydrothermally precipitated chlorite in hydrothermal vein. B) Big quartz and calcite crystals overgrown by hydrothermally precipitated chlorite in hydrothermal vein. C) Calcite are precipitated where its available space. Calcite crystals overgrown by tiny crystals of quartz. D) Quartz crystals show only weak dislocation of the crystal lattice.

4.6.3 Reflected light

Along the contact with the hydrothermal veins, ilmenite grains can be observed in close relation to chlorite. Concentration of ilmenite seems to be heavily enriched along the hydrothermal vein in contrast to the mylonitic shear zone (fig. 25a), where the ilmenite grains seems to be more spread out. The reason the higher concentration of ilmenite along the hydrothermal vein might be due to direct contact metamorphism by the hydrothermal fluid and the precipitation of the quartz and calcite veins.
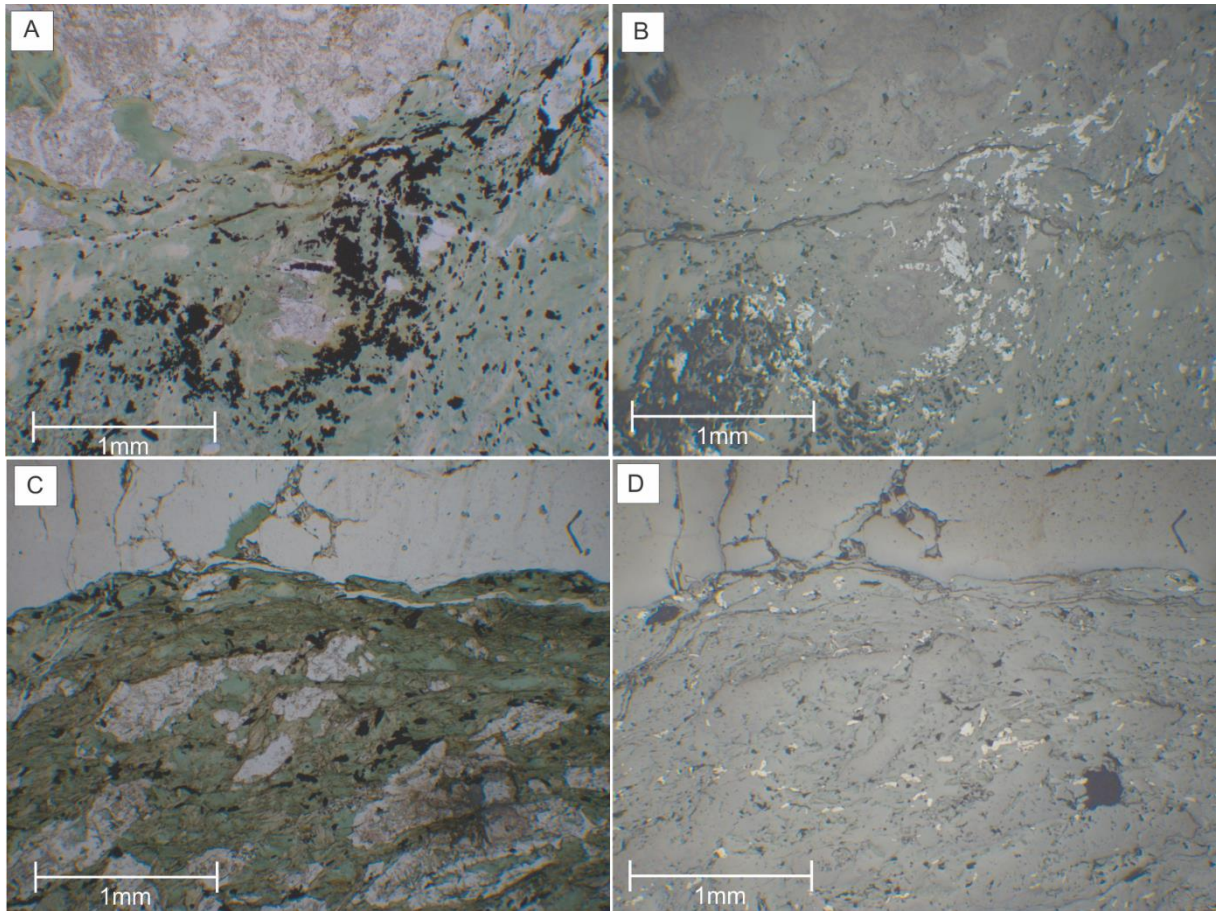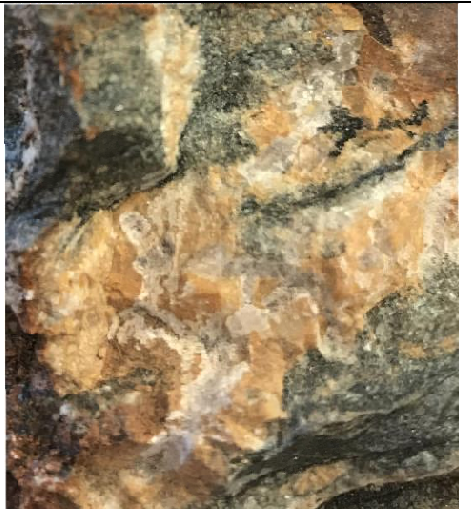
Figure 25. A) Ilmenite precipitated in large amount in contact with calcite in the hydrothermal vein. B) Ilmenite in reflected light. C) Ilmenite distributed in chlorite along the contact to quartz in the hydrothermal vein. D) Ilmenite in reflected light.

5 Samples

Table 1. Presentation of the sampled rocks.

Sample	Locality	Lithology	Mineralogy	Sample Type	Photo
TMF 001	Mylonitic shear zone (syn/post-D3)	Greenschist including carbonate vein	Chlorite, hornblende, carbonate, albite	Hydrothermal (?) carbonate vein in shear zone contact	
TMF 002	Mylonitic shear zone (syn/post-D3)	Greenschist including carbonate vein	Chlorite, hornblende, carbonate, albite	Hydrothermal (?) carbonate vein in shear zone contact	

TMF 003	Mylonitic shear zone (syn/post-D3)	Greenschist including carbonate vein	Chlorite, hornblende, carbonate, albite	Hydrothermal (?) carbonate vein in shear zone contact	
TMF 004	Folded Amphibolite	Weathered amphibolite including quartz-feldspar vein	Hornblende, Quartz, Microcline, Biotite	Pegmatite Quartz-Feldspar vein	

TMF 006	Mylonitic shear zone (syn/post-D3)	Quartz-Calcite vein	Quartz, Calcite	Hydrothermal vein	
TMF 015 (Ts, Ps)	Mylonitic shear zone (syn-post S3)	Greenschist	Chlorite, biotite, quartz, feldspar(?), tourmaline, carbonate	Shear zone, greenschist	

TMF 016	Hydrothermal quartz-calcite vein with greenschist (syn/post-D3)	Greenschist + hydrothermal vein	Chlorite, Albite, Quartz, Carbonate, Apatite	Greenschist in contact with hydrothermal vein	
TMF 017	Amphibolite containing coarse-grained quartz and fine-grained feldspar	Amphibolite + magmatic vein	Hornblende, Biotite, Feldspar, Quartz	Banded amphibolite	

| TMF 018 | Amphibolite | Banded amphibolite | Hornblende, Biotite, Quartz, | Banded amphibolite | |
| TMF 021 | Magmatic Quartz-Feldspatic vein in contact with amphibolite | Amphibolite + magmatic vein | Hornblende, Biotite, Quartz, Calcite, Feldspar, Hematite | Magmatic vein in contact with host rock | |

TMF 022 (RG1)	Rust-Weathered Garnet-Mica Schist	Rust-Weathered Garnet-Mica Schist	Hornblende, Albite, Quartz, small Garnets	Rust-Weathered Garnet-Mica Schist (in close contact with The Banded Amphibolite).	
TMF 023 (RG2)	Rust-Weathered Garnet-Mica Schist (Banded), containing large Garnet	Rust-Weathered Garnet-Mica Schist	Hornblende, Quartz, Hematite, Ankerite, 2 generations of Garnet	Rust-Weathered Garnet-Mica Schist	

6 Mineral chemistry and fluid inclusions

6.1 EBSD (Alteration of chloritized shear zone)
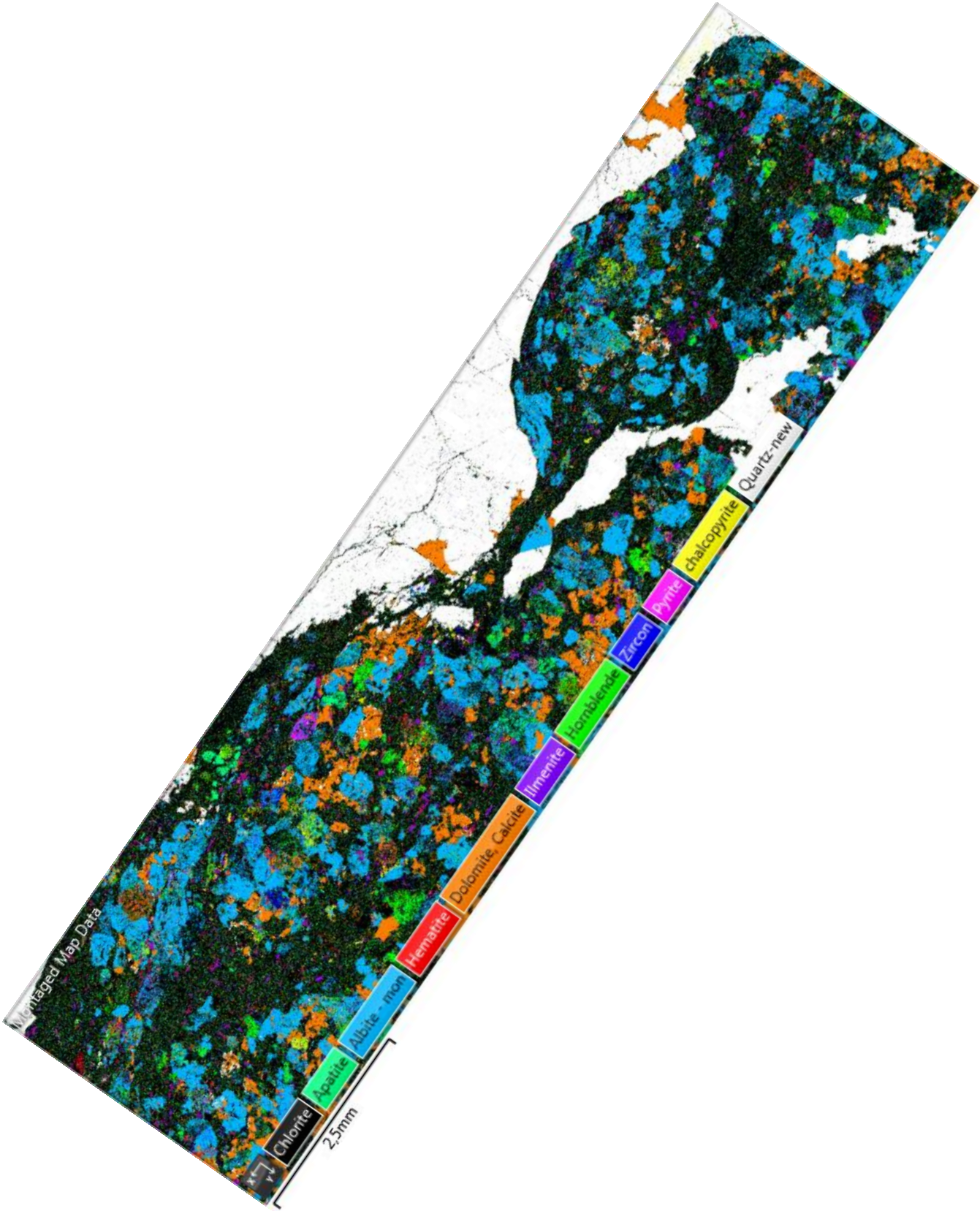
The EBSD mapped contact between the hydrothermal quartz and calcite vein and the mylonitic syn/post-S3 shear zone can be observed in figure 26. Quartz occurs mostly restricted to the hydrothermal vein and appears as relatively robust interlocking crystals. Chlorite defines the penetrative foliation in the phyllonite extending through the rock as continuous bands. Feldspar occurs as clustered bigger aggregates in between the layers of chlorite. Carbonates are widespread within the mylonitic shear zone in relation to feldspar, and can sometimes be observed as growing on top/or inside feldspar grains. Apatite is present as an accessory mineral and observed close to the contact between the hydrothermal veins and the mylonitic shear zone. Grains of ilmenite are restricted to chlorite. Ilmenite and hematite seems to coexist and/or occur together within the chlorite in the phyllonite, and ilmenite seems to account for the highest percentage (fig 26). Chalcopyrite also appears as smaller crystals distributed within chlorite, and it is often closely related to both ilmenite and hematite. Also coexisting grains of pyrite and chalcopyrite are common.

The transformation of the banded amphibole into phyllonite involved transformation from mineral assemblage's hornblende, biotite, titanite and quartz in the banded amphibolite into chlorite, albite, quartz and calcite in the phyllonite. This type of alteration is known as propylitic alteration. This alteration style is the most widespread form of alteration, and indistinguishable from regional greenschist metamorphism. The style of alteration tends to be isochemical and forms in response to H+ metasomatism. It comprises mainly chlorite, epidote, with lesser clinozoisite, calcite and albite. (Robb, 2004). The formation of chlorite from the breakdown of hornblende and biotite needs to be accompanied by water and involves cation metasomatism with the banded amphibolite. Calcite is widespread within the phyllonite, has its origin from the CO_2-H_2O hydrothermal fluids circulating through the phyllonite. The Ca^{2+} cations could come from the breakdown of hornblende or plagioclase.

6.2 XRD
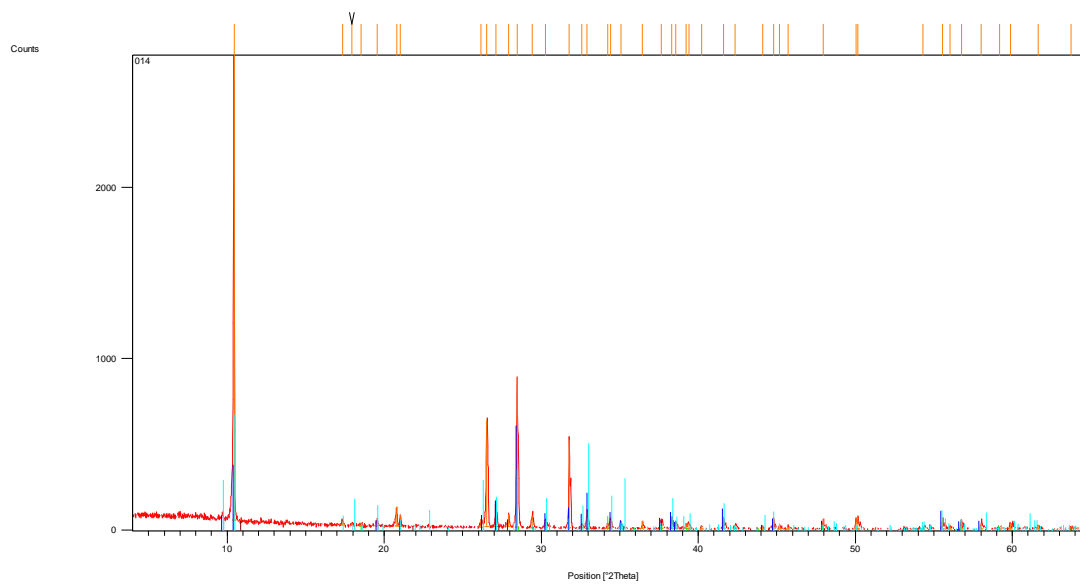
Figure 27. XRD pattern obtained from sample TMF 014, weathered amphibolite surrounding quartz-feldspatic veins.
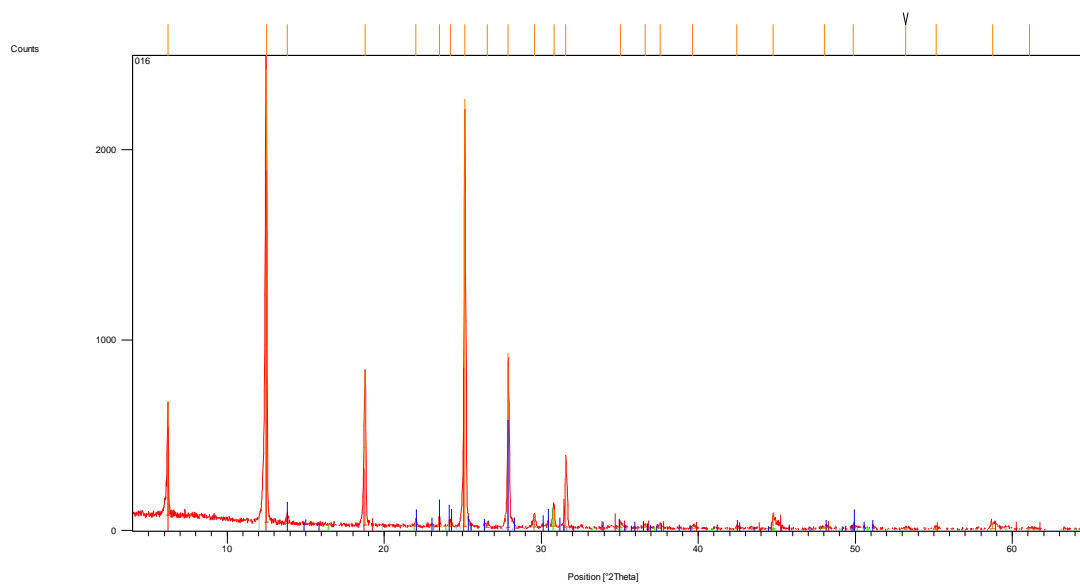
Figure 28. XRD pattern from sample TMF 016, chloritized mylonitic shear zone.
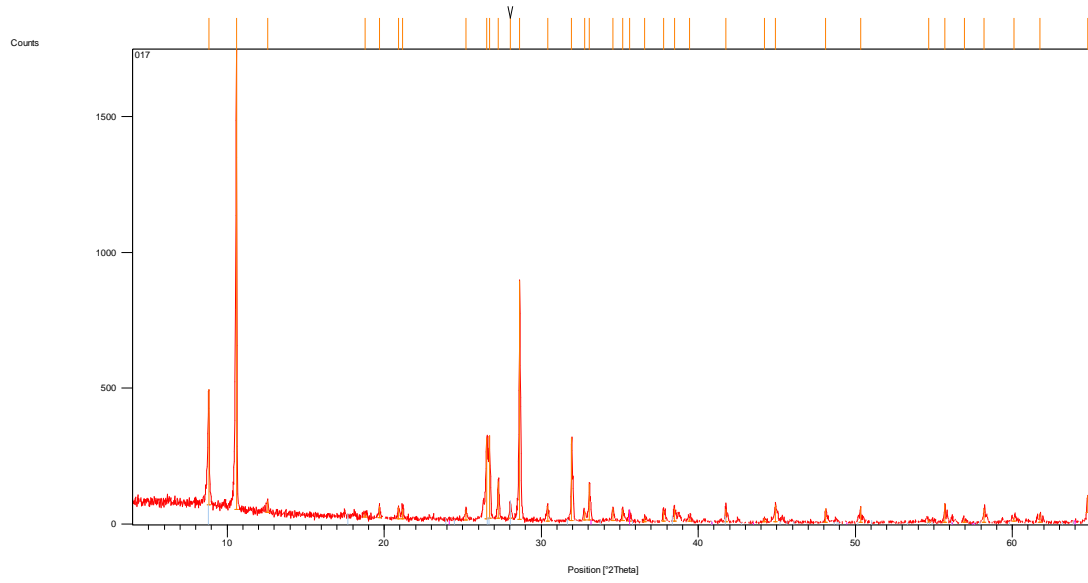
Figure 29. XRD pattern obtained from sample TMF 017, unweathered amphibolite.
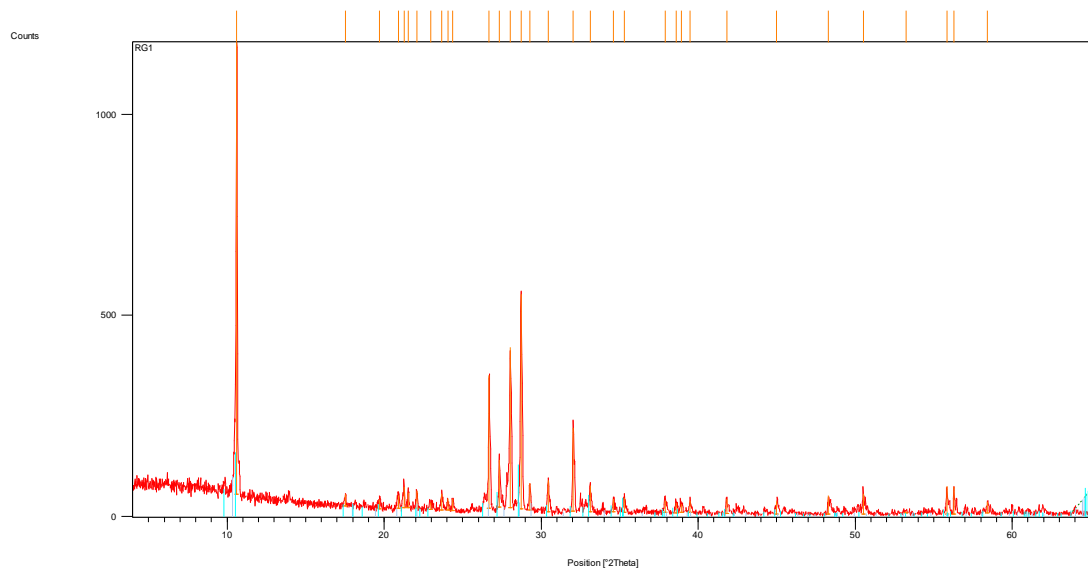
Figure 30. XRD pattern obtained from sample TMF 022, garnet-mica-schist (RG1).
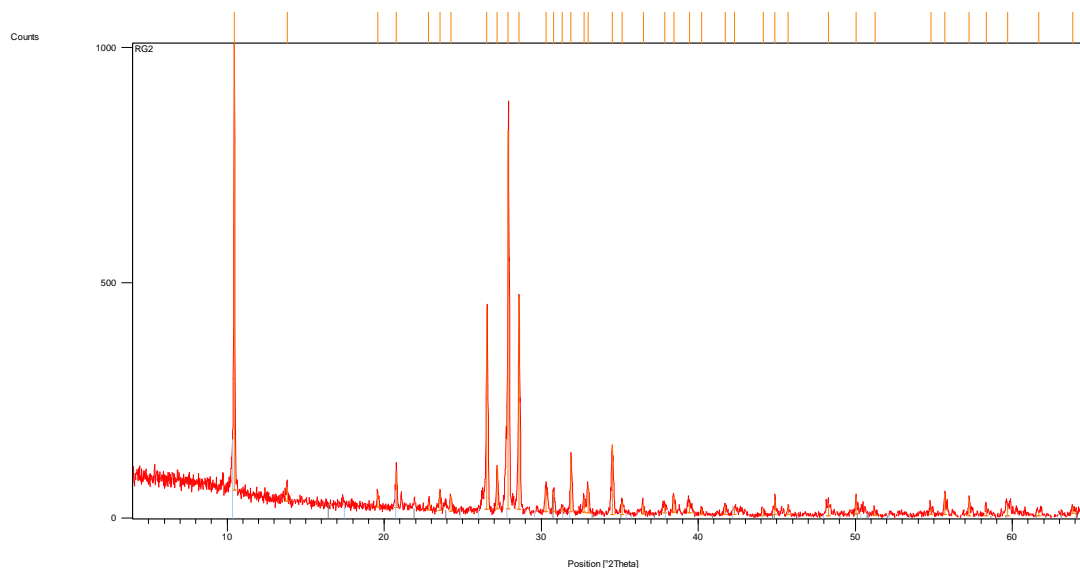
Figure 31. XRD pattern obtained for sample TMF 023, garnet-mica-schist (RG2).

The XRD analysis shows that the banded amphibolites hosting the magmatic quartz-feldspar veins (Sample TMF 014), do not show any hydrothermal alterations indicating no hydrothermal circulation through this lithology. XRD analyses for the weathered host rock, surrounding the magmatic veins contains quartz, hornblende garnet, actinolite (amphibole) and covelite (CuS). The unaltered banded amphibolite consist of biotite, quartz, chlorite and hematite. The biggest differences between the amphibolites hosting the magmatic veins (TMF 014) and the unaltered banded amphibolites (TMF 017) are that the altered amphibolites (TMF 014) contain garnet, and the fact that the altered amphibolites (TMF 014) lack biotite.

XRD analysis of the phyllonite/chloritized schist (TMF 016), which hosts the hydrothermal quartz and calcite veins, shows that the rock mainly consists of chlorite, albite, carbonate and ankerite (Fe-carbonate). The original rock minerals existing in the banded amphibolite (TMF 017), hornblende, biotite, quartz and feldspar transforms into chlorite, albite and carbonate in the mylonitic shear zone/chloritized schist (TMF 016).

The two garnet-mica-schists sampled, also shows some differences. Sample RG1 shows a rock composition consisting of riebeckite (Na-rich) hornblende, cummingtonite, albite and quartz. In contrast to the banded amphibolite (TMF 017), sample RG1 contains minerals rich in sodium. Sample RG2 consists of hornblende, quartz, albite and ankerite (Fe-carbonate). The XRD results reveals the presence of both carbonate and albite within the RG2, and might link the fluids from the circulating the phyllonite in relation to the garnet-mica-schist. Both calcite

and albite seen in the RG2 are also minerals observed in relation to the phyllonite/chloritized schist.

6.3 Chlorite geothermometry

Chlorite from the two different shear zones have roughly the same compositions. Mg-content varies between 8-10 wt%, Fe-content varies between 16-17 wt%, Al-content varies between 8-11 wt%, Si-content varies between 10-12 wt% and O-content varies between 35-46 wt%. This small variability suggests chemical equilibrium between the hydrothermal fluid and the chlorite have been attained. Calculated temperatures are listed in Table 2. Estimated values for sample TMF 016 (syn/post-D3) are quite precise and does not vary with more than 50ºC. Mean value for sample TMF 016 (syn/post-D3) is 521ºC. Temperature values estimated for sample TMF 002 and TMF 015 (syn/post-D3) varies with about 100ºC. Mean value for sample TMF 002 (syn/post-D3) is estimated to be 496ºC. The peak temperature for both samples is 541ºC, and also the small variability between the two samples gives the impression that the chlorite from the two different samples are produced under same conditions. The estimated temperatures for formation of chlorite fits very well with the observation of the grain boundary migration recrystallization.

Table 2. Temperatures calculated by Winccac for formation temperature (TºC) of chlorite.

Sample	TMF 016	TMF 016	TMF 016	TMF 016	TMF 016	TMF 016	TMF 002	TMF 002	TMF 002	TMF 002	TMF 015
Cathelineau (1988) TS	536	498	520	492	538	541	492	541	533	539	506
Kranidiotis and MacLean, (1987)	445	422	433	416	445	451	416	445	439	445	423
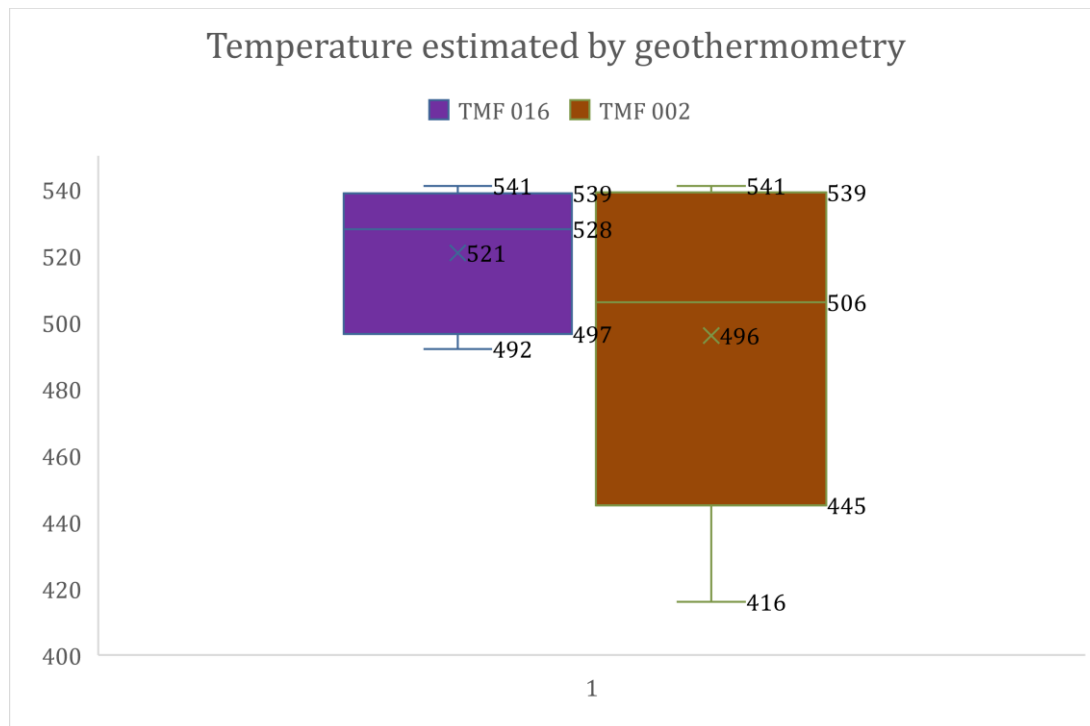
Figure 32. Estimated temperatures in (T in ºC) for formation of chlorite by the program Winccac, by using models by (Cathelineau, 1988) and (Kranidiotis and MacLean, 1987).

6.4 Fluid Inclusion Petrography

Quartz samples for fluid inclusion studies were taken the hydrothermal quartz vein localized in the post S3 shear zone (see map). The hydrothermal quartz vein display a wide variety of fluid inclusions of different sizes and shapes. They hydrothermal quartz shows no signs for micro cracks and annealing of cracks. The fluid inclusion of the hydrothermally precipitated quartz vein reveals two major inclusion types. Type 1 fluid inclusions are big CO_2-rich fluid inclusions up to about 50µm in longest dimension. The degree of fill varies, however 85% of liquid 1 (H_2O-NaCl), 10% of liquid 2(CO_2) and 5% gas (CO_2) are the most common degree of fill. These fluid inclusions occur as single big inclusions, or in group of two and three. Their show ellipsoidal to irregular shapes. Negative crystal forms have not been observed. Necking-down are widespread within the sample. This also explains the various degree of fill in the inclusions. There are also some of Type 1 fluid inclusions containing a bigger amount of liquid CO_2. These fluid inclusions where not suitable for calculations of isochrones, because these fluid inclusions decrepitated before they reached the homogenization temperature. These fluid inclusions have probably been trapped at higher temperatures early in the crystallization sequence. Type 2 inclusions are relatively small (~50 µm) three-phase CO_2-rich inclusions. These inclusions appears in trails that stretches out in different directions, and sometimes crosscuts each other.

The majority of micro thermometry measurements were done on the bigger inclusions, since they are so common and easiest to see relative changes in them. The degree of fill in Type 2 inclusions are also various, the same case as in Type 1. The fluid inclusions measured for in the relation to the hydrothermal quartz and calcite veins are believed to be primary in origin, due to their big size and that almost all inclusions consist of the same three phases.
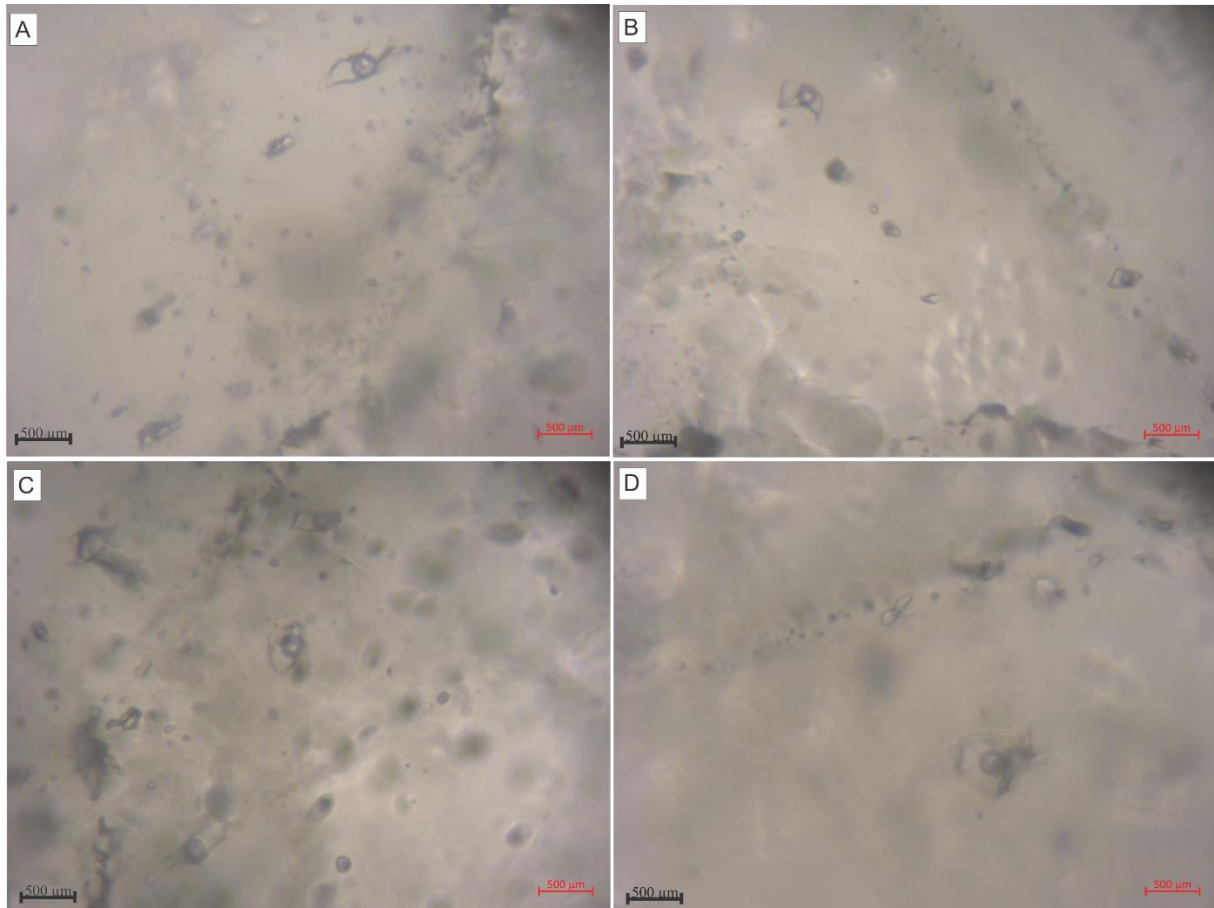
Figure 33. A) CO2 fluid inclusions in hydrothermal quartz vein consisting of various size. B) fluid inclusions in various size following a straight path. C) various shapes. D) big contrast in sizes.

6.5 Microthermometry

Type 1 fluid inclusions homogenization temperature for CO2 (T_H^{CO2}) ranges from 21,9ºC to 29,5ºC (L1 + L2 + V → L + V) Total homogenization temperature (T_H) range from approximately 250ºC to 323ºC (L + V → L). The temperature of first ice melting (T_{FM}) occurs at -17ºC, which indicated that NaCl is the dominant salt present in solution. Clathrate meting temperature (T_M^{clact}) ranges from 5,8ºC to 9,7ºC indicating the salinity from 0 to 13, 2 eq. wt% NaCl clathrate dissolution curve (CDC) after (Collins, 1979).

6.6 Raman Spectrometry

The goal of Raman spectrometry was to identify volatiles the three-phase inclusions and calculate the density of the CO_2-inclusions. Common fluid species have specific Raman shifts (Δv in cm^{-1}), and different fluids can be identified with certain specific Δv values (see table after (Burke, 2001). Figures 21 and 22 shows two spectra of CO_2-fluid inclusions with different densities. The distance between the two peaks (Δv in cm^{-1}) is proportional to fluid density (Burke, 2001). Both peaks for CO_2 and N_2 were observed inn all tested inclusions. By measuring the high of the CO_2 and N_2 peaks, it is possible to calculate the ratio of the two gasses by dividing the estimated areas on each other. Table 1, shows that the CO_2 and N_2 ratio varies from inclusion to inclusion, which also can be observed within the microscope. However, the amount of CO_2 is always high compared to N_2 in all measured inclusions, and can be seen by the much smaller peak for N_2 than for CO_2.
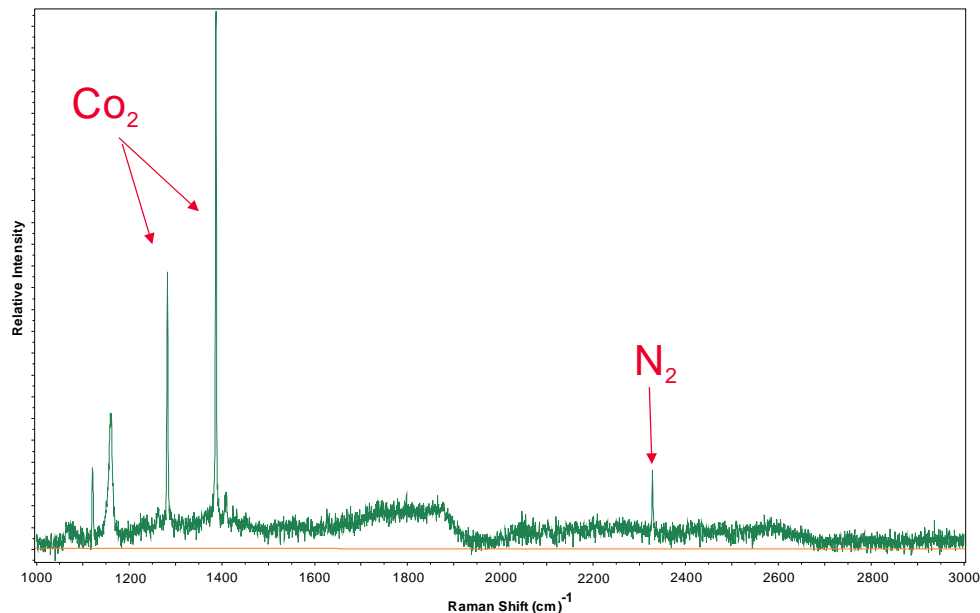
Figure 34. Raman spectrometry from fluid inclusion 5, shows two distinct peaks for CO_2 and one smaller for N_2.
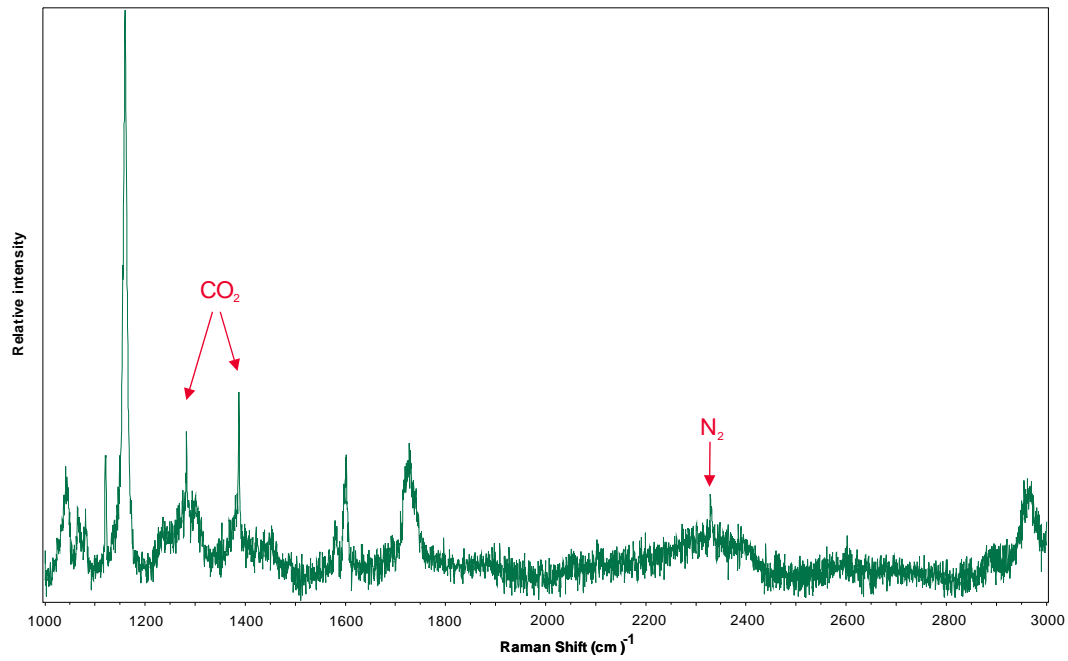
Figure 35. Raman spectrometry from fluid inclusion 1, shows also two peak for CO2 and one smaller for N2.

Table 4. Estimated percentages of CO_2 vs. N_2.

	x^{CO2}	x^{N2}	Δ	r^{CO2}(g/cm3)
FI1	80	20	103,75	0,46
FI3	96	4	104,84	0,91
FI4	85	15	104,70	0,86
FI5	90	10	103,80	0,48

6.7 Stable Isotope

Table 5. d13C and d18O values obtained from selected carbonate-bearing samples.

	Sample name	Peak area [Vs]	d13C VPDB [‰]	d18O VPDB [‰]	d18O VSMOW [‰]
Quartz-feldspatic veins	TMF 004	73,13	-12,3	-18,3	12,0
Quartz-feldspatic veins	TMF 004	26,44	-12,4	-18,3	12,1
Quartz-feldspatic veins	TMF 004	120,52	-12,3	-18,3	12,1
Quartz-feldspatic veins	TMF 021	38,82	-6,4	-15,3	15,2
Quartz-feldspatic veins	TMF 021	70,19	-6,3	-15,4	15,0
syn/post S3	TMF 002	124,31	-3,4	-17,8	12,6
syn/post S3	TMF 001	70,49	-3,5	-17,6	12,8
syn/post S3	TMF 003	82,84	-3,5	-17,7	12,7
syn/post S3	TMF 003	83,36	-3,4	-17,7	12,7
syn/post S3	TMF 002	22,58	-3,5	-17,6	12,8
syn/post S3	TMF 001	75,24	-3,7	-17,7	12,7
syn/post S3 (Hydrothermal quartz)	TMF 016	30,41	-3,0	-17,8	12,6
syn/post S3 (Hydrothermal quartz)	TMF 016	99,52	-3,1	-17,9	12,5
syn/post S3 (Hydrothermal quartz)	TMF 016	21,75	-3,0	-17,8	12,5
syn/post S3 (Hydrothermal quartz)	TMF 006	124,35	-3,5	-17,7	12,7
syn/post S3 (Hydrothermal quartz)	TMF 008	45,77	-3,6	-17,9	12,5
syn/post S3 (Hydrothermal quartz)	TMF 008	125,92	-3,9	-17,9	12,5
syn/post S3 (Hydrothermal quartz)	TMF 006	83,89	-3,7	-17,5	12,9
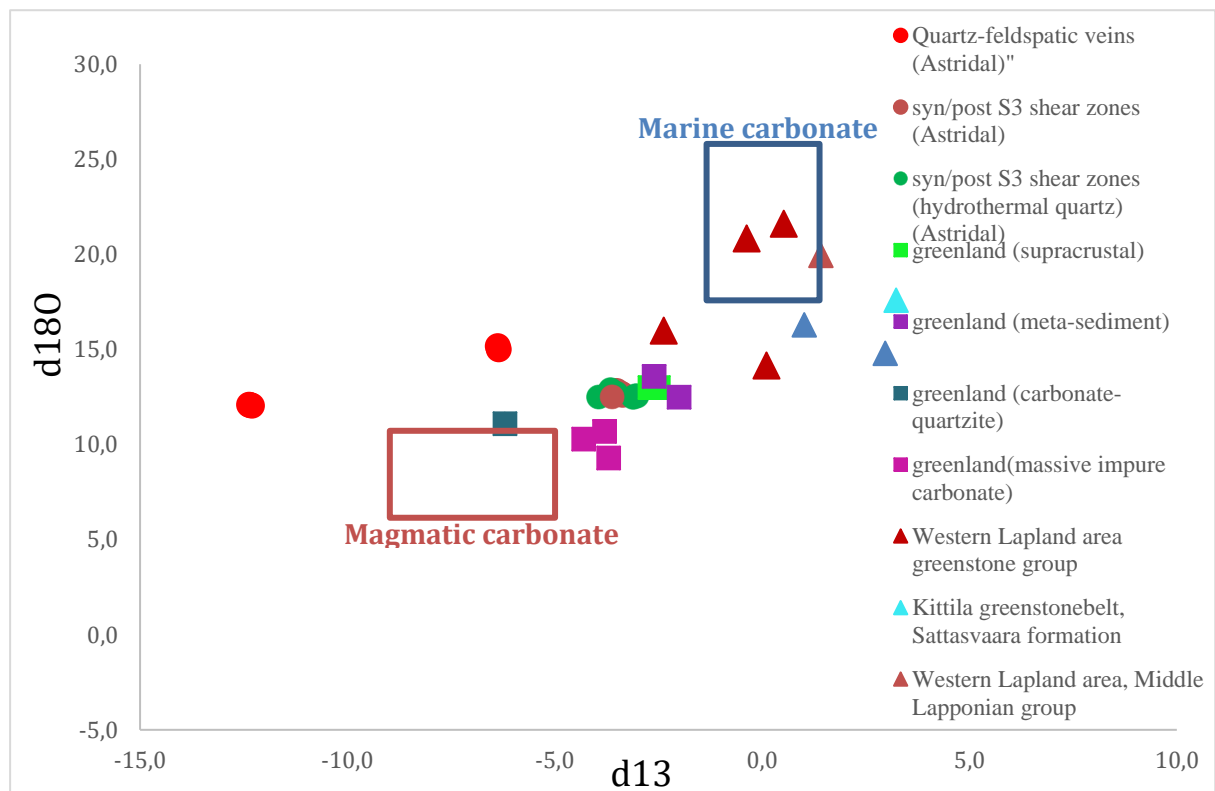
Figure 36. Stable isotope diagram showing d18O vs d13C values.

None of the measured isotopic ratios plots within either marine carbonates or magmatic carbonate (see fig 23). The quartz-feldspatic veins, are characterized by isotopically light carbon comparing to later hydrothermal quartz-carbonate veins (syn/post S3). Samples from syn/post S3 veins reflect a mixing trend between magmatic CO_2 and marine carbonates, but plots in close relation to d18O and d13C values from other supracrustal belts (fig 36).

7 Discussion

7.1 Structural relationships

On a regional scale (Fig. 3) the NW-SE trending Astridal supracrustal belt lies parallel to lens- shaped, anastomosing shear zones that are internally and subparallel to lithologic boundaries. The entire supracrustal belt, however, in its northern part makes a major left-bend into the fjord (Fig. 3) due to presence of a mega-scale, S-shaped F3 fold, and the hinge of this fold is located near the study area (Bergh et al., 2010). The mapped syn/post-D3 shear, NE-SW-striking shear zone is arranged oblique to the average axial surface of this sinistral F3-fold (Fig. 3). If the shear zone formed syn-tectonic relative to this F3 fold, the axial surface may be fan-shaped and split into several directions, near the macro-scale hinge zone (see further discussion below). This is supported by fan-shaped, variable orientations of similar axial surfaces to smaller F3-fold in Småsandneset (fig 6). The reason for the fan-shaped orientation of axial surfaces of F3 folds, and partly, very complex disharmonic fold styles in the study area of the major fold hinge, could be due to space problems caused by the major steep north plunging sinistral folding of the Astridal supracrustal belt.

Complex strain patterns are often seen in hinges of large scale folds, due to accommodation problems. Space problems like this may explain, for example, the variable orientations of ductile shear zones in the study area of the major F3 fold hinge (Bergh et al., 2010, Bergh et al., 2015). The enrichment of hydrothermal fluids along shear zones could be due to various factors along the fault tips including lithology, dip of bedding/foliation and the local strain field. Formation and subsequent reactivation of shear zones arranged parallel to the axial plane of small-scale F3-folds may have caused opening, and fluids under high pressure (CO_2) in the crust are free to move upwards and then, triggered chloritization of these shear zones. This is supported by, among others, the presence of pegmatite dikes in similar F3 folds elsewhere in the Astridalen crustal belt (Bergh et al., 2015). These pegmatitic dikes are thought to have formed in a similar way and hence, the hydrothermal veins and chloritization in shear zones at Småsandnesset could be of the same age as the dated pegmatites (Bergh et al., 2015)

The major F3-fold is truncated by a steep NW-SE strike-slip shear zone on the fjord bottom in Baltsfjord (Bergh et al., 2010)and this ductile shear zone (>10 m wide) is exposed at the contact with the surrounding TTG gneisses. An alternative explanation for hydrothermal

fluids along the studied quartz-carbonate hosting, NE-SW striking mylonitic shear zone within the Astridal supracrustal belt could potentially be related complex strain pattern at the eastern tip to a ductile splay fault merging into the major NW-SE striking shear zone, arranged parallel to the Astridal metasupracrustal belt. Several NE-SW-striking mylonitic shear zone/bands are mapped in the southeastern part of Småsandnesset. Sigmoidal clasts found inside the NE-SW oriented syn/post-D3 shear zone indicate sinistral sense of shear movement at this locality, which is confirmed by thin section studies (fig 21). Several shear zones/bands with NE-SW orientation occur on the southwestern side of the islet, on the northeastern side there are only one shear zone oriented in the NE-SW direction, but two sets of hydrothermal veins exists with the same orientation.

Complex strain are often seen at shear zones tips and zones of extension could occur coeval or in response to a different stress pattern e.g.(Kim et al., 2004). Additional complexity are represented by the NW-SE trending major shear zone indicated onshore (Bergh et al., 2010, Bergh et al., 2015) stretching all the way to Småsandnesset and will likely affect the stress/strain pattern in this area. Damage zones at fault tips may have a complex pattern, especially where several shear zones meet. The rock around a shear zone tip will experience the highest stress and more intense damage can be expected compared to subsequent slip on a fault plane (Martel, 1997). Where there is rapid decrease in slip at a shear zone tip, extensional wing cracks may occur (Rispoli, 1981). The orientation of the chloritized shear zone within Småsandnesset, are oriented exactly perpendicular to the main sinistral shearing orientation of the major strike slip faults in Astridalen supracrustal belt. Bergh et al. (2015) describes S3 shear zones at Småsandnesset to consist of both dextral and sinistral semi-ductile shear zones. Other factors that might influence and trigger this reactivation of faults includes lithology, fluid pressure and temperature. Reactivation of these already existing semi-ductile shear zones arranged parallel to the axial plane of minor F3-folds caused opening, and fluids under high pressure (CO_2) in the crust where free to move upwards and triggered chloritization of these shear zones.

7.2 Origin of Ti-bearing mineral phases

Since amphibolite can be of both sedimentary (para-) and igneous (ortho-) origin, detailed geochemical and mineral chemical data are needed to verify the origin. Distribution of Ti in ortho- and para-amphibolite have been emphasized by (Wilcox and Poldervaart, 1958). Showing that Ti-content is at a minimum in the para-amphiboltes. Iron-enrichment ratio is also a method used to show differential trends in basaltic rocks Ti-contents have shown to increase

with progressive iron-enrichment (Osborn, 1962). The variations of Ti in magmatic rocks and their metamorphic relatives shows systematic changes, and such relation is absent in rocks of para-amphibolite (Misra, 1971). The mineralogy of the banded amphibole in Småsandnesset is relatively simple, consisting of hornblende, biotite, quartz, titanite and garnet. The most pronounced texture is the metamorphic overprint of the preferred elongation of the hornblende, biotite, chlorite and quartz (see fig.) in a specific direction and defines what can be seen as the main foliation (S1) in the banded amphibolite in field. Small titanite grains can be observed growing in relation to biotite in the banded amphibolite.

Oxidation of iron can be seen in relation to the garnet mica schist in Småsandnesset, and in relation to this transformation microscopic studies have revealed that the biotite are missing from the garnet-mica-schist and instead the rock comprising of opaque mixtures of iron oxides which are impossible to distinguish from another. Banfield and Eggleton (1988) described that the early stages of biotite weathering, limited dissolution appears to have opened some channels within the biotite grains, which allowed increased access to the weathering agents (Banfield and Eggleton, 1988). What Banfield and Eggleton (1988) described as the beginning of the kaolinite-goethite stage appears to be marked by rapid oxidation of iron, an extremely abundant component in the system, comprising about half the octahedral cation population of biotite, and that iron migrated to form poorly crystalline Fe-hydroxide and this material subsequently recrystallized to goethite (Banfield and Eggleton, 1988). This type of biotite weathering can be observed within the garnet-mica-schist as gray to black mixtures of iron oxides occupying large vugs or pits within the rusty garnet-mica schist. XRD analysis do however not report any kaolinite within the garnet-mica-schist. An increased amount of garnet in contrast to the banded amphibolite can also be seen in the garnet-mica-schist. Ferry and Spear (1978) documented that cation exchange reaction between biotite and garnet can be achieved (Ferry and Spear, 1978). Therefore, the higher amount of garnet within the garnet-mica-schist can be explained by cation exchange reactions between biotite and garnet, to produce higher amount of garnet by the lack of biotite in the garnet-mica-schist.

7.3 Ilmenite in the chloritized shear zone and in relation to hydrothermal quartz veins

The titantite crystals in the banded amphibolite are previously described to be related to biotite. Biotite is missing in the phyllonite along the contact between the hydrothermal veins, and could

potentially be the source for ilmenite. Several authors have stated that biotite in igneous rocks contains more Ti4+ than biotite in metamorphic rocks (Rimšaite, 1964) and the distribution of Ti4+ may change as a function of metamorphic grade (Guidotti et al., 1977). In terrestrial silicates, titanium is invariably found in the +4-valence state, occupying octahedral sites where it substitutes for Al, Mg and Fe (Van Baalen, 1993).

The banded amphibolites have been rich in iron, and this is supported by observations in the field, microscopic studies and the chemical composition of the rock. In contrast to the amphibolite, the phyllonite contains higher concentration of ilmenite and ilmenite and other iron oxides are the only heavy metal bearing minerals distributed within the phyllonitic shear zone. The ilmenite and iron oxides are mainly distributed in the phyllonitic shear zone in close relation to chlorite. The formation of ilmenite in the mylonitic shear zone occurred under approximately $500^{o}C$ based on geothermometry based on formation of chlorite in the shear zones. Formation temperature for both the syn/post-S3 shear zones, shows roughly the same temperature for formation. Combing the isochores with the temperature calculated for the formation of chlorite, Ilmenite is believed to be a direct contact metamorphic reaction of breakdown of Ti-rich biotite into ilmenite. The solubility of TiO_2 is pH dependent. At pH below 2,5 the dominant Ti-species in solution is a hydroxyl complex TiO^{2+} or $Ti(OH)^{2+}_2$. The nature of the dominant Ti-species in solutions with pH higher than 2,5, is still under question. However, in much of the literature its assumed that a neutral hydroxyl complex like $Ti(OH)^0_4$ or $TiO(OH)^0_2$ is the dominant Ti-species (Van Baalen, 1993). Estimated salinity for the fluids that caused the hydrothermal alteration lies in between 6-7 wt% NaCl. The fluids pH where near neutral due to presence of carbonate and lack of kaolinite in the alteration zone in contact with the hydrothermal vein. Therefore, ilmenite could potentially not be transported with the fluid and therefore must the source of titanium must lie within the banded amphibolite itself.

7.4 Formation of hydrothermal quartz-carbonate veins

The quartz-calcite veins hosted in the mylonitic ductile shear zone are formed under retrograde conditions by hydrothermal fluids circulating during formation of these mylonitic shear zones. The mineralogy of the syn/post S3 shear zone, reflects what type of fluids where circulating these rock. They were moderate saline, consisting of about 6-7 wt% NaCl, have high concentrations of CO2, and they homogenize at temperatures around $290-320^{o}C$ depending of the amount of CO2 in the fluid inclusions. Similar inclusions have been identified in many orogenic gold deposits (e.g., (Robert et al., 1995) (Eilu et al., 2003, Pitcairn et al., 2006)

While these fluids circulated the rock they precipitated carbonate due to the high concentrations of CO2, albite as sodium was introduced by NaCl and quartz as leftover silica from the retrograde reaction. According to microscopic observations and XRD analyses, amphibolites along hydrothermal veins have been altered to a mixture of chlorites, quartz, carbonates and albite by the following reaction:

Ca-amphibole + Ca-plagioclase + H2O + CO2 + NaCl → Chlorite + Quartz + Carbonate + Albite
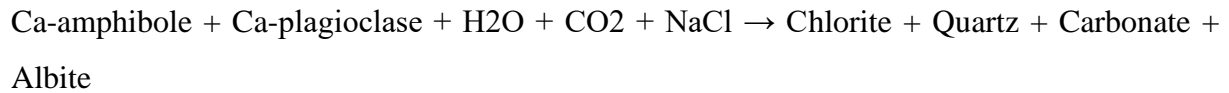
7.5 Temperature and pressure estimations

Both the syn/post D3 shear zones consists of the same mineralogy existing of mainly chlorite, albite and carbonates, with ilmenite in relation to chlorite. Quartz existing in the syn/post-D3 shear zone (TMF 015) shows grain boundary migration recrystallization, the highest temperature form for dynamic recrystallization in quartz. Temperature estimated for this type of recrystallization of quartz are believed to lay in the temperature range of 500-700°C (Stipp et al., 2002). Distribution of quartz grain in the syn/post-D3 shear zone are somewhat limited, but quartz grains appears as bigger elongated aggregates or sigma shaped clasts, with prominent grain boundary migration recrystallization. These quartz grains that appears in the syn/post-D3 shear zone, could potentially be deposited in cracks or cavities within the mylonitic shear zone during fluid flow, due to the limited prevalence of quartz within the syn/post-D3 shear zone. The geothermometers revealed formation temperature of approximately 500°C, and combining this temperature with the calculated isochore values the estimated pressures are about 600MPa (fig 37). These estimated values plots the conditions under which the chloritized syn/post shear zones in between greenschist facies and amphibolite facies conditions (fig 38).

Table 6. Calculated isochore values.

BLUE		GREEN		ORANGE		DARK BLUE		BROWN	
T°C	P(MPa)	T°C	P(MPa)	T°C	P(MPa)	T°C	P(MPa)	T°C	P(MPa)
290	163	297	158	306	12	272	110	306	103
390	374	397	354	406	151	372	331	406	281
490	574	497	545	506	282	472	531	506	449
590	765	597	731	606	408	572	720	606	610
690	950	697	912	706	528	672	902	706	766
790	1132	797	1089	806	646	772	1080	806	918
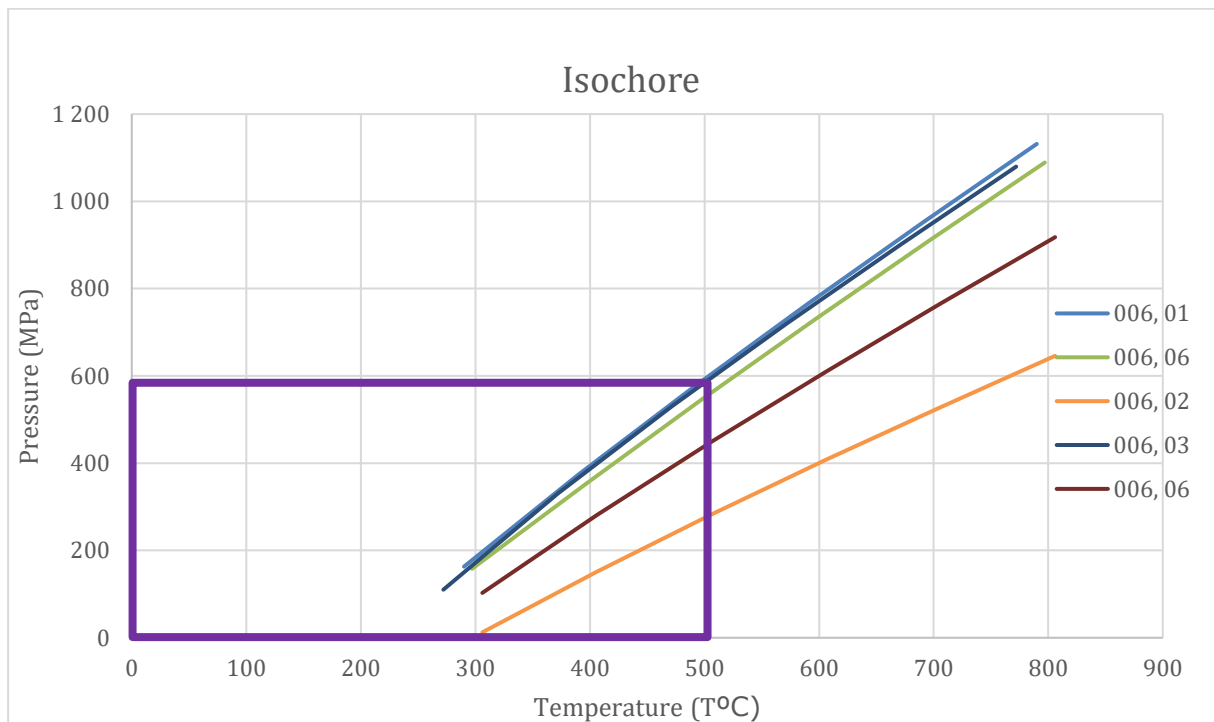
Figure 37. Graph for estimating the salinity of NaCl in CO2 rich inclusions, based on melting temperature of clathrates.
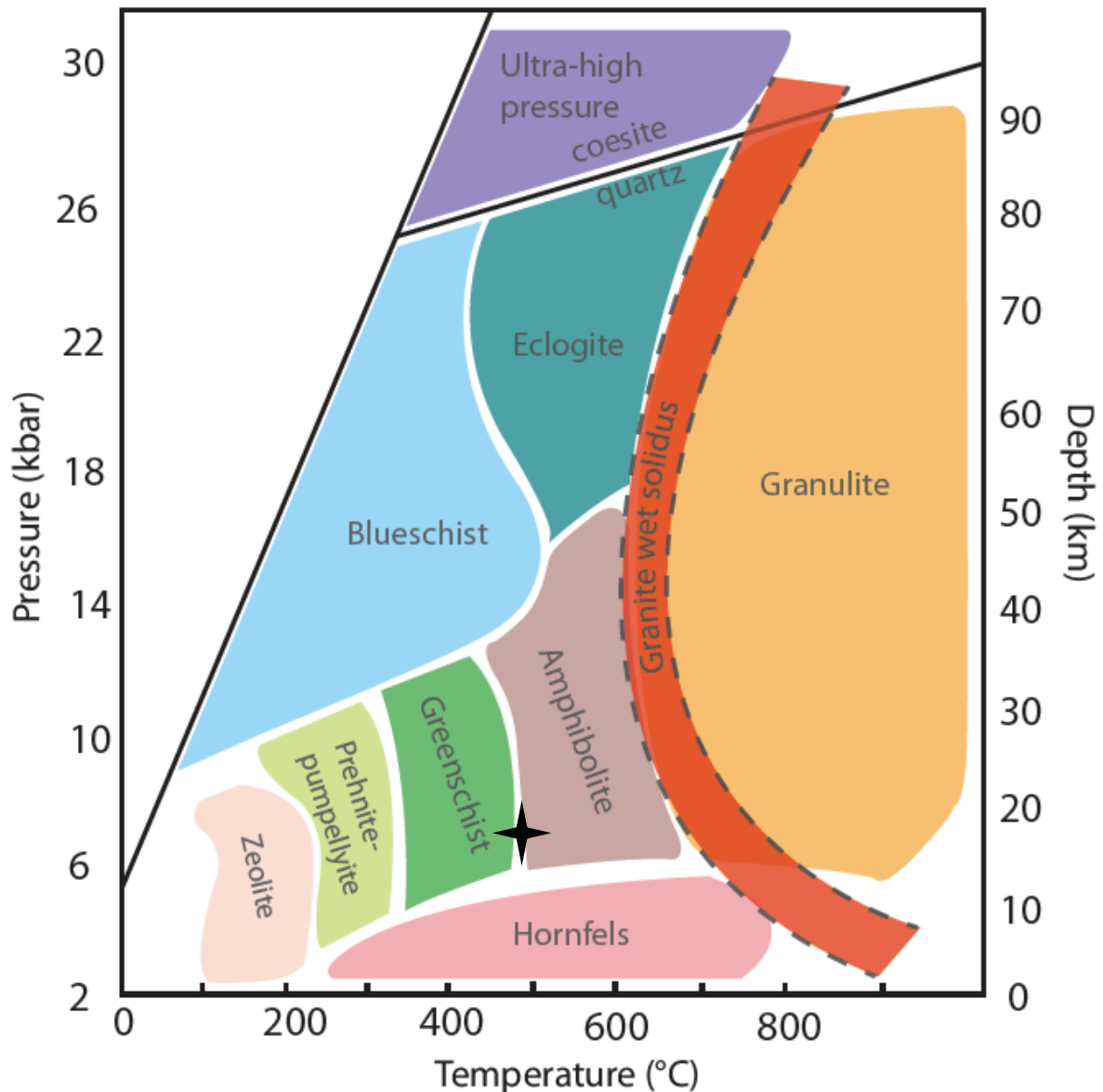
Figure 38. Formation conditions for formation of chlorite based on microthermometry and chlorite geothermometry in the post-D3 mylonitic shear zone. Metamorphic facies diagram (Faber, 2018). Redrawn and modified from Bentley (2010), Bousquet et al.(2008) and Yardley (1988).

7.6 The source of CO2

Since the hydrothermally precipitated quartz and calcite vein collected in field only shows weak dislocation of the crystal lattices in the quartz-grains, could indicate that the hydrothermal vein intruded in at a late stage of the development of the shear zone or was a result of a later event. Since the carbonate (and chlorite) can be observed in thin sections filling in cracks and available space in the hydrothermal veins, quartz and calcite should be precipitated at the same time. Since the chloritized schists in both the syn/post S3 shear zones contains carbonate, both of

shear zones must have been affected by hydrothermal fluids. Fluid inclusion studies revealed that hydrothermal fluids contain a significant amount of CO_2 that could be the most likely source for carbonate minerals within the shear zones. The stable isotope analyses of carbonates hosted by hydrothermal quartz-carbonate veins indicate that CO_2 originated from volcano sedimentary sequences (Fig. 36). The origin of supracrustal rocks are often related to rift basins. Subsequent volcanism could fill these basins with both mafic and felsic magmas, along with various clastic and volcanoclastic sediments. These geological settings have the possibility of infiltration of both magmatic carbonate and marine carbonate. They are also one of the most tectonically complex geological terrains, since they originally was rift basins, but today exposed on top of old Precambrian crust above sea level. Their complex evolution is the reason why these carbonate does not fit in either of these isotopically measured fields. The similar isotopic signature has been observed in Lapland/Kittila Greenstone belt (Karhu, 1996), as well as in Isua supracrustal belt in Greenland (Schidlowski et al., 1979).

8 Conclusion

- Enrichment of hydrothermal fluids and the occurrence of prominent quartz-carbonate veins in the NE-oriented syn/post D3 shear zone at Småsandnesset are likely linked to reactivation of shear zones arranged parallel to the axial plane of small-scale F3-folds. Complex stress and strain pattern at fault tips may have contributed to opening, and fluids under high pressure (CO_2) in the crust were free to move upwards and triggered chloritization of these shear zones.

- Presence of melt inclusions and absence of fluid inclusions in quartz hosted by quartz-feldspatic veins suggest their magmatic origin.

- Fluid inclusion data obtained from hydrothermal quartz-carbonate veins hosted by syn/post S3 ductile shear zones revealed that hydrothermal fluids were low to moderate saline (6-7 wt% NaCl), high temperature fluids (290-300°C) with enriched in CO_2 and N2. Similar inclusions have been identified in many orogenic gold deposits.

- Fluid inclusion data and chlorite geothermometry revealed that hydrothermal quartz-carbonate veins hosted by syn/post D3 ductile shear zones have been deposited at temperatures of 500°C and pressures of 600 MPa.

- The isotopic composition of carbonates from hydrothermal quartz-carbonate veins hosted by syn/post S3 ductile shear zones suggests influence of magmatic CO_2 and marine carbonates and overlaps with isotopic composition of carbonates from Lapland/Kittila Greenstone belt as well as in Isua supracrustal belt in Greenland.

9 Refrences

BANFIELD, J. F. & EGGLETON, R. A. 1988. Transmission electron microscope study of biotite weathering. *Clays and Clay Minerals,* 36**,** 47-60.

BERGH, S., CORFU, F., PRIYATKINA, N., KULLERUD, K. & MYHRE, P. 2015. Multiple post-Svecofennian 1750–1560 Ma pegmatite dykes in Archaean-Palaeoproterozoic rocks of the West Troms basement complex, north Norway: Geological significance and regional implications. *Precambrian Research,* 266**,** 425-439.

BERGH, S. G., KULLERUD, K., ARMITAGE, P. E., BOUKE ZWAAN, K., CORFU, F., RAVNA, E. J. & INGE MYHRE, P. 2010. Neoarchaean to Svecofennian tectono-magmatic evolution of the West Troms Basement Complex, North Norway. *Norwegian Journal of Geology/Norsk Geologisk Forening,* 90.

BERGH, S. G., KULLERUD, K., CORFU, F., ARMITAGE, P. E., DAVIDSEN, B., JOHANSEN, H. W., PETTERSEN, T. & KNUDSEN, S. 2007. Low-grade sedimentary rocks on Vanna, North Norway: a new occurrence of a Palaeoproterozoic (2.4-2.2 Ga) cover succession in northern Fennoscandia. *Norwegian Journal of Geology/Norsk Geologisk Forening,* 87.

BERGH, S. G., KULLERUD, K., MYHRE, P. I., CORFU, F., ARMITAGE, P., ZWAAN, K. & RAVNA, E. 2014. Archaean elements of the basement outliers west of the Scandinavian Caledonides in Northern Norway: architecture, evolution and possible correlation with Fennoscandia. *Evolution of Archean Crust and Early Life.* Springer.

BURKE, E. A. 2001. Raman microspectrometry of fluid inclusions. *Lithos,* 55**,** 139-158.

CARTER, J. & BARWICK, V. 2011. Good practice guide for isotope ratio mass spectrometry. *FIRMS Network*.

CATHELINEAU, M. 1988. Cation site occupancy in chlorites and illites as function of temperature. *Clay minerals,* 23**,** 471-85.

COLLINS, P. L. 1979. Gas hydrates in CO 2-bearing fluid inclusions and the use of freezing data for estimation of salinity. *Economic geology,* 74**,** 1435-1444.

CORFU, F. 2004. U–Pb age, setting and tectonic significance of the anorthosite–mangerite–charnockite–granite suite, Lofoten–Vesterålen, Norway. *Journal of Petrology,* 45**,** 1799-1819.

CORFU, F., ARMITAGE, P. E., KULLERUD, K. & BERGH, S. G. 2003. Preliminary U-Pb geochronology in the West Troms Basement Complex, North Norway: Archaean and Palaeoproterozoic events and younger overprints. *NORGES GEOLOGISKE UNDERSOKELSE,* 441**,** 61-72.

EILU, P., SORJONEN-WARD, P., NURMI, P. & NIIRANEN, T. 2003. A review of gold mineralization styles in Finland. *Economic geology,* 98**,** 1329-1353.

FABER, C. 2018. Mountain building processes in the northern Norwegian Caledonides-Examining Caledonian continental collision using a combination of structural mapping, phase equilibrium modelling and geochronology.

FERRY, J. T. & SPEAR, F. 1978. Experimental calibration of the partitioning of Fe and Mg between biotite and garnet. *Contributions to mineralogy and petrology,* 66**,** 113-117.

FREZZOTTI, M. L., TECCE, F. & CASAGLI, A. 2012. Raman spectroscopy for fluid inclusion analysis. *Journal of Geochemical Exploration,* 112**,** 1-20.

FROST, R. L., XI, Y., POGSON, R. E., MILLAR, G. J., TAN, K. & PALMER, S. J. 2012. Raman spectroscopy of synthetic CaHPO4· 2H2O–and in comparison with the cave mineral brushite. *Journal of Raman Spectroscopy,* 43**,** 571-576.

GORBATSCHEV, R. & BOGDANOVA, S. 1993. Frontiers in the Baltic shield. *Precambrian Research,* 64**,** 3-21.

GORBATSCHEV, R. & GAÁL, G. 1987. The Precambrian history of the Baltic shield. *Proterozic Lithospheric Evolution***,** 149-159.

GRIFFIN, W., TAYLOR, P., HAKKINEN, J., HEIER, K., IDEN, I., KROGH, E., MALM, O., OLSEN, K., ORMAASEN, D. & TVETEN, E. 1978. Archaean and proterozoic crustal evolution in Lofoten–Vesterålen, N Norway. *Journal of the Geological Society,* 135**,** 629-647.

GROVES, D. I., GOLDFARB, R. J., GEBRE-MARIAM, M., HAGEMANN, S. & ROBERT, F. 1998. Orogenic gold deposits: a proposed classification in the context of their crustal distribution and relationship to other gold deposit types. *Ore geology reviews,* 13**,** 7-27.

GROVES, D. I., SANTOSH, M., GOLDFARB, R. J. & ZHANG, L. 2018. Structural geometry of orogenic gold deposits: Implications for exploration of world-class and giant deposits. *Geoscience Frontiers.*

GUIDOTTI, C. V., CHENEY, J. & GUGGENHEIM, S. 1977. Distribution of titanium between coexisting muscovite and biotite in pelitic schists from northwestern Maine. *American Mineralogist,* 62**,** 438-448.

HAGEMANN, S. & CASSIDY, K. 2001. World-class gold camps and deposits in the Eastern Goldfields Province, Yilgarn Craton: diversity in host rocks, structural controls, and mineralization styles. *World-class gold camps and deposits in the eastern Yilgarn Craton, Western Australia, with special emphasis on the Eastern Goldfields Province. Geological Survey of Western Australia Record,* 17**,** 7-44.

HENKEL, H. 1989. Magnetic crustal structures in northern Fennoscandia. *Tectonophysics,* 192**,** 57-79.

HOLLAND, T. & REDFERN, S. 1997. UNITCELL: a nonlinear least-squares program for cell-parameter refinement and implementing regression and deletion diagnostics. *Journal of Applied Crystallography,* 30**,** 84-84.

HOLTTA, P., BALAGANSKY, V., GARDE, A. A., MERTANEN, S., PELTONEN, P., SLABUNOV, A., SORJONEN-WARD, P. & WHITEHOUSE, M. 2008. Archean of Greenland and Fennoscandia. *Episodes,* 31**,** 13-19.

HÖLTTÄ P, B. V., GARDE V, MERTANEN S, PELTONEN P, SLABUNOV A, SORJONEN P, WARD & WHITEHOUSE M 2008. Archean of Greenland and Fennoscandia. *Episodes,* 31.

INDREVÆR, K., BERGH, S. G., KOEHL, J.-B., HANSEN, J.-A., SCHERMER, E. R. & INGEBRIGTSEN, A. 2013. Post-Caledonian brittle fault zones on the hyperextended SW Barents Sea margin: New insights into onshore and offshore margin architecture. *Norwegian Journal of Geology,* 93.

KARHU, J. A. 1996. Paleoproterozoic evolution of the carbon isotope ratios of sedimentary carbonates in the Fennoscandian Shield.

KIKUCHI, S. 1928. Diffraction of cathode rays by mica. *Proceedings of the Imperial Academy,* 4**,** 271-274.

KIM, Y.-S., PEACOCK, D. C. & SANDERSON, D. J. 2004. Fault damage zones. *Journal of structural geology,* 26**,** 503-517.

KOISTINEN, T. 2001. *Geological Map of the Fennoscandian Shield [: Scale 1: 2 000 000,* Geological Survey of Finland.

KRANIDIOTIS, P. & MACLEAN, W. 1987. Systematics of chlorite alteration at the Phelps Dodge massive sulfide deposit, Matagami, Quebec. *Economic Geology,* 82**,** 1898-1911.

KULLERUD, K., CORFU, F., BERGH, S., DAVIDSEN, B. & RAVNA, E. 2006a. U-Pb constraints on the archaean and early proterozoic evolution of the west troms basement complex, North Norway. *Bulletin of the Geological Society of Finland Special Issue I,* 79.

KULLERUD, K., SKJERLIE, K. P., CORFU, F. & JESÚS, D. 2006b. The 2.40 Ga Ringvassøy mafic dykes, West Troms Basement Complex, Norway: the concluding act of early Palaeoproterozoic continental breakup. *Precambrian Research,* 150**,** 183-200.

LAHTINEN, R., GARDE, A. A. & MELEZHIK, V. A. 2008. Paleoproterozoic evolution of Fennoscandia and Greenland. *Episodes,* 31**,** 20.

LARSON, S. Å. & BERGLUND, J. 1992. A chronological subdivision of the Transscandinavian Igneous Belt—three magmatic episodes? *Geologiska Föreningen i Stockholm Förhandlingar,* 114**,** 459-461.

MARTEL, S. J. 1997. Effects of cohesive zones on small faults and implications for secondary fracturing and fault trace geometry. *Journal of Structural Geology,* 19**,** 835-847.

MCCUAIG, T. C. & KERRICH, R. 1998. P—T—t—deformation—fluid characteristics of lode gold deposits: evidence from alteration systematics. *Ore Geology Reviews,* 12**,** 381-453.

MISRA, S. N. 1971. Chemical distinction of high-grade ortho-and para-metabasites. *Norsk Geologisk Tidsskrift,* 51**,** 311-316.

MOTUZA, G., MOTUZA, V., BELIATSKY, B. & SAVVA, E. Volcanic rocks of the Ringvassøya Greenstone Belt (North Norway): implication for the stratigraphy and tectonic setting. Journal of Conference, 2001. 577-578.

MUCCIO, Z. & JACKSON, G. P. 2009. Isotope ratio mass spectrometry. *Analyst,* 134**,** 213-222.

MYHRE, P. I., CORFU, F. & BERGH, S. 2011. Palaeoproterozoic (2.0–1.95 Ga) pre-orogenic supracrustal sequences in the West Troms Basement Complex, North Norway. *Precambrian Research,* 186**,** 89-100.

MYHRE, P. I., CORFU, F., BERGH, S. G. & KULLERUD, K. 2013. U-Pb geochronology along an Archaean geotransect in the West Troms Basement Complex, North Norway. *Norwegian Journal of Geology/Norsk Geologisk Forening,* 93.

NEUFELD, K. 2007. *Lattice preferred orientation in omphacite: examples from the Tauern Window, Austria and the Western Gneiss Region, Norway.* PhD thesis, Universität Mainz.

NIIRANEN, T., LAHTI, I. & NYKÄNEN, V. 2015. The Orogenic Gold Potential of the Central Lapland Greenstone Belt, Northern Fennoscandian Shield. *Mineral Deposits of Finland.* Elsevier.

OLESEN, O., TORSVIK, T. H. & TVETEN, E. 1997. Basement structure of the continental margin in the Lofoten-Lopphavet area, northern Norway: constraints from potential field data, on-land structural mapping and palaeomagnetic data. *Oceanographic Literature Review,* 12**,** 1478.

OSBORN, E. 1962. Reaction series for subalkaline igneous rocks based on different oxygen pressure conditions. *Amer. Mineral.,* 7**,** 211-226.

PEDERSEN, B. 1997. Strukturell analyses av en prekambrisk, duktilt deformert metasuprakrustalsone (Astridal-skjærsonen?) på NØ-Senja, Troms. *Unpublished Cand. Scient. thesis, University of Tromsø.*

PITCAIRN, I. K., TEAGLE, D. A., CRAW, D., OLIVO, G. R., KERRICH, R. & BREWER, T. S. 2006. Sources of metals and fluids in orogenic gold deposits: insights from the Otago and Alpine Schists, New Zealand. *Economic Geology,* 101**,** 1525-1546.

PRIYATKINA, N. 2013. *Petrogenesis and tectonic setting of the mafic-ultramafic rock association from NW Senja, West Troms Basement Complex.* Universitetet i Tromsø.

RIMŠAITE, J. 1964. On micas from magmatic and metamorphic rocks. *Beiträge zur Mineralogie und Petrographie,* 10**,** 152-183.

RISPOLI, R. 1981. Stress fields about strike-slip faults inferred from stylolites and tension gashes. *Tectonophysics,* 75**,** T29-T36.

ROBB, L. 2004. *Introduction to ore-forming processes*, Blackwell publishing.

ROBERT, F., BOULLIER, A. M. & FIRDAOUS, K. 1995. Gold‐quartz veins in metamorphic terranes and their bearing on the role of fluids in faulting. *Journal of Geophysical Research: Solid Earth,* 100**,** 12861-12879.

SCHIDLOWSKI, M., APPEL, P. W., EICHMANN, R. & JUNGE, C. E. 1979. Carbon isotope geochemistry of the 3.7×10^9-yr-old Isua sediments, West Greenland: implications for the Archaean carbon and oxygen cycles. *Geochimica et Cosmochimica Acta,* 43**,** 189-199.

SCHWARTZ, A. J., KUMAR, M., ADAMS, B. L. & FIELD, D. P. 2000. *Electron backscatter diffraction in materials science*, Springer.

SHEPHERD, T. J., RANKIN, A. H. & ALDERTON, D. H. 1985. *A practical guide to fluid inclusion studies*, Blackie.

STIPP, M., STÜNITZ, H., HEILBRONNER, R. & SCHMID, S. M. 2002. Dynamic recrystallization of quartz: correlation between natural and experimental conditions. *Geological Society, London, Special Publications,* 200**,** 171-190.

SUNDBLAD, K. 2003. Metallogeny of gold in the Precambrian of northern Europe. *Economic geology,* 98**,** 1271-1290.

VAN BAALEN, M. 1993. Titanium mobility in metamorphic systems: a review. *Chemical Geology,* 110**,** 233-249.

WILCOX, R. E. & POLDERVAART, A. 1958. Metadolerite dike swarm in Bakersville-Roan mountain area, North Carolina. *Geological Society of America Bulletin,* 69**,** 1323-1368.

YAVUZ, F., KUMRAL, M., KARAKAYA, N., KARAKAYA, M. Ç. & YıLDıRıM, D. K. 2015. A Windows program for chlorite calculation and classification. *Computers & Geosciences,* 81, 101-113.

ZWAAN, K. 1995. Geology of the West Troms Basement Complex, northern Norway, with emphasis on the Senja Shear Belt: a preliminary account. Geological Survey of Norway Bulletin, 427, 33-36.

ZWAAN, K., FARETH, E. & GROGAN, P. 1998. Geologisk kart over Norge, berggrunnskart Tromsø, M 1: 250.000. Norges geologiske undersøkelse.

10 Appendix

Table 7. Chemical composition of chlorite.

CHLORITE

Element	Wt%	Wt% Sigma	oxides
O	43.35	0.25	
Mg	9.61	0.09	15.93603308
Al	10.87	0.09	41.0769405
Si	12.04	0.09	25.75759643
Fe	17.68	0.15	22.74507766
Ca			
Ti	0.25	0.04	0.4170781112
Mn			
Cl			
Cr	0.23	0.04	0.67231063
Total	94.02		

Element	Wt%	Wt% Sigma	oxides
O	35.06	0.23	
Mg	8.22	0.08	13.6310239
Al	8.7	0.08	32.8766812
Si	10.92	0.08	23.3615408
Fe	16.97	0.14	21.8316723
Ca	0.3	0.04	0.5004693734
Ti			
Mn			
Cl			
Cr	0.15	0.04	0.438466997
Total	80.32		

Element	Wt%	Wt% Sigma	oxides
O	43.02	0.24	
Mg	9.92	0.09	16.45009866
Al	10.6	0.09	40.0566013
Si	12.17	0.09	26.03570992
Fe	17.1	0.15	21.9889156
Ca			
Ti			
Mn			
Cl			
Cr	0.14	0.04	0.40923586
Total	92.97		

chlorite

Element	Wt%	Wt% Sigma	oxides
O	40.76	0.22	
Mg	9.12	0.09	15.1234778
Al	9.97	0.09	37.6590588
Si	12.16	0.09	26.0143165
Fe	17.24	0.15	22.1902369
Total	89.24		

Element	Wt%	Wt% Sigma	oxides
O	44.38	0.22	
Mg	9.69	0.09	16.06886517
Al	10.95	0.09	41.37925471
Si	11.84	0.09	25.3297293
Fe	16.99	0.15	21.8574021
Total	93.85		

CHLORITE

Element	Wt%	Wt% Sigma	oxides
O	41.25	0.26	
Mg	8.11	0.08	13.4862
Al	9.1	0.08	34.38824
Si	10.89	0.08	23.29726
Fe	17.69	0.15	22.7594
Ca	2.26	0.05	3.770386
Ti			
Mn	0.15	0.05	0.193684
Cr	0.27	0.04	0.789241
Total	89.73		

chlorite

Element	Wt%	Wt% Sigma	oxides
O	44.59	0.28	
Mg	5.05	0.07	8.374294178
Al	10.73	0.09	40.54789068
Si	22.28	0.11	47.66438024
Fe	8.63	0.11	11.10237671
Cr	0.11	0.04	0.321542465
Total	91.39		

TMF 002

chlorite

Element	Wt%	Wt% Sigma	Total
O	44.96	0.26	
Mg	9.99	0.09	16.56617799
Al	9.74	0.09	36.80675259
Si	12.5	0.09	26.74169055
Fe	18.87	0.15	24.27999615
Ca	0.19	0.03	0.2654902744
Ti	0.1	0.03	0.166831245
Mn	0.15	0.04	0.1938683971
Cl	0.31	0.03	
Cr			
Total	96.82		

Element	Wt%	Wt% Sigma	Total
O	46.03	0.25	
Mg	10.71	0.09	17.76013676
Al	11.35	0.09	42.89082565
Si	12.34	0.09	26.39939691
Fe	16.52	0.14	21.25275356
Ca	0.12	0.03	0.167304786
Ti			
Cl			
Cr	0.22	0.04	0.64308493
Total	97.31		

Element	Wt%	Wt% Sigma	chlorite
O	46.44	0.23	
Mg	10.74	0.09	17.80988504
Al	11.25	0.09	42.51293292
Si	12.42	0.09	26.57054373
Fe	16.46	0.14	21.17556438
Ca	0.13	0.03	0.181896851
Cl	0.16	0.03	
Total	97.6		

Element	Wt%	Wt% Sigma	oxides
O	45.71	0.25	
Mg	10.51	0.09	17.42848155
Al	11.17	0.09	42.21061873
Si	12.3	0.09	26.3138235
Fe	17.07	0.15	21.96032002
Ca	0.09	0.03	0.125926589
Cr	0.29	0.04	0.847702862
Total	97.14		

Element	Wt%	Wt% Sigma	oxides
O	41.16	0.24	
Mg	10.26	0.09	17.01391253
Al	10.25	0.09	38.73400555
Si	12.31	0.09	26.3352 1686
Fe	16.55	0.14	21.2913 4815
Cr	0.16	0.04	0.467098131
Total	90.68		

Table 8. Fluid inclusion data.

sample	P/PS/S	# of phases	fluid ratio	Tclath	TCO2h	Th	Td	salinity (wt% NaCl)	xCO2	xN2	r(bulk)	Vm (cc/mol)
006, 01												
bonmerang	P	L1+L2+V	L1=50, L2=45 V=5		29,5							
boundary	P	L1+L2+V	L1=85, L2=10 V=5	6,8	26,5		300	5,8			0,932038	20,813777
bean	P	L1+L2+V	L1=85, L2=10 V=5	7	28,7	290		6	90	10	0,935647	
dot	P	L1+L2+V	L1=50, L2=48 V=2	2,8	25		307	11,8	90	10		
006, 02												
eye	P	L1+L2+V	L1=65, L2=30 V=5	8,7	21,7		308	3,2			0,740106	26,813897
snake	P	L1+L2+V	L1=70, L2=25 V=5	5,8	26	306		6,8			0,809946	24,632031
006, 03												
golfclub	P	L1+L2+V	L1=50, L2=45 V=5	1,8	24,4			13,2			0,65123	32,288887
ellipsode	P	L1+L2+V	L1=85, L2=10 V=5	9,7	30	272		0,5			0,899175	21,305993
birdhead	P	L1+L2+V	L1=80, L2=15 V=5	7	24,4	306		6			0,886482	21,96034
gun	P	L1+L2+V	L1=70, L2=25 V=5									
006, 04												
fish	P	L1+L2+V	L1=90, L2=5 V=5	5,8	23,3			6,8			0,978775	19,714577
paperplane	P	L1+L2+V	L1=70, L2=25 V=5	8	21,9			4			0,787441	25,017392
seat	P	L1+L2+V	L1=95, L2=3 V=2	10	28			0			0,971274	19,378599
lap	P	L1+L2+V	L1=70, L2=25 V=5	7,8	27,7			4,2			0,799632	24,836807
eye	P	L1+L2+V	L1=50, L2=45 V=5		30		350					
star	P	L+V?	L=50 V=45	8			430					
006, 05												
needle	P	L1+L2+V	L1=85, L2=10 V=5	11	29							
star	P	L1+L2+V	L1=50, L2=45 V=5	6,7	27,1	250		6,4			0,641537	32,814129
in line	P	L1+L2+V	L1=85, L2=10 V=5	6,6	27,3			6,3			0,93606	20,76466
mini	P	L1+L2+V?	L1=50, L2=48 V=2	7,2	23,5			5,8			0,627689	33,182364
gigantisk	P	L1+L2+V	L1=50, L2=45 V=5	2,9	23,3			12,2			0,650763	32,480922
006, 06												
tear drop	P	L1+L2+V	L1=50, L2=45 V=5	6,8	25,8	323		5,8			0,634945	32,996514
wierd	P	L1+L2+V	L1=65, L2=25 V=10	7	27,7	250		6			0,767445	26,291115
triangle	P	L1+L2+V	L1=75, L2=10 V=5	8	30			4			0,843725	23,352993
heart	P	L1+L2+V	L1=55, L2=40 V=5	7,9	27,9			4,1			0,676544	30,516007
ghost	P	L1+L2+V	L1=85, L2=10 V=5	3,4	19,5	297		11,6			0,961388	20,432309
twist	P	L1+L2+V	L1=50, L2=45 V=5	7,4	27,1		260	5,2			0,637018	32,960202
006, 07												
heart	P	L1+L2+V	L1=50, L2=45 V=5	6,3	19,5			6,1			0,617038	33,426253
pen	P	L1+L2+V	L1=65, L2=20 V=5	7,4	27,4			5,2			0,76279	26,384672
triangle	P	L1+L2+V	L1=75, L2=20 V=5	10	30	290		0			0,818084	23,83953

XRD - Sample TMF 004
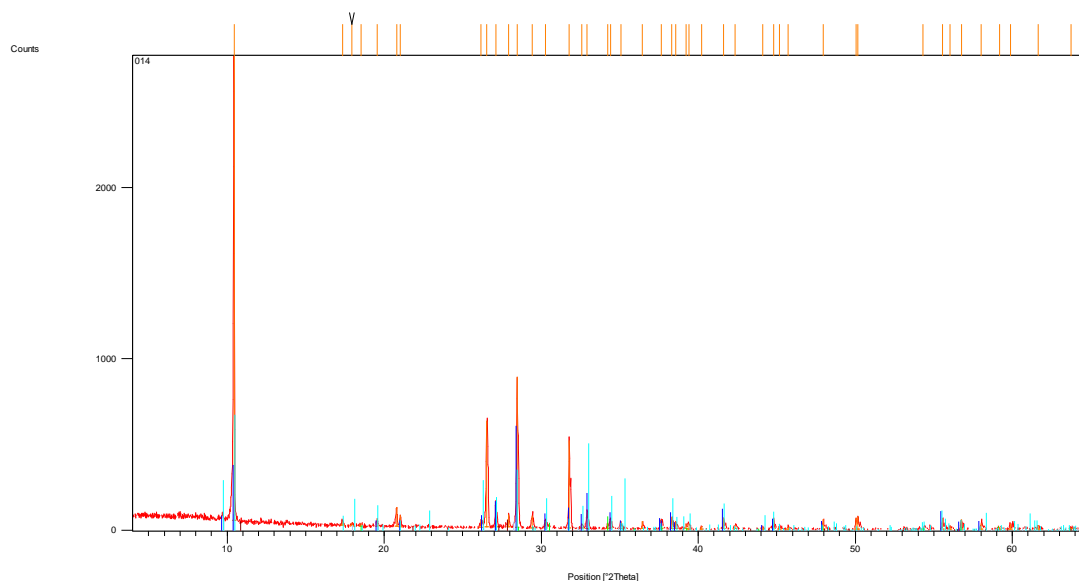
Pos. [°2Th.]	Height [cts]	FWHM [°2Th.]	d-spacing [A]	Rel. Int. [%]	Tip width [°2Th.]	Matched by
10,4390	2734,79	0,0787	8,47452	100,00	0,0945	00-021-0149; 01-089-5366
17,3563	20,18	0,1181	5,10946	0,74	0,1417	01-089-5366
17,9400	16,00	0,0900	4,94453	0,59	0,1080	
18,5400	16,00	0,0900	4,78584	0,59	0,1080	00-047-1815; 01-089-5366
19,5501	40,08	0,1181	4,54079	1,47	0,1417	00-021-0149; 01-089-5366
20,7886	114,10	0,0787	4,27298	4,17	0,0945	01-089-8936

21,0267	66,98	0,0787	4,22513	2,45	0,0945	00-021-0149; 01-089-5366
26,1775	47,00	0,0900	3,40429	1,72	0,1080	00-021-0149; 01-089-5366
26,5479	619,90	0,0787	3,35764	22,67	0,0945	01-089-8936
27,1174	140,85	0,1181	3,28840	5,15	0,1417	00-021-0149; 01-089-5366
27,9203	72,57	0,0787	3,19564	2,65	0,0945	03-065-3928
28,4712	880,19	0,0984	3,13504	32,18	0,1181	00-021-0149; 00-047-1815; 01-089-5366
29,4317	69,63	0,1378	3,03488	2,55	0,1653	03-065-3928; 01-089-5366
30,2903	41,49	0,1181	2,95078	1,52	0,1417	00-021-0149; 01-089-5366
31,7831	511,74	0,0590	2,81552	18,71	0,0708	00-021-0149; 01-089-5366
32,5902	18,01	0,0900	2,74761	0,66	0,1080	00-021-0149; 01-089-5366
32,9168	94,87	0,0590	2,72109	3,47	0,0708	00-021-0149; 03-065-3928; 01-089-5366

34,2302	30,00	0,0900	2,61963	1,10	0,1080	00-047-1815
34,4293	45,91	0,1574	2,60493	1,68	0,1889	00-021-0149; 01-089-5366
35,0711	36,00	0,1181	2,55873	1,32	0,1417	00-021-0149; 01-089-5366
36,4545	45,64	0,0590	2,46474	1,67	0,0708	01-089-8936; 01-089-5366
37,6614	48,94	0,1574	2,38848	1,79	0,1889	00-021-0149; 00-047-1815; 01-089-5366
38,3264	67,27	0,1378	2,34856	2,46	0,1653	00-021-0149; 01-089-5366
38,5702	39,00	0,0900	2,33427	1,43	0,1080	00-021-0149; 01-089-5366
39,2228	27,64	0,0900	2,29692	1,01	0,1080	00-047-1815
39,4114	28,95	0,1968	2,28636	1,06	0,2362	01-089-8936; 00-047-1815; 01-089-5366
40,2028	15,00	0,0900	2,24316	0,55	0,1080	01-089-8936
41,6240	63,93	0,0590	2,16980	2,34	0,0708	00-021-0149; 01-089-5366
42,3438	21,64	0,1574	2,13457	0,79	0,1889	01-089-8936; 00-047-1815;

						01-089-5366
44,1084	10,66	0,2362	2,05318	0,39	0,2834	00-021-0149
44,7949	48,90	0,0590	2,02330	1,79	0,0708	00-021-0149; 01-089-5366
45,1888	18,55	0,1968	2,00658	0,68	0,2362	01-089-5366
45,7269	12,00	0,2362	1,98421	0,44	0,2834	01-089-8936; 01-089-5366
47,9622	55,52	0,0787	1,89683	2,03	0,0945	00-021-0149; 00-047-1815; 03-065-3928; 01-089-5366
50,0461	64,30	0,0720	1,82111	2,35	0,0864	01-089-8936; 01-089-5366
50,1735	74,42	0,0720	1,81679	2,72	0,0864	01-089-5366
54,3001	6,83	0,6298	1,68946	0,25	0,7557	00-047-1815; 01-089-5366
55,5725	63,93	0,0787	1,65375	2,34	0,0945	00-021-0149; 01-089-5366
56,0300	21,00	0,0900	1,64133	0,77	0,1080	01-089-5366
56,7519	58,80	0,0787	1,62216	2,15	0,0945	00-047-1815; 03-065-3928; 01-089-5366

58,0284	34,83	0,1574	1,58948	1,27	0,1889	00-021-0149; 01-089-5366
59,1766	12,57	0,2362	1,56135	0,46	0,2834	00-047-1815; 03-065-3928; 01-089-5366
59,8725	30,52	0,0787	1,54485	1,12	0,0945	01-089-8936
61,6632	25,36	0,1181	1,50422	0,93	0,1417	01-089-5366
63,7266	5,87	0,3936	1,46040	0,21	0,4723	01-089-8936; 00-047-1815; 03-065-3928; 01-089-5366
64,6207	93,79	0,0720	1,44114	3,43	0,0864	01-089-5366

XRD - SAMPLE TMF 016
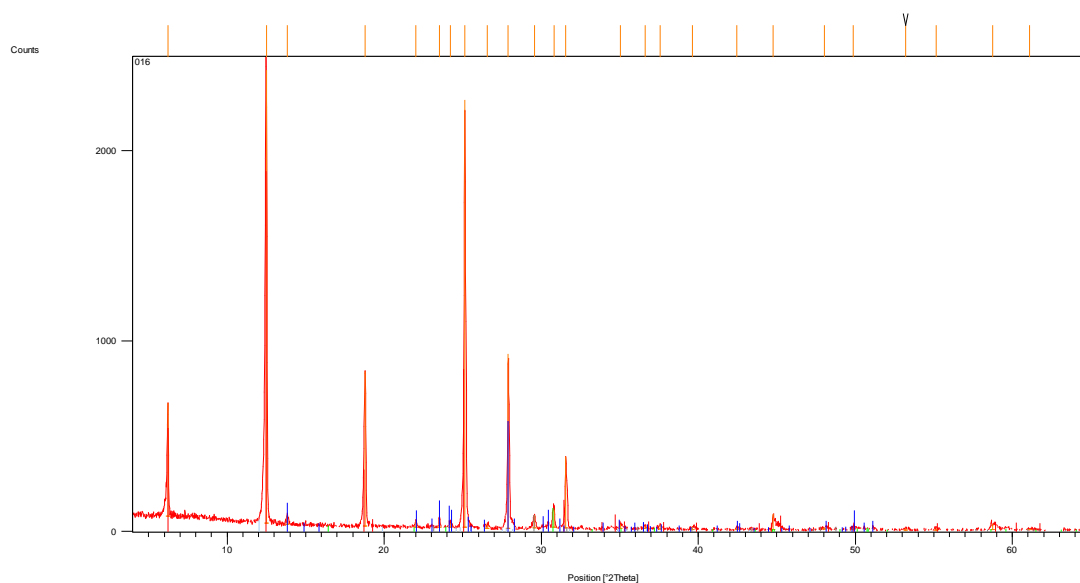
Pos. [°2Th.]	Height [cts]	FWHM [°2Th.]	d-spacing [A]	Rel. Int. [%]	Tip width [°2Th.]	Matched by
6,2357	595,80	0,0787	14,17423	25,02	0,0945	00-022-0712
12,4985	2380,87	0,0984	7,08229	100,00	0,1181	00-022-0712
13,8418	48,82	0,1181	6,39786	2,05	0,1417	00-009-0466
18,7910	813,29	0,1181	4,72248	34,16	0,1417	00-022-0712
22,0237	31,62	0,1181	4,03607	1,33	0,1417	00-009-0466; 00-041-0586
23,5186	55,59	0,0590	3,78280	2,33	0,0708	00-009-0466
24,2075	22,24	0,1968	3,67668	0,93	0,2362	00-009-0466; 00-041-0586
25,1364	2248,42	0,1181	3,54288	94,44	0,1417	00-022-0712; 00-009-0466
26,5557	19,12	0,3936	3,35667	0,80	0,4723	00-009-0466
27,8994	918,29	0,0984	3,19799	38,57	0,1181	00-009-0466
29,5607	68,08	0,1378	3,02193	2,86	0,1653	01-086-2335
30,8078	90,10	0,1181	2,90238	3,78	0,1417	00-041-0586
31,5705	376,37	0,0984	2,83399	15,81	0,1181	00-022-0712; 00-009-0466; 01-086-2335

35,0609	22,89	0,2362	2,55945	0,96	0,2834	00-022-0712; 00-009-0466; 00-041-0586
36,6117	17,09	0,2362	2,45451	0,72	0,2834	00-022-0712; 00-009-0466
37,5833	19,46	0,2362	2,39327	0,82	0,2834	00-022-0712; 00-009-0466
39,6339	14,18	0,3149	2,27404	0,60	0,3779	00-022-0712; 00-009-0466; 01-086-2335
42,4494	10,38	0,2362	2,12950	0,44	0,2834	00-009-0466
44,7738	82,23	0,0590	2,02421	3,45	0,0708	00-022-0712; 00-041-0586
48,0502	10,44	0,4723	1,89356	0,44	0,5668	00-022-0712; 00-009-0466; 01-086-2335
49,8625	13,73	0,3149	1,82890	0,58	0,3779	00-022-0712; 00-009-0466; 00-041-0586
53,2098	7,77	0,4723	1,72147	0,33	0,5668	
55,1423	8,90	0,4723	1,66563	0,37	0,5668	00-022-0712
58,7458	29,54	0,4723	1,57176	1,24	0,5668	00-022-0712; 00-041-0586

| | | | | | | 61,1110 | 2,80 | 1,1520 | 1,51522 | 0,12 | 1,3824 | 01-086-2335 |

Visible	Ref. Code	Score	Compound Name	Displacement [°2Th.]	Scale Factor	Chemical Formula
*	00-022-0712	51	Nimite-1\ITM\RG#I#I\IT#b\RG	0,000	0,733	(Ni , Mg , Al)6 (Si , Al)4 O10 (O H)8
*	00-009-0466	37	Albite, ordered	0,000	0,224	Na Al Si3 O8
*	00-041-0586	29	Ankerite	0,000	0,039	Ca (Fe +2 , Mg) (C O3)2
*	01-086-2335	22	Calcite, magnesian	0,000	0,027	(Mg.064 Ca.936) (C O3)
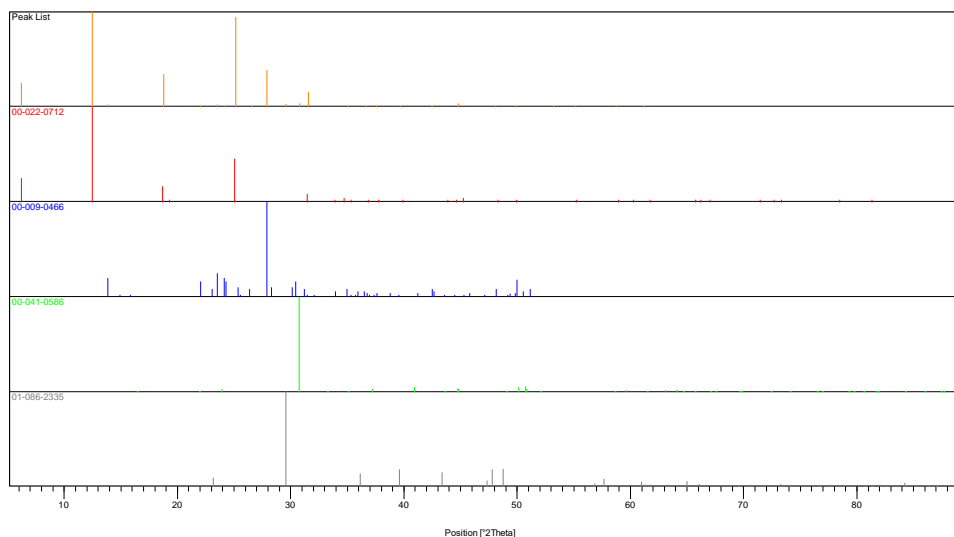
XRD – SAMPLE TMF 017
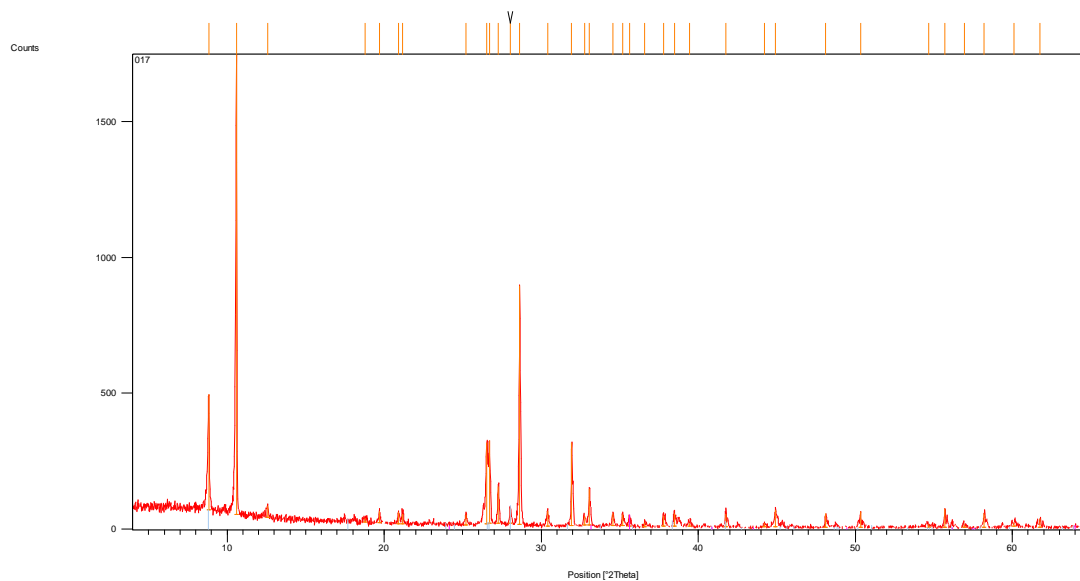
Pos. [°2Th.]	Height [cts]	FWHM [°2Th.]	d-spacing [A]	Rel. Int. [%]	Tip width [°2Th.]	Matched by
8,8281	426,29	0,0984	10,01695	25,05	0,1181	00-042-1414
10,5885	1701,47	0,0787	8,35516	100,00	0,0945	00-045-1371
12,5664	42,31	0,1181	7,04421	2,49	0,1417	00-052-1044
18,7808	15,96	0,2362	4,72501	0,94	0,2834	00-052-1044
19,7062	44,17	0,1181	4,50516	2,60	0,1417	00-045-1371
20,9188	43,16	0,1181	4,24669	2,54	0,1417	01-078-1253
21,1778	37,73	0,1181	4,19533	2,22	0,1417	00-045-1371
25,2160	38,83	0,1574	3,53188	2,28	0,1889	00-052-1044

26,5328	297,55	0,0984	3,35951	17,49	0,1181	00-042-1414; 01-078-1253
26,7090	305,19	0,1181	3,33774	17,94	0,1417	00-042-1414; 01-078-1253
27,2614	134,25	0,0984	3,27135	7,89	0,1181	00-045-1371
28,0338	54,38	0,0787	3,18296	3,20	0,0945	
28,6293	880,58	0,0984	3,11809	51,75	0,1181	00-045-1371
30,4067	56,41	0,1574	2,93976	3,32	0,1889	00-045-1371
31,9414	303,93	0,0590	2,80192	17,86	0,0708	00-045-1371
32,7562	32,11	0,1181	2,73406	1,89	0,1417	00-045-1371
33,0663	132,86	0,0590	2,70913	7,81	0,0708	00-045-1371; 00-042-1414; 01-073-0603
34,5759	45,33	0,1181	2,59423	2,66	0,1417	00-045-1371
35,2037	40,34	0,1574	2,54939	2,37	0,1889	00-045-1371
35,6392	28,44	0,1181	2,51923	1,67	0,1417	01-073-0603
36,6023	14,74	0,2362	2,45513	0,87	0,2834	01-078-1253
37,8090	39,14	0,1968	2,37949	2,30	0,2362	00-045-1371
38,4852	47,04	0,1181	2,33923	2,76	0,1417	00-045-1371

39,4551	10,00	0,2362	2,28393	0,59	0,2834	00-045-1371; 00-042-1414; 01-078-1253
41,7492	47,62	0,0590	2,16359	2,80	0,0708	00-045-1371
44,2243	13,33	0,1968	2,04807	0,78	0,2362	00-045-1371
44,9186	61,53	0,1968	2,01801	3,62	0,2362	00-045-1371
48,1226	50,31	0,0984	1,89088	2,96	0,1181	00-045-1371
50,3297	58,38	0,0720	1,81151	3,43	0,0864	00-045-1371; 01-078-1253
54,6829	10,66	0,4723	1,67853	0,63	0,5668	00-045-1371; 00-042-1414
55,7118	69,63	0,0787	1,64995	4,09	0,0945	00-045-1371; 00-042-1414
56,9494	10,70	0,2362	1,61700	0,63	0,2834	00-045-1371
58,2156	50,98	0,1181	1,58481	3,00	0,1417	00-045-1371
60,1035	14,43	0,3149	1,53947	0,85	0,3779	00-045-1371; 00-042-1414; 01-078-1253
61,7780	33,56	0,0787	1,50170	1,97	0,0945	00-045-1371
64,7945	60,72	0,0960	1,43770	3,57	0,1152	00-045-1371

Visible	Ref. Code	Score	Compound Name	Displacement [°2Th.]	Scale Factor	Chemical Formula
	00-045-1371	42	Magnesiohornblende, ferroan	0,000	0,232	Ca2 (Mg , Fe +2)4 Al (Si7 Al) O22 (O H , F)2
	00-042-1414	21	Biotite-1\ITM\RG	0,000	0,210	K (Mg , Fe +2)3 (Al , Fe +3) Si3 O10 (O H , F)2
	00-052-1044	25	Chlorite-serpentine	0,000	0,019	(Mg , Al)6 (Si , Al)4 O10 (O H)8
	01-078-1253	41	Silicon oxide - $-alpha	0,000	0,115	Si O2
*	01-073-0603	28	Iron(III) oxide - $-alpha	0,000	0,024	Fe2 O3
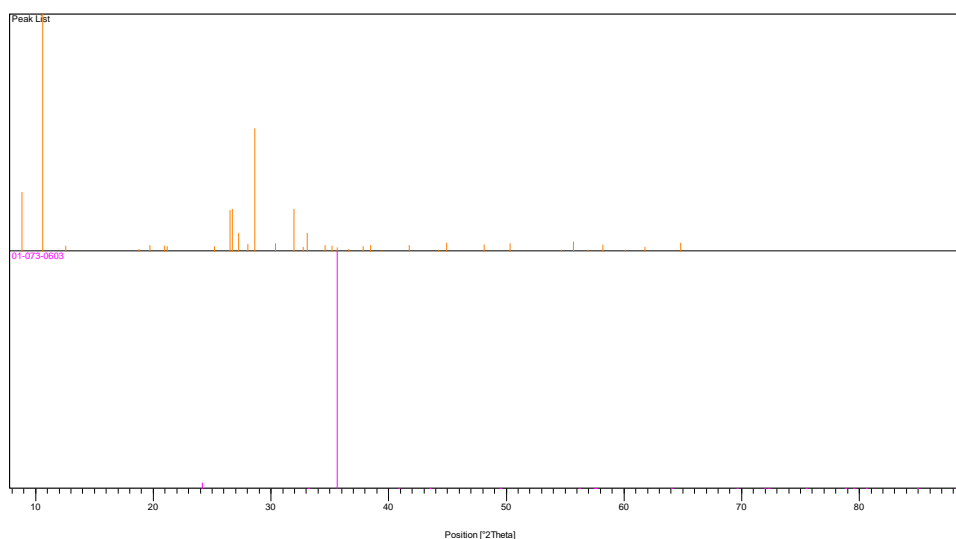
Position [°2Theta]

Visible	Ref. Code	Score	Compound Name	Displacement [°2Th.]	Scale Factor	Chemical Formula
	01-089-8936	43	Silicon oxide - $-alpha	0,000	0,260	Si O2
*	00-021-0149	43	Magnesiohornblende, ferroan	0,000	0,206	Ca2 (Mg , Fe)5 (Si , Al)8 O22 (O H)2
*	00-047-1815	27	Spessartine, vanadian	0,000	0,024	(Mn , Ca)3 (Al , V)2 Si3 O12
*	03-065-3928	15	Covellite	0,000	0,015	Cu S
*	01-089-5366	21	Actinolite	0,000	0,215	(Mg , Ca , Fe , Na , Al , Mn , Ti)7 (Na , K)0.16 (Si Al)8O22 (O H)1.4 F0.46
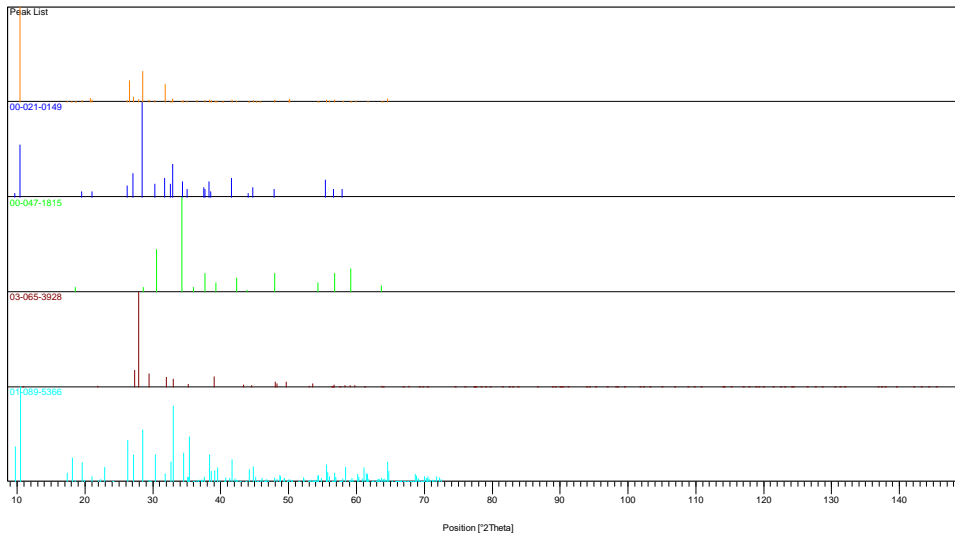
XRD – SAMPLE TMF 021
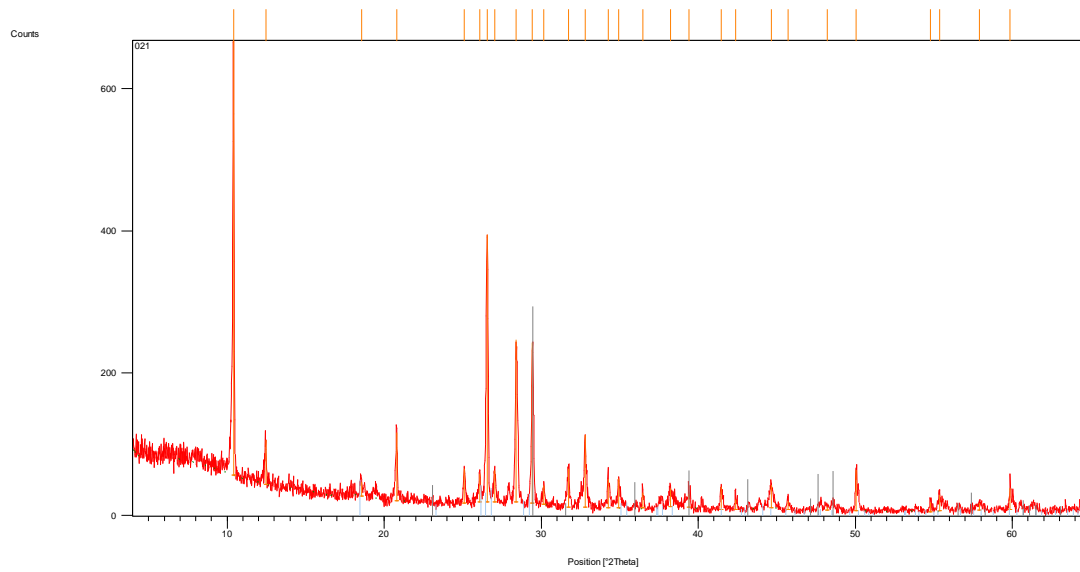
Pos. [°2Th.]	Height [cts]	FWHM [°2Th.]	d-spacing [A]	Rel. Int. [%]	Tip width [°2Th.]	Matched by
10,4045	624,14	0,0787	8,50250	100,00	0,0945	00-021-0149
12,4627	62,39	0,0984	7,10260	10,00	0,1181	00-022-0712
18,5746	19,27	0,2362	4,77701	3,09	0,2834	00-022-0712
20,7948	96,40	0,0787	4,27172	15,45	0,0945	01-089-8936; 00-021-0149
25,1052	48,52	0,1181	3,54722	7,77	0,1417	00-022-0712
26,0883	39,20	0,1181	3,41573	6,28	0,1417	00-021-0149
26,5558	376,00	0,1181	3,35665	60,24	0,1417	01-089-8936
27,0420	43,60	0,1181	3,29740	6,99	0,1417	00-021-0149
28,3923	228,10	0,1574	3,14357	36,55	0,1889	00-021-0149
29,4436	225,87	0,1378	3,03368	36,19	0,1653	01-072-1652
30,1710	26,36	0,1181	2,96218	4,22	0,1417	00-021-0149
31,7295	54,40	0,1574	2,82015	8,72	0,1889	00-021-0149; 01-072-1652
32,7921	102,25	0,0787	2,73115	16,38	0,0945	00-021-0149
34,2859	41,05	0,1574	2,61551	6,58	0,1889	00-021-0149

34,9354	41,87	0,1181	2,56835	6,71	0,1417	00-021-0149
36,4853	22,15	0,1181	2,46273	3,55	0,1417	01-089-8936
38,2227	25,31	0,2362	2,35469	4,06	0,2834	00-021-0149
39,3943	18,96	0,2362	2,28732	3,04	0,2834	01-089-8936; 01-072-1652
41,4700	32,05	0,1574	2,17751	5,14	0,1889	00-021-0149
42,3902	14,26	0,1968	2,13234	2,29	0,2362	01-089-8936
44,6606	32,81	0,3149	2,02907	5,26	0,3779	00-021-0149; 00-022-0712
45,7361	12,27	0,2362	1,98383	1,97	0,2834	01-089-8936
48,2258	5,29	0,9446	1,88707	0,85	1,1336	00-022-0712
50,0580	57,38	0,0787	1,82221	9,19	0,0945	01-089-8936; 00-022-0712
54,7981	12,99	0,2362	1,67528	2,08	0,2834	01-089-8936
55,3908	22,57	0,2362	1,65875	3,62	0,2834	01-089-8936; 00-021-0149; 00-022-0712
57,9229	9,97	0,6298	1,59212	1,60	0,7557	00-021-0149
59,8537	30,46	0,1440	1,54401	4,88	0,1728	01-089-8936

Visible	Ref. Code	Score	Compound Name	Displacement [°2Th.]	Scale Factor	Chemical Formula
	01-089-8936	59	Silicon oxide - $-alpha	0,000	0,682	Si O2
	00-021-0149	38	Magnesiohornblende, ferroan	0,000	0,590	Ca2 (Mg , Fe)5 (Si , Al)8 O22 (O H)2
	00-022-0712	28	Nimite-1\ITM\RG# I#I\IT#b\RG	0,000	0,094	(Ni , Mg , Al)6 (Si , Al)4 O10 (O H)8
*	01-072-1652	23	Calcite	0,000	0,394	Ca C O3
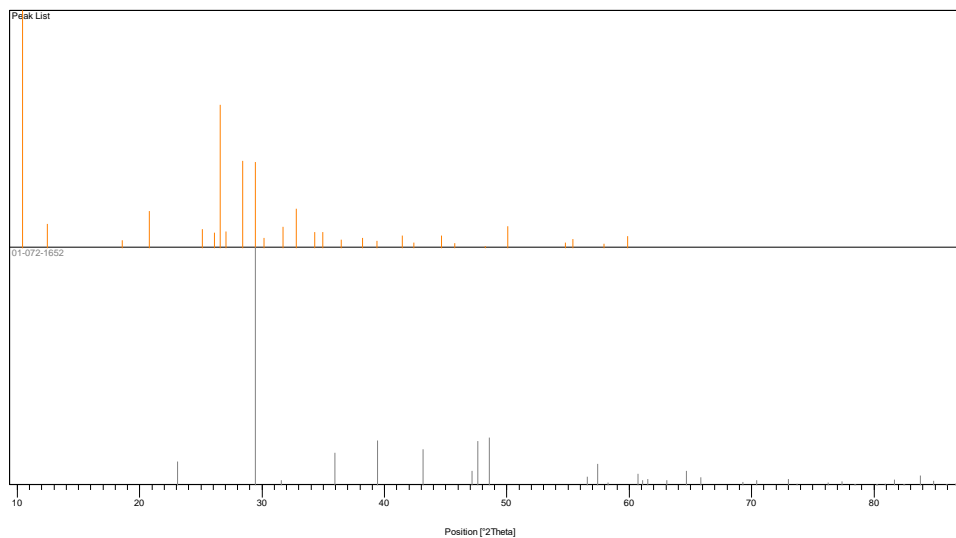
XRD – SAMPLE TMF 022 (RG1)
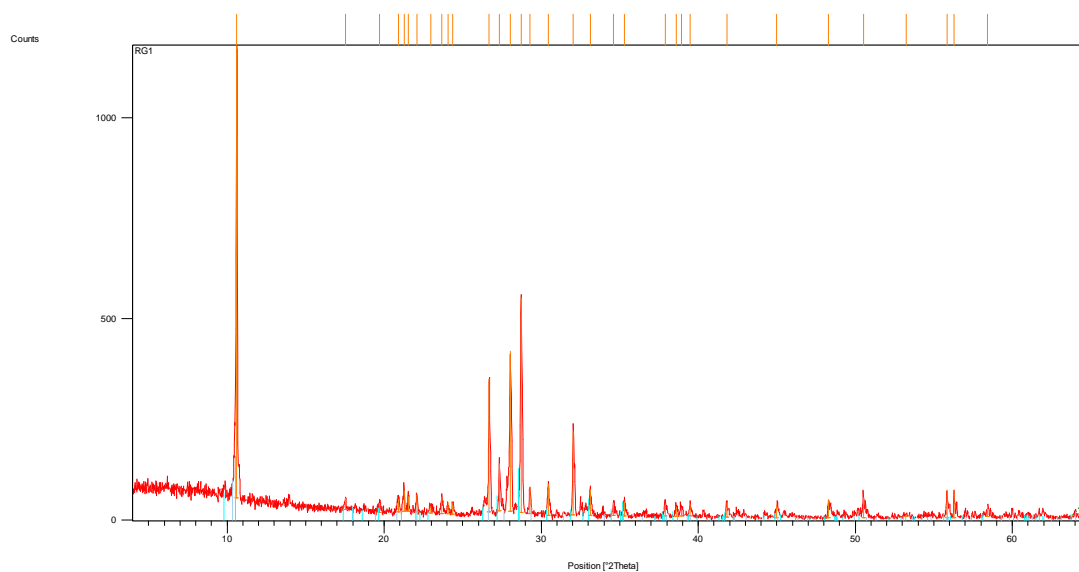
Pos. [°2Th.]	Height [cts]	FWHM [°2Th.]	d-spacing [A]	Rel. Int. [%]	Tip width [°2Th.]	Matched by
10,6198	1148,70	0,0787	8,33064	100,00	0,0945	01-085-0392; 01-077-0187; 00-045-1371
17,5437	30,00	0,0900	5,05532	2,61	0,1080	01-085-0392; 01-077-0187
19,6861	22,25	0,2362	4,50974	1,94	0,2834	01-085-0392; 00-045-1371
20,8975	31,32	0,1181	4,25096	2,73	0,1417	01-085-0796
21,2692	52,92	0,0787	4,17751	4,61	0,0945	01-077-0187
21,5513	37,65	0,1181	4,12345	3,28	0,1417	01-085-0392
22,0751	43,04	0,1181	4,02679	3,75	0,1417	00-041-1480; 01-077-0187;

						00-045-1371
22,9780	16,81	0,2362	3,87056	1,46	0,2834	00-041-1480; 01-085-0392; 01-077-0187
23,6693	40,03	0,1181	3,75905	3,48	0,1417	00-041-1480; 01-085-0392
24,0600	30,00	0,0900	3,69889	2,61	0,1080	00-041-1480; 01-085-0392
24,3725	29,69	0,1181	3,65216	2,58	0,1417	00-041-1480; 01-077-0187
26,6934	331,09	0,1181	3,33966	28,82	0,1417	01-085-0796; 01-085-0392
27,3444	118,34	0,0984	3,26161	10,30	0,1181	01-077-0187; 00-045-1371
28,0392	399,09	0,0787	3,18236	34,74	0,0945	00-041-1480
28,7215	534,30	0,1378	3,10829	46,51	0,1653	01-085-0392; 01-077-0187
29,2680	65,65	0,0984	3,05148	5,72	0,1181	01-085-0392
30,4552	79,15	0,0984	2,93518	6,89	0,1181	00-041-1480; 01-085-0392; 00-045-1371
32,0358	208,81	0,0984	2,79388	18,18	0,1181	01-077-0187

33,1174	65,82	0,0787	2,70506	5,73	0,0945	01-077-0187; 00-045-1371
34,6070	32,72	0,1574	2,59197	2,85	0,1889	01-085-0392; 01-077-0187; 00-045-1371
35,2854	36,41	0,1574	2,54367	3,17	0,1889	00-041-1480; 01-085-0392; 01-077-0187; 00-045-1371
37,9206	28,98	0,1574	2,37275	2,52	0,1889	01-077-0187; 00-045-1371
38,5996	24,22	0,1181	2,33256	2,11	0,1417	00-041-1480; 01-085-0392; 01-077-0187; 00-045-1371
38,9258	21,33	0,1574	2,31376	1,86	0,1889	01-077-0187
39,4930	29,25	0,1181	2,28183	2,55	0,1417	01-085-0796; 00-041-1480; 01-085-0392; 01-077-0187; 00-045-1371
41,8202	36,02	0,1968	2,16008	3,14	0,2362	00-041-1480; 01-077-0187; 00-045-1371

45,0071	31,70	0,1968	2,01425	2,76	0,2362	00-041-1480; 01-085-0392; 01-077-0187; 00-045-1371
48,2960	45,87	0,0787	1,88449	3,99	0,0945	00-041-1480; 01-085-0392
50,5133	50,58	0,1574	1,80685	4,40	0,1889	01-085-0796; 01-085-0392; 01-077-0187
53,2470	5,24	0,4723	1,72036	0,46	0,5668	00-041-1480; 01-085-0392; 01-077-0187; 00-045-1371
55,8373	69,28	0,0720	1,64517	6,03	0,0864	01-085-0392; 01-077-0187; 00-045-1371
56,2979	67,96	0,0720	1,63280	5,92	0,0864	01-085-0392; 01-077-0187
58,4321	28,38	0,1440	1,57815	2,47	0,1728	00-041-1480; 01-085-0392; 01-077-0187

Visible	Ref. Code	Score	Compound Name	Displacement [°2Th.]	Scale Factor	Chemical Formula
	01-085-0796	43	Quartz	0,000	0,169	Si O2
	00-041-1480	38	Albite, calcian, ordered	0,000	0,227	(Na , Ca) Al (Si , Al)3 O8
	01-085-0392	16	Cummingtonite manganoan	0,000	0,167	Na0.1 Ca0.4 Mg5.6 Mn1.0 Si8 O22 (O H)2
	01-077-0187	19	Riebeckite	0,000	0,549	Na1.38 K0.13 Ca0.17 Mg0.25 Mg2.81 Fe1.66 Fe0.48 Al0.04 Si7.94 O22(O H)2
*	00-045-1371	15	Magnesiohornblende, ferroan	0,000	0,088	Ca2 (Mg , Fe +2)4 Al (Si7 Al) O22 (O H , F)2
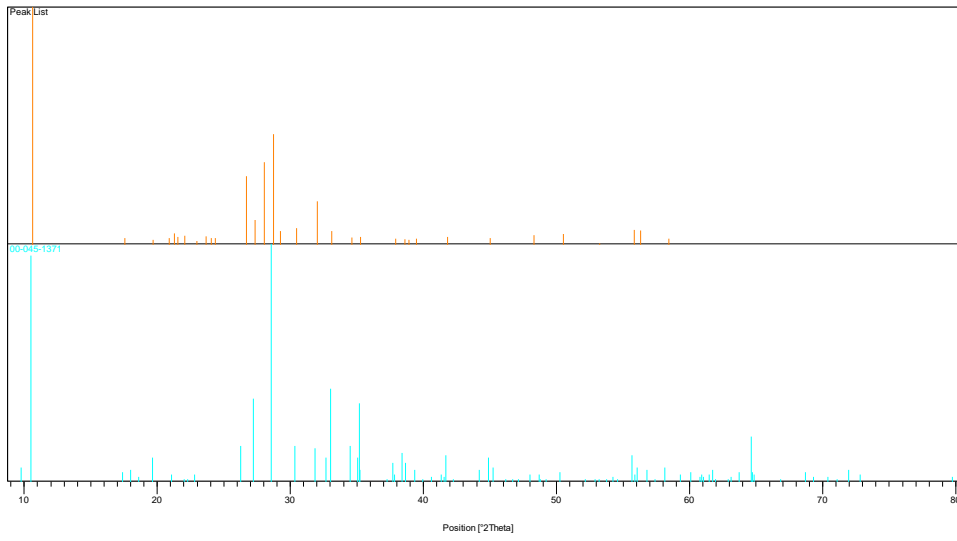
XRD – SAMPLE TMF 023 (RG2)
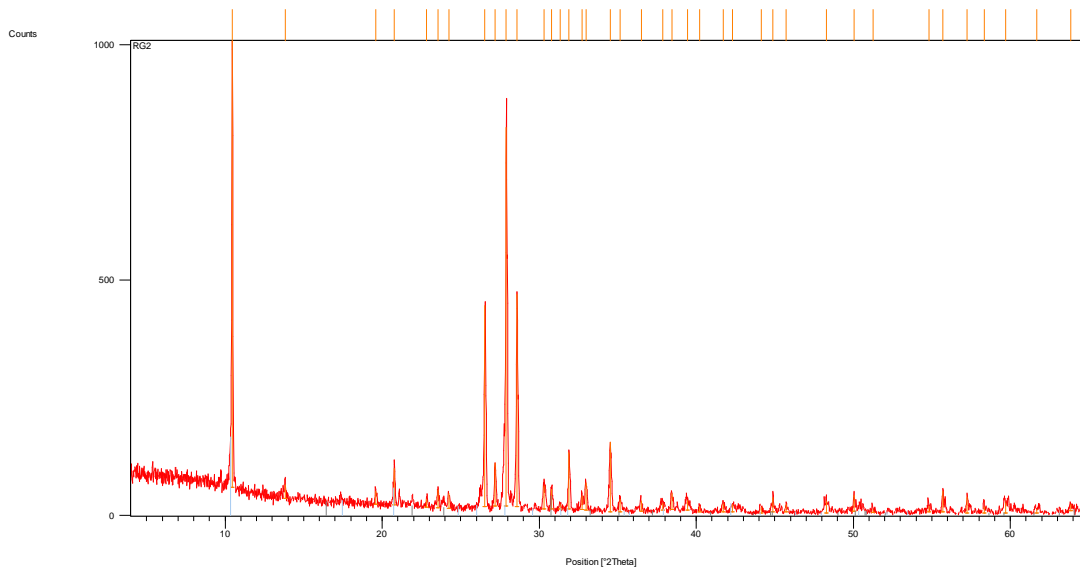
Pos. [°2Th.]	Height [cts]	FWHM [°2Th.]	d-spacing [A]	Rel. Int. [%]	Tip width [°2Th.]	Matched by
10,4675	962,98	0,0787	8,45150	100,00	0,0945	00-045-1371
13,8183	28,93	0,2362	6,40870	3,00	0,2834	00-041-1480
19,6036	28,92	0,1181	4,52852	3,00	0,1417	00-045-1371
20,7840	78,10	0,0787	4,27392	8,11	0,0945	01-089-8936
22,8365	17,27	0,2362	3,89422	1,79	0,2834	00-045-1371; 00-041-1480
23,5647	37,84	0,1181	3,77551	3,93	0,1417	00-041-1480
24,2410	31,33	0,1574	3,67168	3,25	0,1889	00-041-1480
26,5472	428,84	0,1181	3,35772	44,53	0,1417	01-089-8936; 00-041-1480
27,1903	91,96	0,1181	3,27975	9,55	0,1417	00-045-1371
27,8999	806,03	0,0984	3,19792	83,70	0,1181	00-041-1480
28,5802	452,41	0,0787	3,12334	46,98	0,0945	00-045-1371
30,3270	49,75	0,1968	2,94729	5,17	0,2362	00-045-1371; 00-041-1480
30,7771	42,94	0,0984	2,90521	4,46	0,1181	00-041-0586
31,3239	9,76	0,2362	2,85574	1,01	0,2834	00-041-1480

31,9002	120,49	0,0787	2,80545	12,51	0,0945	00-045-1371
32,7142	29,60	0,1181	2,73748	3,07	0,1417	00-045-1371
32,9896	58,20	0,1181	2,71525	6,04	0,1417	00-045-1371
34,5253	148,58	0,0984	2,59791	15,43	0,1181	00-045-1371
35,1641	27,90	0,1574	2,55217	2,90	0,1889	00-045-1371; 00-041-1480; 00-041-0586
36,4962	22,82	0,1181	2,46201	2,37	0,1417	01-089-8936
37,8532	15,13	0,3149	2,37682	1,57	0,3779	00-045-1371; 00-041-1480
38,4458	34,26	0,1574	2,34154	3,56	0,1889	00-045-1371; 00-041-1480
39,4511	21,03	0,3149	2,28415	2,18	0,3779	01-089-8936; 00-045-1371; 00-041-1480
40,2211	11,87	0,1181	2,24219	1,23	0,1417	01-089-8936
41,7244	16,79	0,2362	2,16481	1,74	0,2834	00-045-1371; 00-041-1480
42,3159	15,56	0,2755	2,13591	1,62	0,3306	01-089-8936; 00-045-1371; 00-041-1480

44,1396	11,45	0,2362	2,05181	1,19	0,2834	00-045-1371
44,8726	30,51	0,1574	2,01998	3,17	0,1889	00-045-1371; 00-041-1480; 00-041-0586
45,7064	15,87	0,1574	1,98505	1,65	0,1889	01-089-8936; 00-041-1480
48,2783	25,31	0,2362	1,88514	2,63	0,2834	00-041-1480
50,0384	35,63	0,1181	1,82288	3,70	0,1417	01-089-8936; 00-041-1480; 00-041-0586
51,2666	6,10	0,2362	1,78206	0,63	0,2834	00-041-1480
54,8275	12,81	0,2362	1,67445	1,33	0,2834	01-089-8936
55,6992	44,68	0,0720	1,64892	4,64	0,0864	00-045-1371
57,2538	34,14	0,1181	1,60912	3,55	0,1417	00-045-1371
58,3583	13,53	0,2362	1,58127	1,41	0,2834	00-041-1480
59,7198	22,26	0,3936	1,54844	2,31	0,4723	01-089-8936; 00-041-0586
61,6889	8,29	0,3936	1,50365	0,86	0,4723	00-045-1371; 00-041-1480; 00-041-0586

						01-089-8936; 00-045-1371; 00-041-1480; 00-041-0586
63,8642	14,25	0,2880	1,45638	1,48	0,3456	

Visible	Ref. Code	Score	Compound Name	Displacement [°2Th.]	Scale Factor	Chemical Formula
	01-089-8936	52	Silicon oxide - $-alpha	0,000	0,477	Si O2
	00-045-1371	41	Magnesiohornblende, ferroan	0,000	0,286	Ca2 (Mg , Fe +2)4 Al (Si7 Al) O22 (O H , F)2
	00-041-1480	16	Albite, calcian, ordered	0,000	0,377	(Na , Ca) Al (Si , Al)3 O8
*	00-041-0586	17	Ankerite	0,000	0,027	Ca (Fe +2 , Mg) (C O3)2